Weldability of AZ31B Magnesium Sheet by Laser Welding Processes

By

Elliot J. M. Powidajko

A thesis
presented to the University of Waterloo
in fulfillment of the
thesis requirement for the degree of
Master of Applied Science
in
Mechanical Engineering

Waterloo, Ontario, Canada, 2009

AUTHOR'S DECLARATION

I hereby declare that I am the sole author of this thesis. This is a true copy of the thesis, including any required final revisions, as accepted by my examiners.

I understand that my thesis may be made electronically available to the institutions or individuals for the purpose of scholarly research.

Elliot Powidajko

Abstract

Due to finite fossil fuel resources and the impact on our environment of burning fossil fuels, the automotive industry has been investigating ways to reduce the overall weight of automotive vehicles. This has led to increased interest in ways that light weight alloys such as magnesium can be used in fabrication of automotive parts and manufacturing processes such as welding that would enable increased use of magnesium. The objectives of this project were to characterize and determine the weldability of 2 mm thick AZ31B-H24 magnesium alloy by three different laser beam welding processes: a 4 kW Nuvonyx ISL-4000L high power diode laser, a 5 kW Trump TLC-1005 CO_2 laser, and a 10 kW YLR-10000-WC fibre laser.

The diode laser operated with a 0.9 by 12 mm spot size and with a maximum power density of 37 MW/m^2. Due to its low power density, the diode laser was restricted to conduction-mode welding which produced wide fusion zones. The AZ31B magnesium laser welds exhibited a number of defects including hydrogen porosity, solidification cracking, liquation cracking, high vaporization rates, molten expulsions, and poor weld bead quality due to low surface tension. It was found that the majority of these defects could be controlled through the proper use of clamping and shielding of the weld pool and joint preparation and surface cleaning prior to welding.

The as-received base material was delivered with a dark grey hydrated oxide layer. This surface condition was found to increase the overall diode laser beam absorption but was

detrimental to the welding process when disrupted. When incorporated into the weld pool, the oxide created weak facets where solidification cracks would initiate or acted to localize strain during tensile testing. Proper joint preparation was required to produce a high quality diode laser weld: machining of the joint interface to remove interfacial gaps, chemical cleaning with acetone and ethanol to remove residual oils or grease, and stainless steel wire brushing to remove the oxide. Diode laser welds made using 3 kW power and 0.75 m/min welding speed achieved approximately 60% of the base metal's ultimate strength and less than 15% of the base metal ductility. The reduced strength and ductility were attributed primarily to the weld defects which acted as strain localizers during plastic deformation and the lack of strain hardening in the weld metal.

Both the CO_2 and fibre lasers beams had focal spot sizes of 300 μm diameters and maximum power densities of 70 and 140 GW/m^2, respectively. At these power densities, the CO_2 and fibre lasers operated in keyhole-mode and produced welds which had narrower columnated fusion zones. The CO_2 laser keyhole-mode welds exhibited keyhole instability and bulk material loss through vaporization that resulted in macro-porosity, under-fill, and generally poor weld bead quality. Welds produced using 5 kW power and 8 m/min welding speeds achieved approximately 70% of the base metal's ultimate strength.

The highest quality fibre laser welds were produced at 2 kW power and 100 mm/s welding speeds. These defect-free welds achieved transverse tensile strengths that were 86% of the base metal's ultimate strength. The 14% loss of strength was attributed to the difference in temper of the base metal and the weld metal. The base material was received in

a half-hard H24 temper and the as solidified weld metal is naturally in the softer F temper. This also resulted in a corresponding 15% reduction in hardness. Failure always occurred in the softened fusion zones of the welded samples where the measured hardness was reduced to an average 60 VHN_{25} from the base metal's 75 HVN_{25}. The fibre laser weld samples also experienced the greatest extension of any of the tested welds with a cross head displacement of 30% of the base metal. The extreme reduction in overall cross head displacement was attributed to the lower strength of the fusion zone. This led to strain localization in the transverse tensile specimens and premature failure that occurred prior to plastic deformation of the surrounding base material.

Proper joint preparation was found to be critical when laser welding AZ31B magnesium sheet. Machined interfaces were required to minimize the gap and degreasing and stainless steel wire brushing were required for removal of the pre-existing hydrated oxide in order to produce sound laser welds. Helium shielding gas was found to improve the weld bead surface quality compared to argon. The keyhole-mode welds produced with the CO_2 and fibre lasers were superior compared to the conduction-mode welds produced with the diode laser. This was due to the narrower fusion zone and reduced bulk material loss. Of the three laser welding processes examined in this study, the fibre laser produced the highest quality, strongest, and most ductile welds when analyzed in transverse tensile testing. However, direct comparisons between the CO_2 and fibre laser welds could not be made because they were made using different joint preparations and welding conditions.

Acknowledgements

I would like to acknowledge the incredible amount of help given by Professor David C. Weckman in the organization and guidance of both the research and writing of this thesis. To all three of my academic supervisors: Professors Norman (Y.) Zhou, David C. Weckman, and Michael Kuntz, and to the entire Center for Advanced Material Joining (CAMJ) at the University of Waterloo, your help and knowledge has been invaluable.

I would also like to acknowledge the support from industrial partners. Prometek provided equipment in the form of their CO_2 laser and on site analytical equipment. Mike Babiak, Wayne Chabrol, and Raj Majesty provided sound technical advice and support during the work conducted at Prometek. IPG Photonics also provided manpower and equipment to further this research with their fibre laser and skilled personnel: Mike Klos, Eric Stiles, and Garrett Larrimore.

This research was funded by Auto21 and supported by the Magnesium Front End Research and Development (MFERD) tri-country venture. The material was supplied by General Motors through the MFERD project.

Dedication

To those who have fought the good fight and helped me to greater achievements both academically and as a person.

To Professor David Weckman, without your support, none of this would have been possible.

To my coworkers and peers, Trevor Burns, Jesse Brenneman, and Lee Upshall, who helped me on a day to day basis, and the support staff at the University, specifically Laurie Wilfong, who kept this juggernaut rolling.

Lastly, to my family and other friends who supported me and put up with me over these years, my parents Linda and Jerry, step-mother Kim, siblings Kasey and Nicholas and my friends Annette Brown, Jeannie Tam, and John Olaveson. Your dedication to me is more than I could have hoped for and more than I deserve.

It is to you that I dedicate this thesis.

Table of Contents

List of Figures

List of Tables

List of Equations

Chapter 1

Introduction

1.1 Identifying the Need

Natural resources are harvested to produce energy to power homes and factories, to transport people and products around the globe, and to feed the demands of the world as it is. Coal, oil, gas, and other forms of fossil fuels form the backbone of the majority of the world's energy consumptions. These resources are made readily available for many purposes, but the scarcity of such substances places demands on science and technology to make the most of them.

In the automotive industry, gasoline is still the dominant fuel source for powering vehicles. To help foster the global push to conserve our planets dwindling supply of high energy density fuels, research into new designs and materials has been made a priority to decrease the rate vehicles consume them. Several different possibilities have been identified to achieve this goal and are being investigated. On the manufacturing level, redesigning and

consolidating several complex parts can reduce the overall part number and complexity of automotive designs. This is beneficial because the final product would require fewer stages in manufacturing and inventories for repair. By reducing the overall complexity, the cost of manufacturing is reduced, but this will have marginal long term benefits if there is no reduction in weight associated with the redesign. The other area of interest is in the selection of lighter alternative materials to build vehicles. By manufacturing equivalent parts that are lighter, less fuel would be consumed and there would be lower emissions of harmful gases into our environment for every kilometer the vehicle travels. Thus, there is currently much interest in exploring ways that automotive vehicles can be made using lighter weight materials rather than traditional heavier materials such as steel. Magnesium is one of the lightest weight structural materials known to man and is therefore one of the key materials being investigated to replace steel in automotive applications.

1.2 Magnesium Alloy Nomenclature

The nomenclature used to identify wrought and cast magnesium alloys is straightforward. All magnesium alloys are denoted by four primary characters, two letters followed by two numbers [1]. The two primary alloying elements are each represented by a single letter in order of their concentration in the alloy. Table 1-1 shows the list of commonly used alloying elements [1] and their abbreviated letter. For example, the alloy AZ31 is a common, general purpose wrought alloy used widely in sheet and plate form [1, 2]. The 'A' identifies aluminum and 'Z' zinc as the two primary elements in this magnesium alloy. The two digits that follow the elements are the nominal weight percentages of each element. For example, AZ31 has a nominal composition of 3 wt%

Table 1-1: List of alloying elements (taken from ASTM [1]).

A	--	Aluminum	Q	--	Silver
C	--	Copper	S	--	Silicon
E	--	Rare Earth	T	--	Tin*
H	--	Thorium*	V	--	Gadolinium
J	--	Stronium	W	--	Yttrium
K	--	Zirconium	Z	--	Zinc
L	--	Lithium*	* For historical Referance		
M	--	Manganese			

aluminum and 1 wt% zinc. Inferred with this nomenclature is the assumed error of ±0.5 wt% which provides a range of possible compositions for a given alloy name.

The major hindrance in identification of generic magnesium alloys is that any other element could theoretically be added such that it does not exceed the quantity of the second noted alloying element. This variance in the exact composition causes confusion among similarly-named compositions and can necessitate further clarification for more exact identification. When several alloys with the same initial four characters become commercially common and require differentiation, an additional letter is added to the initial four characters. This letter is assigned in alphabetical order chronologically based on when each alloy variation was identified as a commercially standard magnesium alloy. The specification of an alloy subset also sets further requirements on the alloy that need to be referenced specifically for each individual alloy. AZ31B is a commonly used alloy in the AZ31 family. When referenced further, the B in AZ31B can be found to specify the alloy must also meet additional requirements for concentrations of other minor alloying elements like molybdenum. The full list of AZ31B's alloying elements and their nominal values can be found in Table 1-2.

Table 1-2: Standard composition of AZ31B in wt% (taken from ASM [2]).

Alloy	Al	Ca	Cu	Fe	Mn	Ni	Si	Zn	Other
AZ31B	2.5-3.5	0.04	0.05	0.005	0.20-1.0	0.005	0.10	0.6-1.4	0.3

The final piece of information that can be found in an alloy description follows the material identification and pertains to the manufacturing processes used to produce the final product. For example AZ31B-H24 is a further distinction to the previous alloy. H24 is a temper designation that indicates the magnesium was hot rolled and then annealed 50%, *i.e.* on a scale from 0 for fully annealed and 8 for fully work hardened, H24, is annealed to a half hard condition. The full list of heat treatments and processing standards can be found in Table 1-3 and include the common final product states such as fully stress relieved, denoted by 'O'. With the use of these ASTM nomenclature standards, non-standard alloys can be easily approximated and common industrial alloys can have their composition and important processing readily conveyed.

Table 1-3: Heat Treatments and Processing Information (taken from ASTM [1]).

Temper				
F	As-Fabricated			
O	Annealed, Recrystalized (Wrought Only)			
H	Strain Hardened			
	H1X	Strain Hardened Only		
	H2X	Strain Hardened and Partially Annealed		
	H3X	Strain Hardened and then Stabalized		
	X	A Number, 0 - 8 | 0 is Fully Annealed and 8 is Fully Hardened		
W	Solution Heat Treated			
T	Thermal Treatment Producig a Stable Temper Other Than F, O, or H			
	T1	Cooled and Naturally Aged	**T7**	SHT and AA
	T3	SHT and Cold Worked (CW)	**T8**	SHT and Stabalized
	T4	Solution Heat Treated (SHT)	**T9**	SHT, CW, and AA
	T5	Cooled and Artificially Aged (AA)	**T10**	Cooled, AA, and CW
	T6	SHT and AA		

1.3 Benefits of Magnesium

Magnesium can be found abundantly in many forms including dolomite, magnesite, and carnallite. The most abundant sources of magnesium are chlorides in sea water, as brines and other salt deposits. Produced as a byproduct of the desalination process, it has been estimated that in a cubic mile of sea water, there exists some 6 million tons of magnesium. With approximately 320 million cubic miles of sea water on Earth there is an almost unlimited supply [2-4]. Magnesium has a density of 1.74 g/cm^3 which is approximately 65% the density of aluminum, and only 22% when compared to steel, thus making magnesium one of the lightest structural metals [2-6]. The metal's low density allows for a large weight reduction in components when constructed with magnesium over other commonly used structural materials such as steels or cast irons. The thermal conductivity of magnesium is comparable to aluminum, and both far exceed the thermal dissipation capabilities of steel. The high thermal conductivity of magnesium prevents heat buildup and makes magnesium ideal for heat transfer systems. The high thermal conductivity also prevents magnesium from localized combustion despite its increased reactivity at high temperatures. Magnesium castings also exhibit excellent sound dampening characteristics [7], a property which has been used to advantage in automotive designs.

1.4 Disadvantages of Magnesium

While the low specific weight of magnesium makes it desirable to use, the lower specific strength and generally poor ductility of magnesium alloys necessitate that larger components be used when designing with magnesium. This can be prohibitive in existing designs as it generally requires modifications and redesigns of adjoining parts and increases the net cost of

the part. Magnesium also has a much lower melting point than steel and is not generally suitable for high temperature applications where creep or fatigue may play a factor. Molten magnesium is also highly reactive in air and during welding will react with the oxygen, nitrogen, and carbon if not properly shielded. Common welding defects encountered in the welding of magnesium alloys include; porosity, solidification and liquation cracking, loss of alloying elements, and the inclusion of oxides [8]. The most prohibitive aspect associated with working with magnesium is still an economical one since magnesium can cost up to 6 times that of steel and twice that of aluminum on a mass basis [7].

1.5 Welding and Joining of Automotive Structures

In the creation of an automotive body, the numerous components are individually created and organized into several levels of sub-assemblies. Since the final product cannot be made of a single piece, a method of connecting interacting parts is required. Mechanical connectors such as bolts and nuts can affix two or more parts together. These connections provide the option for subsequent disassembly and replacement of the individual components. This can be suitable when certain parts are attached to parts with shorter life-spans or that are intentional failure points. Mechanical connectors provide generally poor stress and strain transfer between components. Fusion welding is the primary joining method used in structural components where high efficiency stress and strain transfer is required, such as in a roll cage. Fusion welded joints are permanent connections between components where the interface between the components was melted and solidified as a continuous junction. Arc and resistance spot and seam welding are three commonly used electric welding processes used in the automotive industry. All of these processes require access to

both the front and reverse sides of the materials being joined but have a high threshold for low tolerance joints. Laser welding is advantageous compared to the previous methods in that it only requires access to one side of the weld and can be conducted at much faster welding speeds. Keyhole-mode laser beam welding can produce much smaller welds compared to the previous fusion welding processes. However, because the laser beam spot size is very small, typically less than 1 mm in diameter, the joint interfaces must be prepared very carefully to minimize any gap between the parts at the joint. The possibility of implementing magnesium alloys into the structural components of auto-body construction necessitates that enabling technologies for welding and joining of magnesium alloys be identified and assessed. Due to the numerous advantages of laser beam welding processes in many automotive manufacturing applications, there is a need to explore the weldability of magnesium alloys by laser beam welding processes. Development and assessment of this enabling joining technology will facilitate a more rapid incorporation of light weight magnesium alloys into automotive structures.

1.6 Laser Fundamentals

The term laser is an acronym for light amplification by simulated emissions of radiation [9]. All lasers consist of several fundamental components: a lasing medium, a method of excitation of the lasing medium, and a beam delivery system to collimate, direct, and focus the coherent monochromatic laser beam onto the surface of the part to be welded.

A laser beam is generated by the excitation of electrons to higher valance energy levels [10] as depicted in Figure 1-1. This is done when the lasing material is excited by the external energy source. These excited electrons jump from their conduction band to a

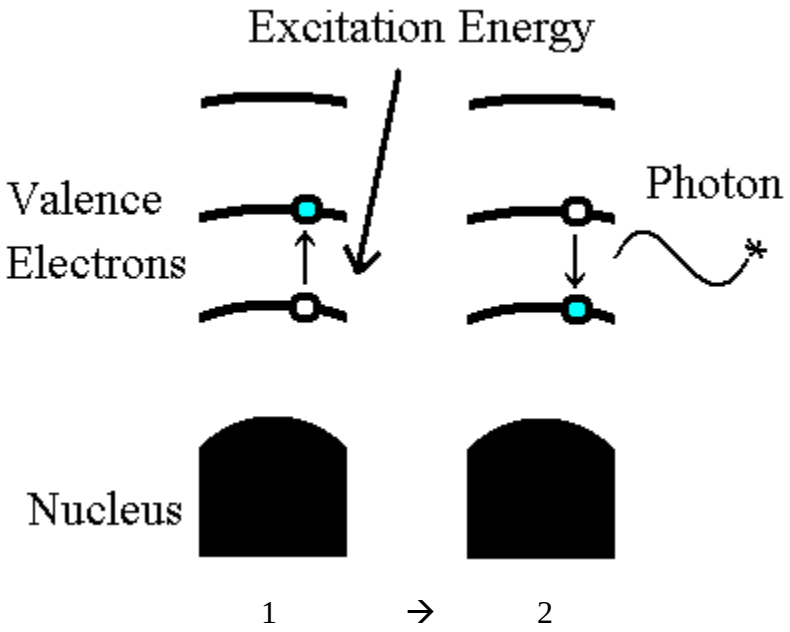

Figure 1-1: Production of a laser photon by external excitation of an electron-hole pair.

valence band, creating an unstable electron-hole pair. In the process of collapsing back to a lower, more stable energy state, the electron emits light photons in the process. These emitted photons will be of a single wavelength because the level of electron excitation and collapse are functions of the energy source and lasing material. The emitted photons are then collected within the lasing medium where they are reflected between two reflective mirrors, one that is as close to fully reflective as possible, and another that is slightly less to permit a controlled outlet for the generated beam. This continued reflection creates a resonance of the created beam in the lasing medium. The level of rebounding can vary depending on what kind of laser is used but in each reflection between the mirrors, additional photons are created that are not only in line with the original photon, but are also in phase. This process needs to be heavily controlled since it can quickly create a huge amount of light photons that are highly-collimated and in phase once there is a population-inversion. Population-inversion refers to the transfer of the lasing medium from an equilibrium state where more atoms are in

the stable lower energy state than the unstable excited energy state. Once there exists more excited atoms than stable atoms in the lasing material, it is said to have undergone a population-inversion [9]. Laser beams will generally pass through a polarization filter to ensure the created laser beam is identically oriented and phased to prevent interference. The final step in most lasers is the focusing of the beam into the desired final convergence point where the laser is actually used.

1.6.1 Diode Lasers

Diode lasers are solid state lasers produced using p-n junctions. As seen in Figure 1-2, the built up p-doped cladding acts as an optical wave guide that contains the produced photons. This effect is due to the current flow following the channel built by the insulator guiding the current preferentially to a small portion of the active layer. This active region prevents the distribution of electrons or holes because the energy required for the promotion of the valence electrons to reach the holes is reduced [11]. In the typical diode laser emitters, shown in Figure 1-3, aluminum oxide is used as the mirror surfaces with silicon added to the higher reflective surface to decrease its transmission. For beams created with 800 to 1200 nm wavelength, the aluminum oxide and silicon mirrors have been shown to have reflectivity of 90% or more [11].

Advantages of the diode laser include the small footprint required for the system. This can be advantageous in mass production assembly lines where many units would be required to operate in close proximity to increase throughput where the diode laser would have the advantage of having very compact and lightweight emitters. The diodes themselves are very

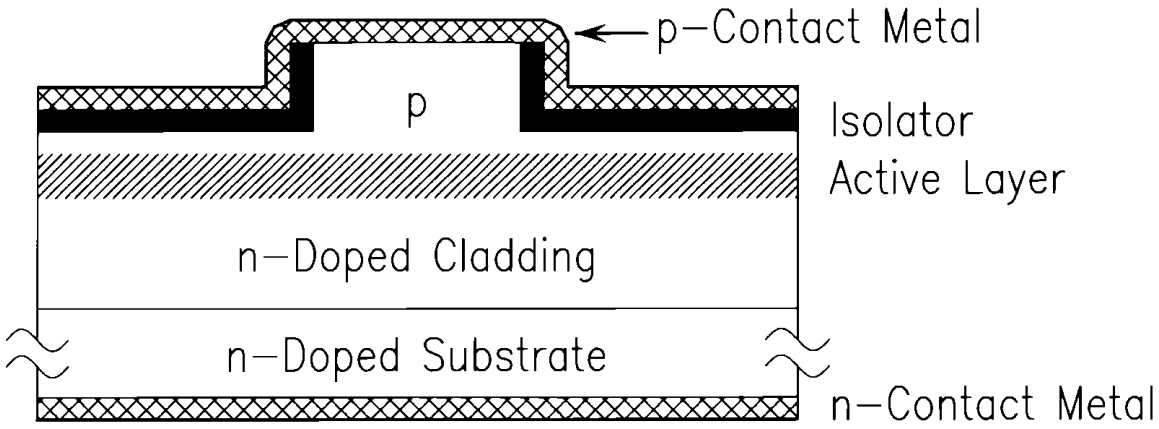

Figure 1-2: Diode configuration with current and optical beam confinement (taken from Diehl [11]).

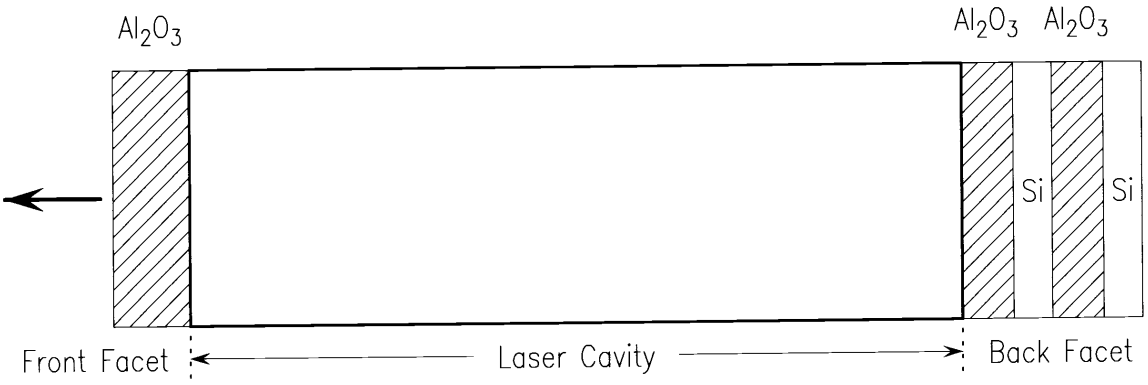

Figure 1-3: Mirror coating for high-power edge emitting lasers (taken from Diehl [11]).

small and are easily mounted directly to a robotic arm. Diode lasers also suffer from limitations; the produced laser from a single diode is not fully symmetric and generally produces an elliptical shaped spot as shown in Figure 1-4 with a top-hat distribution along the y-axis and a Gaussian distribution along the x-axis. Each individual diode can only produce a very small amount of laser energy due to the micro-scale of the p-n junction. The diodes, therefore, must be stacked together in large arrays to produce a sufficient amount of laser power to be viable. Grouping many individual diodes causes the resulting laser beam to be spread out over a larger area, limiting the power density of the beam and preventing the

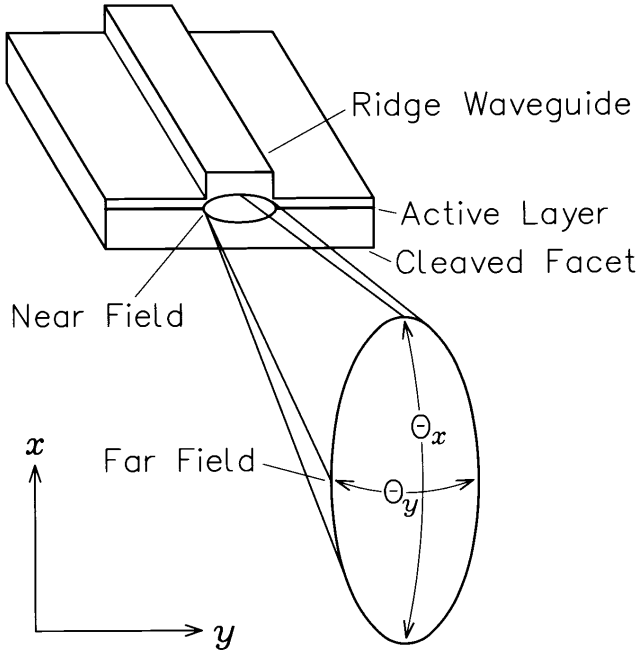

Figure 1-4: Diode Laser emission profile (taken from Diehl [11]).

diode laser from welding in anything but conduction mode. The diodes also produce a large amount of heat which can damage the diodes. Thus, additional chilling of the diode must be supplied during operation. Lastly, the thermal cycling of the diodes leads to a degradation of the emitters over time that slowly lowers the maximum achievable power [12].

1.6.2 CO_2 Lasers

CO_2 laser systems are unlike the previous diode system which was a solid state laser. The lasing material producing the CO_2 laser beam is a gas mixture of CO_2, He, and N_2 combined in a 0.8 to 1.0 to 1.1 ratio. This mixture is then excited through electrically ionization by a high voltage power supply [13]. The CO_2 produces the desired photons with a characteristic wavelength of 10.60 μm, while nitrogen promotes the excitation of the CO_2, and helium is used to more rapidly quench the CO_2 so that it reverts back to the non-energized state emitting the desired photons [14]. The two mirrors reflect the photons

repeatedly through the gas to propagate a single phase collimated beam. Figure 1-5 shows a schematic of a sealed tube CO_2 laser with Brewster angles cut at either end which work to polarize the laser as it is reflected between the two mirrors. Similar to the diode, the output mirror's reflectivity is reduced to permit a small amount of the laser beam to escape the cycle of reflections.

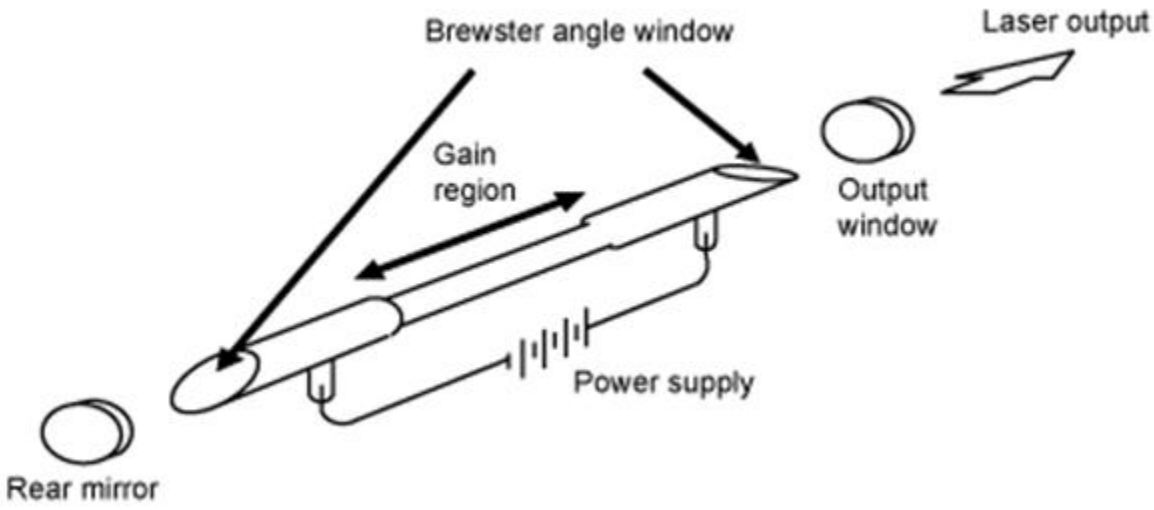

Figure 1-5: Schematic of a general CO_2 laser set up (taken from Silfvast [13]).

CO_2 lasers have lower wall-plug efficiency than diode lasers [13]. The power density of a CO_2 laser beam is also much greater when compared to a diode laser beam of comparable power because the CO_2 laser beam can be focused to a very small circular profile with nominal spot sizes of the order of 200-400 μm diameter. This small spot size and high power density at the beam focus permits the CO_2 laser to operate in keyhole mode or to be defocused and operate in conduction mode. The gas tube in the CO_2 laser is, however, delicate and generally not located in the laser head like the diodes were in the diode laser. With a smaller divergence angle than the diode laser, the CO_2 laser is transmitted via high precision mirrors to the work piece. These distances are commonly encased in tubes to

prevent undesired interactions with the beam. This prevents the gas tube from being damaged as it is kept stationary, remote from the laser head and the beam is transmitted to the work piece.

1.6.3 Fibre Lasers

Fibre lasers essentially consist of a doped fibre where the laser is produced, an excitation source, and a beam delivery system. The fibre laser is unique in that the lasing media is contained within an optical fibre. Broad area multimode pump diodes surrounding the fibre are then used to invoke the doped fibre to produce photons [15]. A general schematic of these components is shown in Figure 1-6. The diode laser is used to excite the doped fibre and produce the emission of photons which, due to the fibre's refractive nature, are contained within the strand and propagate back and forth along its length. To prevent the uncontrolled escape of photons in the fibre ends, Bragg gratings are created in the fibre. These gratings are created by intense ultra-violet light that writes a periodic change in the refractive properties of the affected area [11]. The Bragg gratings act as high-efficiency mirrors in the fibre and can be modified for a specific desired wavelength which allows fibre laser beams to be created with a range of wavelengths. The reflection within the fibre between the two sets of Bragg gates set up a resonance similar to the two previous laser systems that produce a single phase collimated beam with a wavelength between 1060 and 1070 nm. The output laser generally goes through additional beam collimators to eliminate any residual aberrant elements and to focus the beam to the final desired spot size.

Fibre lasers have only recently become viable as high-power laser sources [16]. Initial equipment expenses are more than offset over the laser's life cycle due to the fact that it

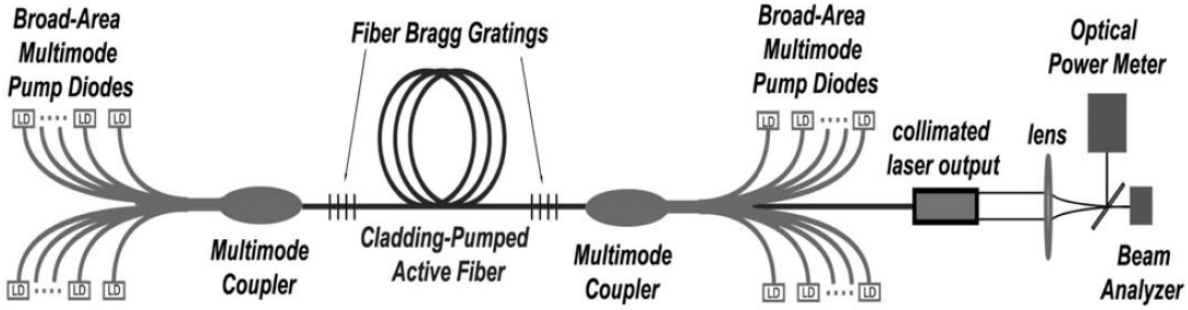

Figure 1-6: Schematic of a general fibre laser set up (taken from Gahan [15]).

requires almost no maintenance, it does not require additional cooling, and has one of the highest wall-plug efficiencies of any laser beam process (between 25 and 30%). Also, the resulting beam experiences less divergence than other comparable laser beams [15]. The major difficulty with fibre laser technology is that it is patented proprietary knowledge [15] and it uses fibre optics in creation of the laser beam and to convey it to the laser head [11].

1.7 Conduction versus Keyhole Mode Welding

Laser welding processes fall primarily into one of two distinct modes of heat transfer, conduction or keyhole-mode welding. Conduction-mode welding is so named because the heat is conveyed through the specimen via thermal conduction. The focused laser beam is incident on the material surface and all the energy required for heating, melting, and welding must be absorbed from this surface source of heat. The energy is then conveyed into the material primarily by thermal conduction.

A schematic depiction of a conduction-mode weld can be seen in Figure 1-7a. Conduction-mode welds are characteristically twice as wide as they are deep. Lasers with lower power densities are generally limited to operate in conduction-mode. Making the transition from conduction to keyhole-mode welding requires a drastic increase in power density. At these transition power densities, the weld profile takes on characteristics of both

conduction and keyhole welding modes. The upper surface of the weld has a characteristic hemispherical profile with a high penetration keyhole forming a nail shape in section [9]. In full keyhole-mode laser welding, the laser power density is high enough to form a vaporized pocket or keyhole of plasma in the weld pool. As depicted in Figure 1-7b, the vaporization pressure produces a recoil force that creates a depression in the weld pool [17]. For the newly-formed cavity to remain stable, the vapour pocket must be able to withstand the counteracting forces of gravity, surface tension, and impinging shielding gases. Keyhole-mode welding produces weld profiles that are far more penetrating than they are wide and generally lead to an increase in efficiency because the keyhole effectively acts as a beam trap [18].

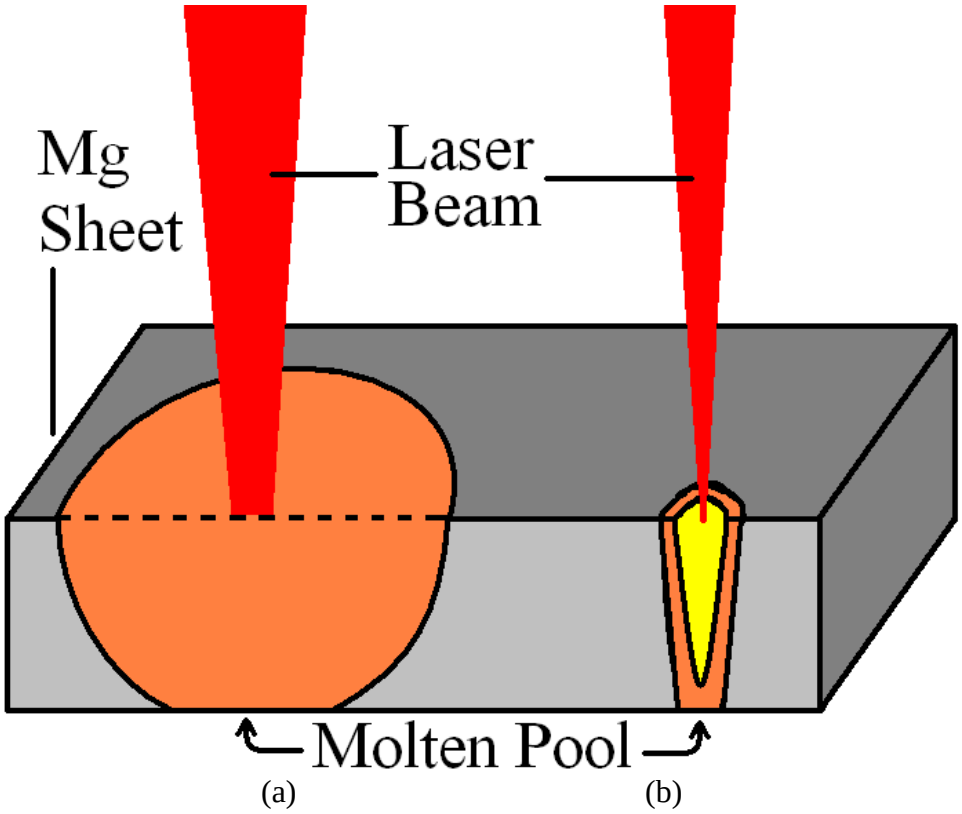

Figure 1-7: Comparison of: a) conduction and b) keyhole-mode weld pool profiles.

1.8 Goals and Purpose

To determine if magnesium can be a viable structural material for use in automotive bodies, three different lasers have been identified: the conduction-mode diode laser, and the keyhole-mode CO_2 and fibre lasers. Using these identified processes, the purposes of the research conducted in this study were:

a) to determine the feasibility of welding AZ31B magnesium alloy sheet through the applications of the various laser welding technologies,

b) to evaluate the effects of laser beam power and travel speed and provide operational windows when using three different types of lasers,

c) to quantify the quality of the laser welds through mechanical testing and analysis, and if determined feasible,

d) to examine which laser beam welding processes and their respective parameters are viable for laser welding magnesium alloys.

Chapter 2

Literature Review

While research in structural metals properties and applications is an active and growing field, the majority of the research conducted is centered primarily on steels and aluminum alloys. Magnesium and its alloys are still not experiencing the same level of interest and investigation in the automotive industry due to numerous factors including but not limited to: availability, cost, and industrial reluctance to adopt new materials.

Magnesium is a high strength-to-weight ratio material with applications in the automotive, building construction, and aerospace industries. As of yet, it is not widely used outside of cast components because it is still a new material and sufficient knowledge has not yet been acquired for general acceptance and integration into modern engineering structures and machines.

The welding and joining of magnesium is required in almost any large scale application of the material. Mechanical connectors use a larger volume of material, are less effective in the distribution of applied stresses, and require a great number of components for assembly when compared to welding processes. The weldability of magnesium alloys by various welding processes including; arc, resistance, friction stir, electron beam, and various laser and laser-hybrid welding processes has been investigated for specific applications.

Arc-welding is one of the most readily-available welding processes, experiencing efficiencies up to 80% [19]. The weldability of magnesium by arc welding, specifically gas tungsten arc welding, is generally considered to be excellent [20]. However, arc welding processes inherently have slow production rates relative to other welding processes. Zhou *et al*. [21] have investigated partial penetration welding of AZ91D with tungsten inert gas arc welding. Working with 3-5 mm cast plate and weld travel speeds of 5 mm/s, they found evidence of the brittle Al-Mg eutectic and $Al_{12}Mg_{17}$ intermetallic in their ingot castings. These brittle constituents were not found in the weld fusion zones due to the higher solidification rate of the weld metal. The slow cooling rates for the AZ91 cast plates produced large dendritic grains with evidence of macro-segregation. These segregated regions had some eutectic and suffered from hot-cracking during welding when contracting thermal stresses exceeded the heat affected zone's strength along the root surface and opened liquation cracks originating from the root surface. The weld metal tensile properties were 50% greater than the base plate's ultimate tensile strength of 160 MPa. This increase in mechanical properties is largely attributed to the low quality of the base material and finer solidification structure found in the weld fusion zone microstructure.

Zhang *et al.* [22] also investigated TIG arc welding of 5 mm thick AZ31B magnesium plate at 5 mm/s travel speed. They applied an activated flux to investigate its effect on the weld profile. The addition of TiO_2 and Cr_2O_3 were both shown to increase the welding penetration. The welds made using Cr_2O_3 exhibited a 50% increase in penetration compared to the welds made without flux. Use of SiO_2 was also investigated due to previous results with aluminum and steel but in the case of magnesium, the flux was found to dissociate and form magnesium oxides. The trend discovered with the activated flux TIG arc welding was that as the weld penetration increased, the surface bead profile degraded. Additional tests were conducted to analyze the effects of the three fluxes when using different of travel speeds, electrode stand-off distances, and current settings. In all cases, the previous penetration trend was continued with expected reactions to the varied parameters. No mechanical testing was conducted on any of the weld samples; only analysis of the bead profile was conducted. It was determined that SiO_2 should be avoided when welding magnesium as the silicon will readily shed its oxygen, oxidizing the weld metal and contaminate the weld pool with silicon, and that higher penetration is achievable in TIG arc welding with the application of activated fluxes.

Another process that has been widely used in the automotive industry is resistance spot welding (RSW). Sun *et al.* [23] investigated RSW of AZ31B magnesium sheet. It was found that with higher current levels, the high internal thermal stresses of the weld created solidification cracking in the fusion zone and the welds experienced both expulsion and severe electrode indentation. This was remedied by a reduction in power level, but this also limited the size of the resulting weld nugget and overall joint strength. Achieving button

pullout at currents of 19–23 kA, and interfacial failure below that, they correlated the nugget size to the final shear strength and concluded that 23 kA weld current provided the highest strength welds while preventing the previous welding defects associated with higher-current welding parameters.

Gould and Chuko [24] used AZ91 and compared RSW against a more recently developed process, friction stir welding (FSW), developed by The Weld Institute of Cambridge [25]. FSW has been a major source of interest for magnesium and aluminum welding, because it is a solid-state welding process. Having the material remain solid during the welding process prevents defects associated with solidification such as hydrogen porosity or solidification cracking and reduces thermal contraction and residual stresses. Similar to the study by Sun *et al.* [23], Gould's RSW welds suffered from solidification cracking and liquation cracking through the heat affected zone that initiated from the sheet-seam interface. The higher aluminum content increased the formation of intermetallics and susceptibility of the material to hot-cracking. This required lower optimized weld currents of 20 kA with down-sloped weld profiles to prevent expulsion. The hardness of the weld profile showed that the entire weld experienced between 15-20 VHN softening with the fusion zone boundary experiencing an additional 5 VHN decrease. The FSW welds were found to exhibit far less softening, approximately 10 HVN localized to the stir zone and thermo-mechanically affected zone (TMAZ), with joint efficiencies approaching the base metal. This high quality of the weld was attributed to the lack of melting and grain refinement inherent to the process, which both prevents segregation and results in an equiaxed grain microstructure.

Additional studies have been conducted by Afrin *et al.* [26] and Xunhong and Kuaishe [27] to investigate FSW of AZ31B. Afrin conducted a more in-depth examination of the FSW microstructure and derived a Hall-Petch correlation between grain size and micro-hardness. They also found that the softening in the TMAZ was preferentially skewed to the advancing side of the FSW weld tool. This was attributed to the higher velocity of the pin along the advancing side, which produced greater grain refinement than the retreating side, and had a gradual and even hardness profile from the weld center-line to the base metal. Xunhong and Kuaishe [27] investigated the effects of rotational speed on mechanical properties and exhibited results indicated that higher pin rotational speeds produced higher-strength welds, especially at very low tool travel speeds. Optimized at a rotational speed of 1500 rpm and travel speed of 90 mm/min, the FSW samples achieved 93% of the base metal properties, with a failure strength of 255 MPa.

Another modern welding process used by Chi *et al.* [28, 29] to weld AZ series magnesium plate is electron beam (EB) welding. EB welding uses the kinetic energy from accelerated electrons to produce heating for welding. The process is very efficient with an estimated 95% of the kinetic energy transferred from the electrons to the sample during welding. The system does require a high vacuum to operate, as air or other gasses would quickly scatter the beam prior to impacting the material's surface, but can achieve full penetration in 11 mm thick plate when traveling at speeds of 60 mm/s. Using Taguchi's method for analysis of parameter interactions and simultaneous optimization, the critical parameters were identified in the following order: the focal position and travel speed were the critical parameters, with the accelerating voltage, beam current and post-weld stress relief

having lesser effects. In many of the EB welds conducted, the top bead surface exhibited roping along the weld toe. Under-fill was common along the root surface, but this was controlled with careful selection of welding parameters. Even when optimized, porosity was still prevalent in both the AZ61 and AZ91 samples. At their optimized parameters, the AZ31 weld samples withstood up to 270 MPa of stress before failure. The AZ61 and AZ91 weld samples proved to be similar; both achieving approximately 290 MPa failure strength.

Focusing on the fracture modes of the above optimized weld parameters, Chi *et al.* [30] discovered that while the increase in aluminum content (up to 10%) increased the ultimate tensile strength of the welded samples, it also decreased the ductility. The AZ31 samples all exhibited failure in the fusion zone, all of the AZ91 samples failed in the heat affected zone, and the AZ61 samples failed in a mixture of both modes during tensile testing. The previously identified defects of roping along the crown and root side undercutting were again identified as sources of strain localization and causes for lower than base metal tensile performances. Overall, the AZ91 was identified as the most robust alloy with the largest weld parameter operation window, and the AZ31 was identified as the most sensitive alloy to changes of welding parameters.

Adapting the arc welding process to improve its slow travel speeds and lack of penetration, new processes have been developed that incorporate a laser beam welding system working simultaneously with an arc welding process to perform hybrid welds. Liu *et al.* [31] have investigated using this hybrid process to perform bead-on-plate welds on 5 mm plate AZ31B. A 400 W pulsed Nd:YAG laser was oriented perpendicular to the plate and the TIG torch was placed behind the laser, pushing the weld pool. The process was

shown to produce a very high-quality weld bead profile, but transverse cross-sections showed the presence of macro-porosity. This was attributed to the incomplete shielding provided by the TIG torch which allowed a portion of the weld pool to react with the atmosphere. By providing additional shielding to the welding process, the macro-porosity was eliminated. Liu *et al.* [32] continued their study of hybrid welding on 2.5 mm AZ31B in a lap-joint configuration with the TIG torch reversed to the pulling side of the weld bead. The hybrid process was well-tailored to conduct lap joints since the TIG welding arc melts the upper sheet and allows the laser to penetrate through to the second sheet. At travel speeds below 1000 mm/min, the conducted weld samples experienced blow holes from excess energy. The weld was optimized at travel speeds between 1400 and 1700 mm/min. Further testing was performed to examine the effects of the laser focal position and separation between the laser and arc welding locations. It was found that when the laser was focused on the upper surface and the TIG torch preceded the laser by 1.0 mm, the penetration was maximized at 3.2 mm and the welds achieved 80% of the base metal strength in shear testing. In additional tests [33], it was found that bead-on-plate hybrid welds with 100% (253 MPa) joint efficiency could be produced using this hybrid welding process. Additional sections were also studied that exhibited the instability of the laser when used individually and conversely, the low penetration of the lone TIG welding process. The combination of the optimized hybrid welding parameters greatly increased the overall penetration. This was attributed to stabilization of the laser keyhole by the welding arc.

Low-power lasers do not have sufficient power to maintain stable keyholes when used alone and require the application of additional processes to achieve consistent and repeatable

weld profiles. High-power lasers are becoming more available in industry, and with greater power, could overcome some previous limitations thereby allowing their application to the welding of magnesium.

Leong *et al.* [7] were one of the first to publish studies on Nd:YAG and CO_2 laser beam welding of AZ31B in 1998. Using a pulsed 2 kW Nd:YAG laser, they found that high power density lasers produced very narrow weld bead profiles with negligible heat affected zones. The welds did suffer from other inherent difficulties associated with welding magnesium using high power density processes. The surface tension was identified as a source of weld bead defects and the low melting points and high vapour pressures of both magnesium and zinc lead to bulk material loss. They estimated the room temperature absorptivity of the magnesium alloy was approximately 3% and that the laser had to be limited to 0.8 kW for acceptable bead surface qualities to be achieved. When using the 6 kW continuous wave (CW) CO_2 laser, they claimed to be unable to fully penetrate the 1.8 mm sheet regardless of the power or travel speed used. The inability to weld with the CO_2 laser was attributed to the oxidized surface, which was broken up when welded with the Nd:YAG laser, but remained intact with the CW CO_2 laser welds. They reported optimized parameters were achieved using 0.8 kW peak power pulses and 30 mm/s welding speed for the pulsed Nd:YAG laser and using 2.5 kW power and 127 mm/s welding speed for the CW CO_2 laser.

Zhu *et al.* [34] compared the benefit of using a 2 kW CO_2 laser and a 1.5 kW diode laser when welding 1 mm thick AZ31B sheet. Both lasers were reported to achieve full penetration over a wide variety of parameters but suffered from bulk material loss, macro-porosity, and solidification cracking. The diode laser was found to reduce the amount of

porosity because it operated in conduction-mode welding. Both weld profiles were reported to have negligible heat affected zones.

Pan *et al.* [35] presented the results of a weld parameter optimization study when using a 500 W pulsed Nd:YAG laser and 1 mm thick AZ31 magnesium alloy sheet. The optimization was conducted using Taguchi's grey rational analysis technique to reduce the required number of test samples. The laser pulse energy and pulse profile were identified as the critical parameters, where the higher power output delivered in pulses with up-sloped intensities and abrupt cut-offs produced the highest-quality joints. The fully-optimized weld samples achieved 142 MPa ultimate strength when tensile tested.

Quan *et al.* [36] noted a transition in solidification mode from a columnar-to-equiaxed dendritic structure in their CO_2 laser welded fusion zones. In further studies by Quan *et al.* [5], a softened zone at the periphery of the fusion zone was found, but no heat affected zone or partially molten zone were observed in AZ31 CO_2 laser welds. Cao *et al.* [37] used a 4 kW CW Nd:YAG laser to weld 2 mm thick ZE41A-T5 sheet in a butt-joint configuration. They were one of the first to show distinctive hydrogen porosity formations along the fusion zone boundary, and liquation cracking in an identified heat affected zone. They found a softened heat affected zone that was many times larger than the weld fusion zone.

Yu *et al.* [38] conducted trials on 4 mm thick AZ31 with a fibre laser up to 8 kW laser power. The transverse sections presented both a CET and grain coarsened HAZ from the conducted welds. The welds were approximately 1.1 mm wide with the central 40% displaying an equiaxed dendritic structure. The HAZ was identified visually without

hardness profiles to corroborate the findings. With their optimized parameters at 4 kW laser power and 4 m/min welding speed, the welded samples achieved an ultimate tensile strength of 260 MPa. They conducted texture mapping for the different regions of the weld and found while the base material and columnar dendritic structures display a strong texture along the (0001) basal plane, the equiaxed dendritic structure show no texturing.

Research of the weldability of magnesium alloys is still in the early stages. The majority of the research has been performed on alloys that were created specifically for the sake of research and not on commercially-produced products that have received production heat-treatments. In terms of quantifying the weldability of magnesium through the applications of laser beam welding processes, only initial research into diode lasers [34] and fibre lasers [38] have been reported. The majority of magnesium laser welding research has been confined to keyhole-mode welding processes like Nd:YAG [7, 35, 37] and CO_2 [5, 36] laser systems. For most of the published research, only superficial or partial explanations are provided as to what constitutes a high quality weld or how inconsistent weld bead profiles affect mechanical properties of the welds.

Chapter 3
Experimental Apparatus and Procedures

Three different types of lasers were used in this study to investigate the weldability of magnesium alloy AZ31B-H24. The first laser was a 4 kW high power diode laser at the University of Waterloo, Waterloo Ontario, Canada. The viability of creating a laser seam welded butt joint with a conduction-mode laser welding process was investigated along with subsequent improvements to the process. The second laser was a 5 kW CO_2 laser at Promatek, Brampton Ontario, Canada. The keyhole-mode laser welding process was investigated and optimized for travel speed with this high power density welding process. The final laser used was a 10 kW fibre laser at IPG Photonics, Novi Michigan, United States

of America. The fibre laser welding trials were optimized for both travel speed and power using this high power density welding process.

3.1 Experimental Material

For this study, 2 mm thick AZ31B-H24 magnesium alloy sheet provided by General Motors (GM) was used. The AZ31B sheet was hot rolled and annealed to 50% or half-hardness. This processing left a coherent dark grey oxide layer on the surface. This layer was similar to the oxide layers studied by Ghali *et al.* [1]. The composition of the as-received AZ31B was measured with a Thermo Scientific Niton XL3t XRF Analyzer at the University of Waterloo. Table 3-1 lists the measured values for the AZ31B and the nominal concentrations as stated by ASM [2, 39]. The measured values all fall within the nominal ranges for AZ31B. The aluminum is used in the alloy due to its properties as a reducing agent. This helps prevent excessive magnesium oxidation [32]. Manganese is most commonly added as a grain refiner to promote nucleation of a final equiaxed grains during solidification [39, 32]. The manganese was found in the form of solid particles in the alloy. This led to high variability in concentration measurements. The measured locations were statistically on the low end of acceptable element concentrations but the values were still in the acceptable range. The controlled elements specified by the standards were not found in any of the measurements because they were below the resolution of the XRF analyzer. In magnesium alloys, the concentrations of elements like iron are important to limit in order to prevent the formation of additional undesirable intermetallics that reduce the mechanical properties and corrosion resistance of the alloy [3].

Table 3-1: Nominal composition (taken from ASM [2, 39]) and measured AZ31B alloy composition in wt%.

AZ31B	Al	Ca	Cu	Fe	Mn	Ni	Si	Zn	Mg
Standard	2.5-3.5	0.04	0.05	0.005	0.20-1.0	0.005	0.10	0.6-1.4	Bal.
Measured	2.73	--	--	--	0.375	--	--	0.915	Bal.

In Figure 3-1, a representative section of the base metal shows banding of larger grain sizes in the base metal of primarily equiaxed grains. The presence of dark grey manganese particles can also be seen dispersed throughout the alloy. With a melting point of 1244 °C, the manganese would remain solid in a molten magnesium bath since the melting point of magnesium is only 650 °C. Magnesium's boiling point of 1090 °C would also not be sufficient to melt the manganese particles. The manganese particles were generally less than 10 μm in diameter with only an occasional large particle exceeding 50 μm. These particles also effect solidification during welding by breaking off dendrite arms along the solidification interface. If these detached arms do not re-melt, they assist the manganese by providing heterogeneous nucleation points for equiaxed grains in the weld pool.

Figure 3-2 and Figure 3-3 show the binary phase diagrams for magnesium alloyed with aluminum and zinc, respectively. With a composition of 2.73 wt% aluminum and 0.915 wt% zinc, these phase diagrams indicate that the AZ31 will solidify with a single phase α-Mg material. $Al_{12}Mg_{17}$ or Al_3Mg_2 intermetallics may form at the grain boundaries during non-equilibrium solidification or when the alloy is allowed to approach equilibrium below temperatures below about 200 °C [39].

AZ31 received a rating of 'high weldability' by ASM for arc welding processes [20]. It is less susceptible to solidification and liquation cracking compared to other commonly

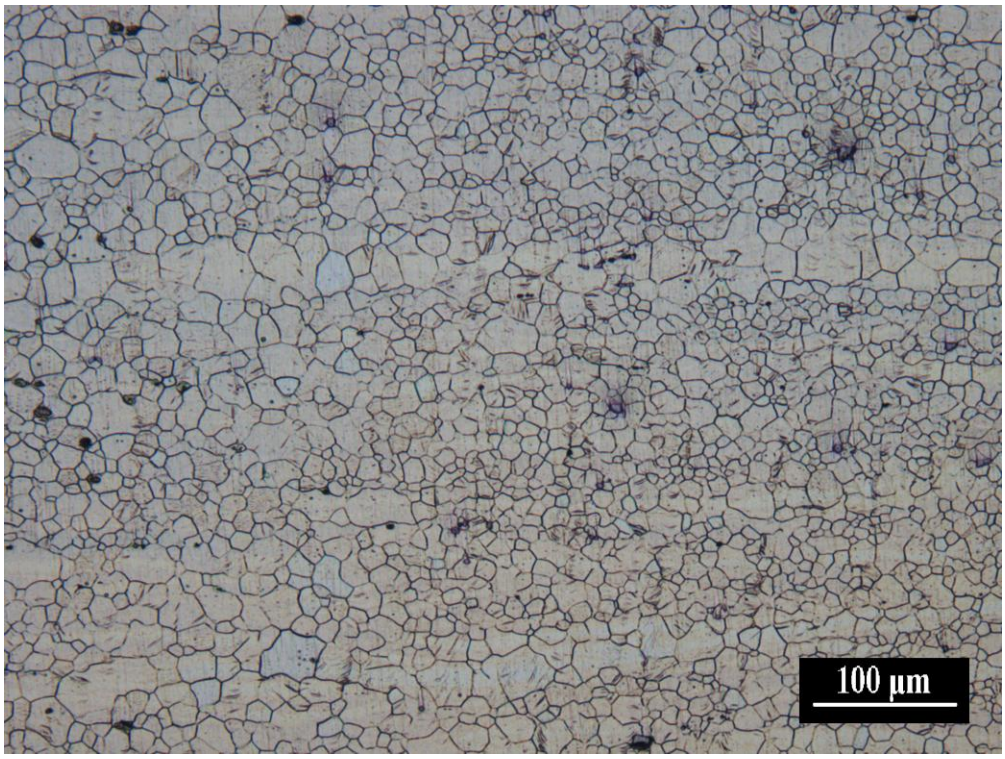

Figure 3-1: AZ31B-H24 base metal microstructure.

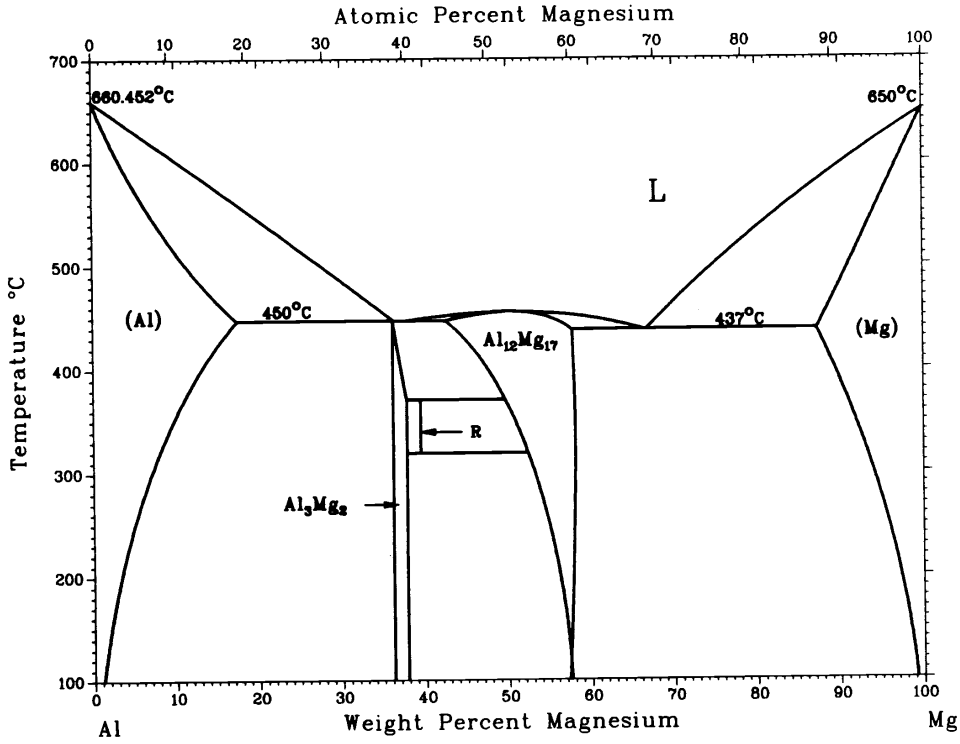

Figure 3-2: Aluminum magnesium binary phase diagram taken from ASM [39].

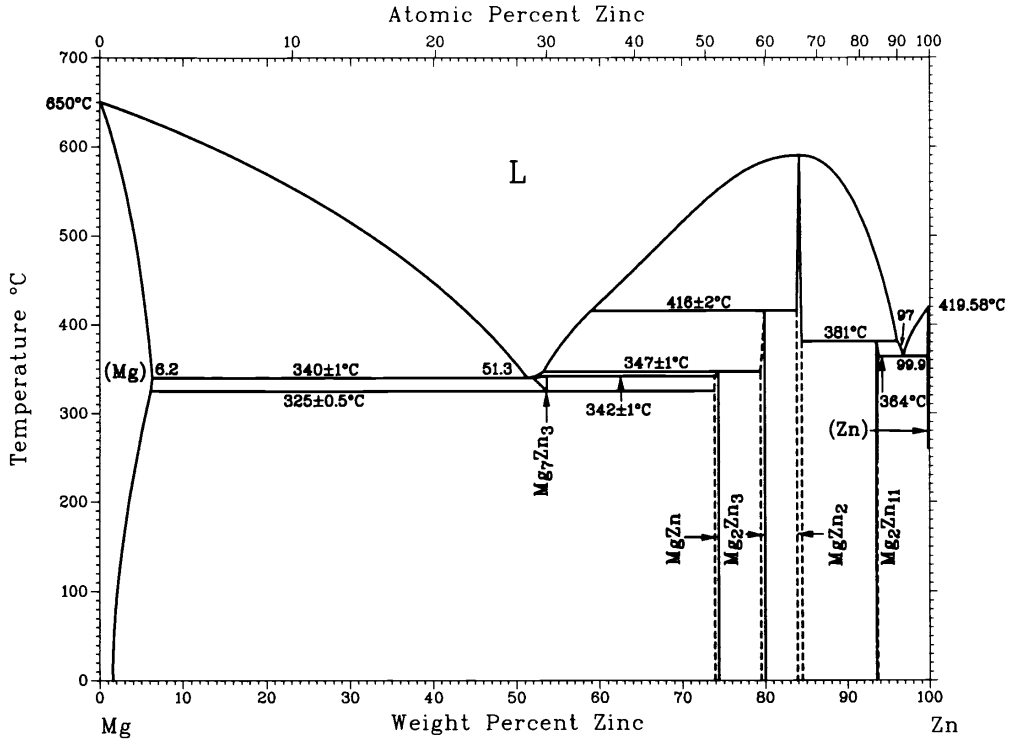

Figure 3-3: Magnesium zinc binary phase diagram taken from ASM [39].

available magnesium alloys. Thus, AZ31B was the alloy chosen to be used in this study to determine the laser weldability of magnesium alloys.

3.2 Sample Preparation and Analytical Procedures

3.2.1 Sectioning and Cleaning

Full 1220 mm × 405 mm sheets of 2 mm thick AZ31B-H24 was provided by General Motors (GM), USA. This sheet material was sectioned into sample weld coupon sizes using a Tennsmith T52 pneumatic shear. This process resulted in a shear edge faying surface such as shown in Figure 3-4a. If left as is, the lip on the faying surface would enable gas pockets to be entrapped and prevent the shielding gas from expelling it. The sheared surface also led to a high amount of variability in the surface so that when two samples were brought together, they would often have gaps occurring intermittently along the length of the seam.

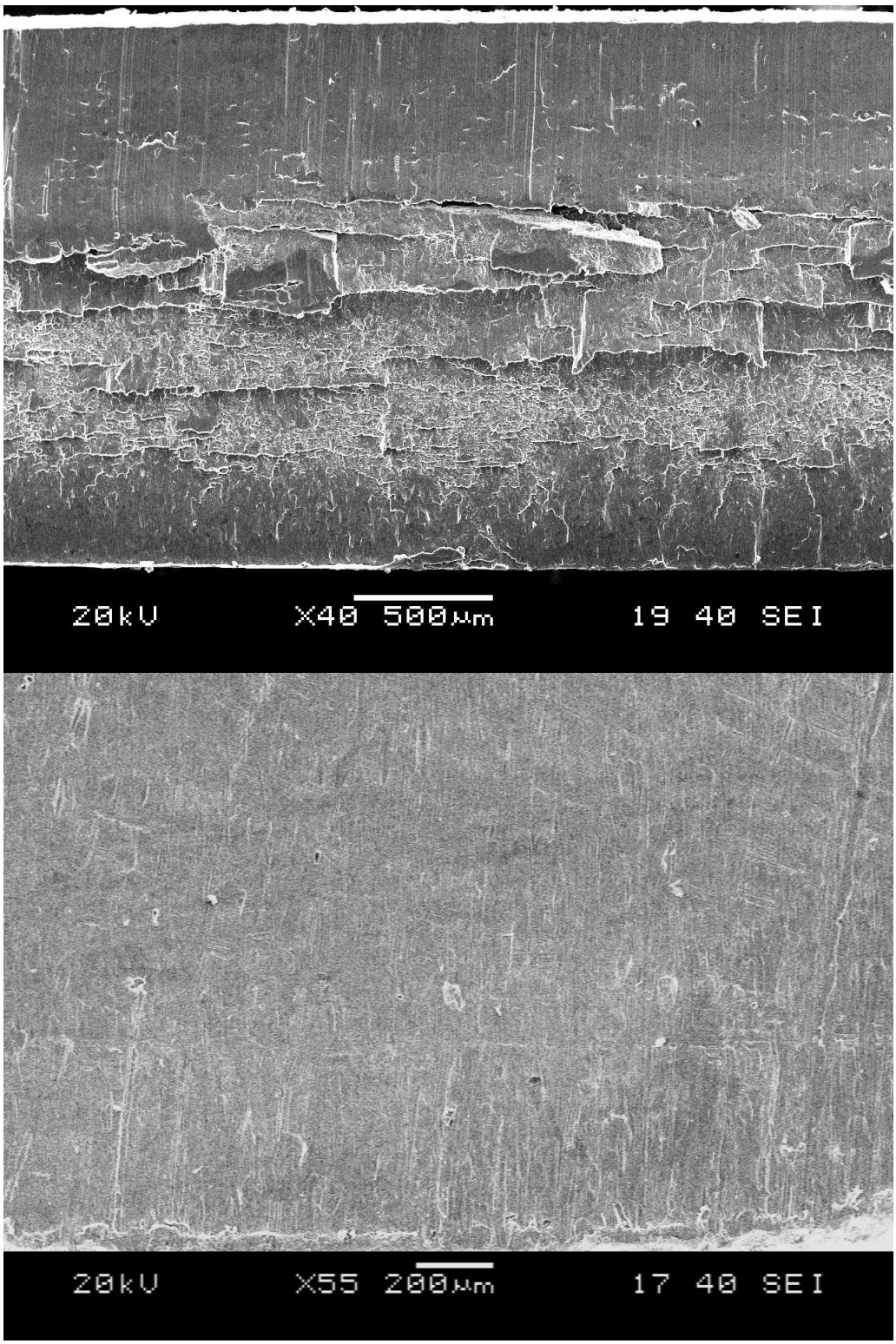

(a)

(b)

Figure 3-4: Edge surface of 2 mm thick AZ31B sheets: a) sheared joint interface surface and b) sheared and then milled interface surface.

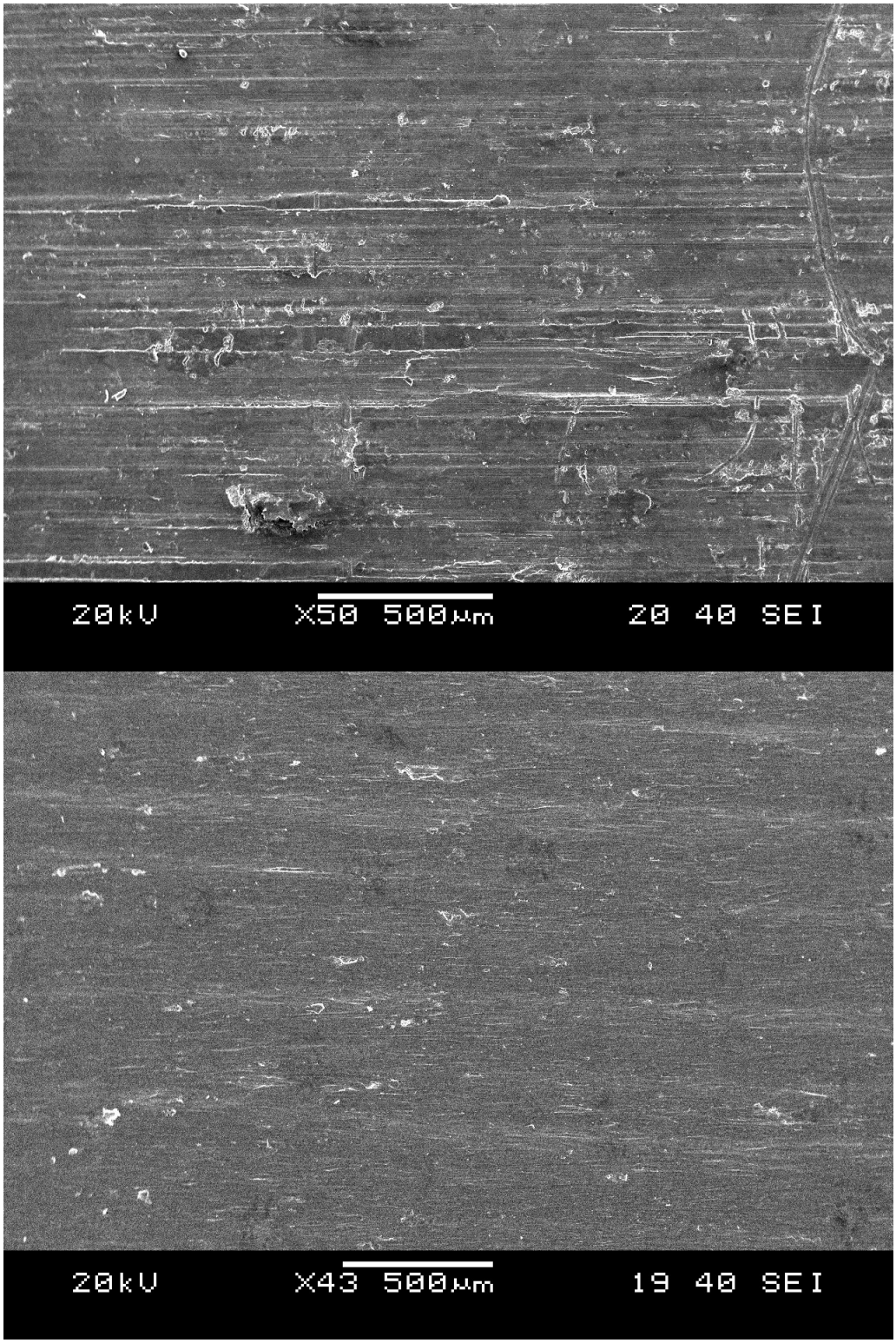

(a)

(b)

Figure 3-5: Magnesium sheet surface conditions: a) as-received with thick dark grey oxide layer and b) after degreasing and stainless steel wire brushing.

These gaps would potentially allow the laser to pass through the seam without any incidence on the sample, especially with the much narrower spot size of the CO_2 and fibre laser beams. As a rule of thumb, the fit-up gaps in laser welded butt joints must not exceed 5% of the materials thickness [9]. To ensure a joint fit up below this recommended 5% (0.1 mm) gap tolerance, the faying surfaces were machined using a First LC 20V SG milling machine. Figure 3-4b shows the machined surface. The machined surfaces provided a very flat and plane surface with excellent fit-up when the samples were clamped together for welding. With the samples cut to size and the joint prepared, they could be stored for an extended time without significant degradation.

The 'as received' magnesium sheet, seen in Figure 3-5a, had a dark grey coloured surface oxide layer. Prior to welding, this surface was cleaned with acetone and ethanol to remove any oil, grease, and loose surface contaminants. The surface oxide layer was removed by wire brushing with an 8" electric table-mounted bench grinder fitted with a stainless steel wire brush attachment with 0.3 mm diameter wires. The cleaned surface can be seen in Figure 3-5b and compared to the original surface shown in Figure 3-5a. The samples were welded within 30 minutes of cleaning to ensure that no surface contamination or oxidation would be introduced into the weld pool. If a sample was left for longer than 30 minutes without being used, the cleaning process was repeated prior to welding. If surface contaminants such as oils or grease were not removed, they would be burned off during the laser welding process, introducing oxygen, hydrogen, and nitrogen into the molten weld pool. These elements would readily react with the molten magnesium to produce oxides, hydrogen porosity, or nitrides in the final weld. The reacted surface layer was the

more important substance to remove during cleaning, since the hydrated oxides often entrap other contaminants. Hydrogen contamination occurs when hydrocarbons, moisture, or hydrated oxide in the oxide layer dissociates during welding. Similar to aluminum, the solubility of hydrogen in molten magnesium is high while the solubility limit for hydrogen in solid magnesium drops significantly during solidification. Figure 3-6 shows the measured solubility of hydrogen in magnesium versus temperature. At the solidification temperature, the solubility decreases by approximately 25% [40]. This decrease of solubility causes the nucleation and growth of hydrogen pores if hydrogen contamination had occurred in the weld [10].

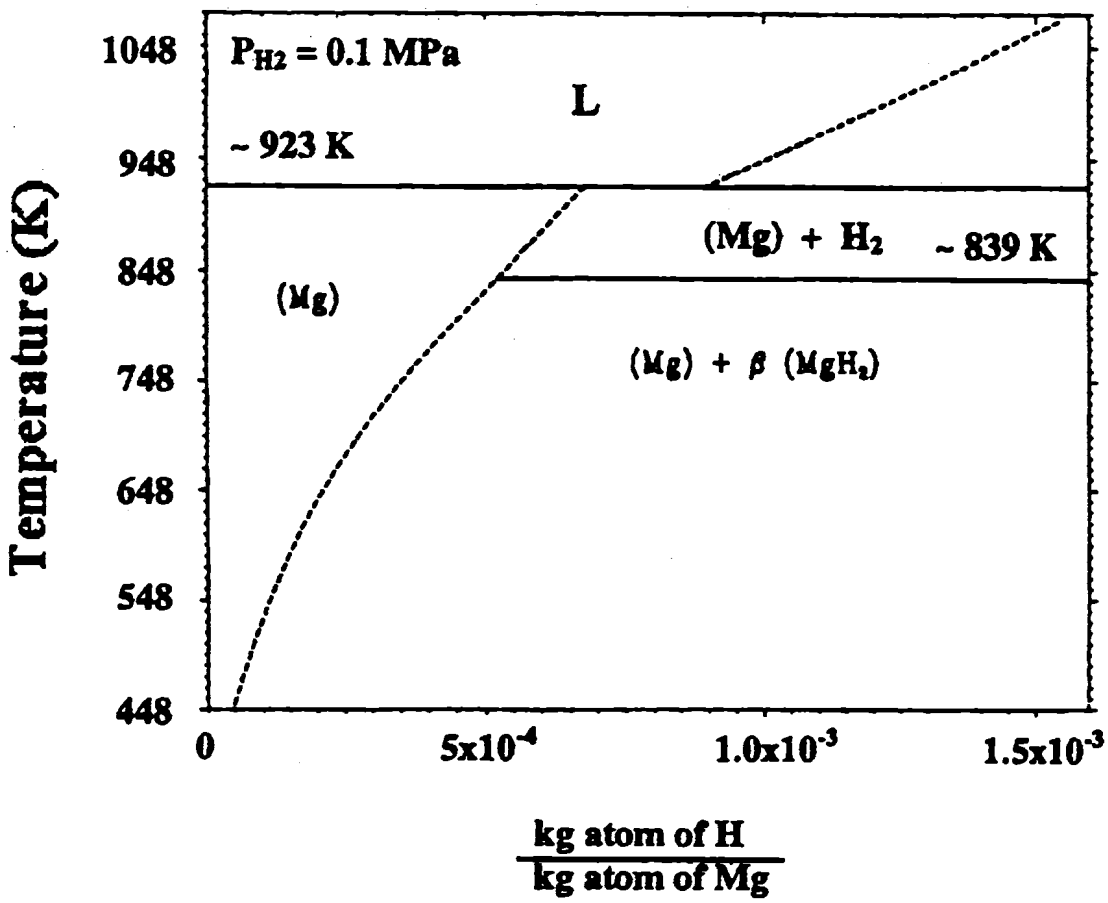

Figure 3-6: Hydrogen solubility in magnesium (taken from Zhao and DebRoy [40]).

3.2.2 Mounting and Etching

Once the weld samples were completed, they were sectioned for microscopic analysis and testing of physical properties. Microscopy samples were taken at random from the length of the weld such that the first and last 20 mm of the weld were excluded as the weld would not have been at steady-state conditions in these regions. The sections were then mounted in Struers Epo-Fix epoxy compound in 38 mm diameter cups. A plane surface of the sample was achieved with a belt grinder and the specimens were then ground with a series of water-lubricated silicon carbide papers to achieve a smooth surface. The original sample preparation summarized in Table 3-2 was used for the initial two experimental series involving the diode laser. The coarsest grit grinding paper was a 320 grit, progressing to 600, 800 and then to the 1200 grit papers. Polishing was conducted with Leco DP-red oil-based lubricant and 1 μm and 0.25 μm diamond spray particles.

Table 3-2: Original grinding and polishing schedule.

Step		1	2	3	4	5	6	7
Surface	Type	SiC Paper #320	SiC Paper #600	SiC Paper #800	SiC Paper #1200C	SiC Paper #1200F	MD-Nap	MD-Nap
	Speed (RPM)	300	300	300	150	150	150	150
Abrassive	Type						DP-Susp. 1 μm	DP-Susp. 1 μm
Lubricant	Type	Water					DP-Red	DP-Red

The final diode trials, Experimental Series D, and all CO_2 and fibre laser trial samples were prepared with the schedule summarized in Table 3-3 received from Struers [41]. This alternative method of polishing required fewer stages to achieve a finished sample and resulted in a reduction of non-uniform scratching by switching from oil to ethanol-based lubricants. The samples produced with the Struers method also achieved a higher surface quality by using an equal mixture of ethanol and colloidal silica final stage to achieve a

plane, scratch-free surface. From these polished samples, cracks, pores, and other defects were identified if present. The samples were then etched to expose the sample microstructure with a picric etchant. The solution was a combination of 6 g picric acid, 10 mL glacial acetic acid, and 100 mL ethanol [1]. The required etching time to expose the weld grain structure was approximately 45 seconds.

Table 3-3: Grinding and polishing schedule as proposed by Struers [41].

Step		1	2	3	4
Surface	Type	SiC Paper #320	MD-Largo	MD-Dac	MD-Chem
	Speed (RPM)	300	150	150	150
Abrassive	Type		DP-Susp. A. 9 µm	DP-Susp. A. 3 µm	OP-S, 0.004 µm
	Prelevel		2	2	
	Level		3	3	
Lubricant	Type	Water	DP-Blue	DP-Blue	Ethanol
	Prelevel		3	3	
	Level		5	7	
Holder	Force (N)	30/	30/	30/	25/
	Direction	>>	>>	>>	>>
	Speed (RPM)	150	150	150	150
	Time	00:45	05:00	04:00	02:00

3.2.3 Microhardness Measurement Procedure

Hardness measurements were conducted to determine if any softened regions had resulted from the welding processes and to determine the size of the heat affected zone. For all hardness data measurements, a Shimadzu HMV-2000 indenter was used with an inverted square pyramid diamond indenter. The resulting hardness indent was measured with an Olympus BH2-UMA light microscope. To analyze the repeatability and accuracy of data points, a simple trial was conducted to determine the optimal test load. When using very high loads, the data points were representative of the material's average hardness as each indent interacted with a greater volume of equiaxed grains and manganese particles, thus

decreasing the effect of localized variances in the microstructure. Conversely, the very light load trials interacted with a much smaller volume and would identify local hardness variances that the higher loadings would mask. Figure 3-7 shows a plot of the measured microhardness versus indenter load for a 15 s indenter dwell time. As the load was decreased, the measured readings increased and the scatter gradually became extreme. The very light load trials allowed for very fine resolutions, but the repeatability of the data became scattered as high power optics were required for the software to measure the indents. At a loading level of 25 g, the small size of the microhardness indent was sufficient for good test resolution while the measurement scatter was minimized. From the literature, 50 g is the most common Vickers microhardness loading weight [7, 8, 33] with extremes of 10 g [42] and 500 g [24, 43] also being used. Neither 25 g nor 50 g loading trials provided a representative bulk material hardness and the difference between them was a slight

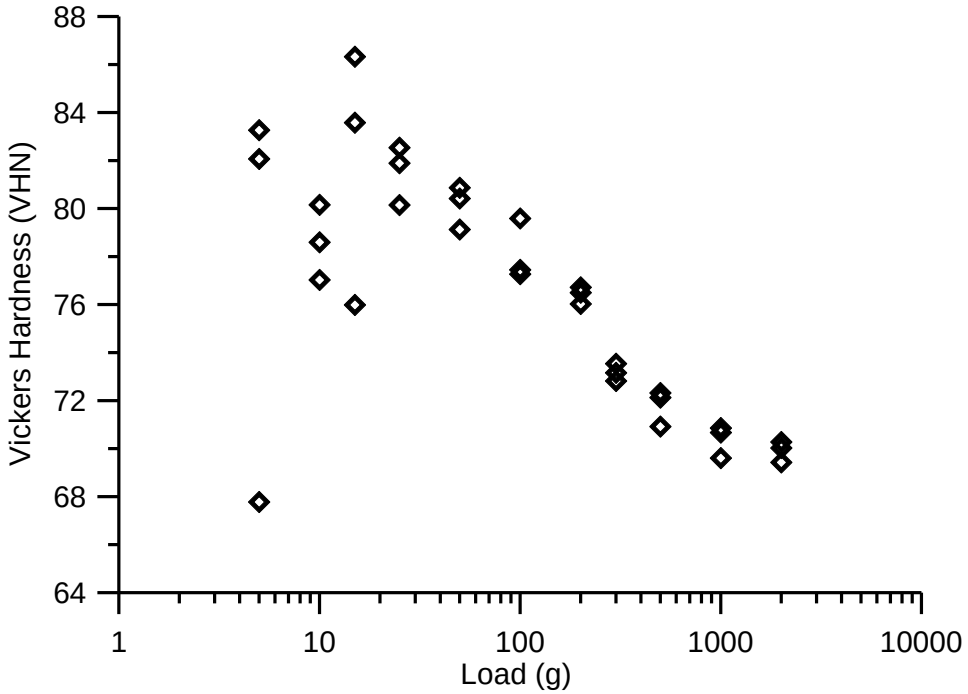

Figure 3-7: Measured Vickers hardness versus indenter loads for a 15 s dwell time.

discrepancy in the resulting hardness with the 25 g loading affecting a much smaller area. Therefore, the micro-hardness tester was set at 25 g load with a 15 s dwell time was used for all micro-hardness measurements.

3.2.4 Tensile Testing Procedure

Tensile trials were conducted to determine the yield strength, ultimate tensile strength, and elongation to failure for both the base metal and the welded specimens. The tensile specimens were sectioned with the Tennsmith shear and machined using the First milling machine. All samples were prepared to conform to ASTM standard full-size rectangular tensile samples Section B557-06 [1] seen in Figure 3-8. All specimens were welded transverse to the base material rolling direction. The tensile test coupons were machined to be in line with the original rolling direction with the transverse weld along the centre of the tensile coupon. These transverse tensile specimens were tested to failure using a lead-screw type Instron tensile testing system located at the University of Waterloo, Ontario, Canada.

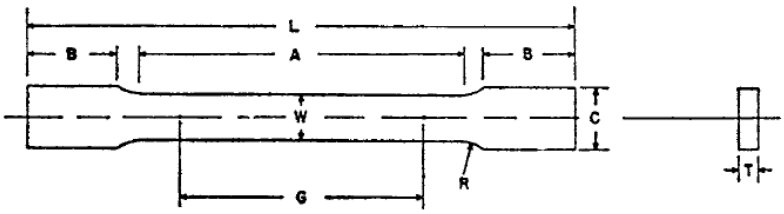

	Dimensions, in.	
	Standard Specimen Sheet-Type, ½-in. Wide	Subsize Specimen ¼-in. Wide
G—Gage length	2.000 ± 0.005	1.000 ± 0.003
W—Width (Note 1 and Note 2)	0.500 ± 0.010	0.250 ± 0.002
T—Thickness (Note 3)	thickness of material	thickness of material
R—Radius of fillet, min	½	¼
L—Overall length, min (Note 4)	8	4
A—Length of reduced section, min	2¼	1¼
B—Length of grip section, min (Note 5)	2	1¼
C—Width of grip section, approximate (Note 2 and Note 6)	¾	⅜

Figure 3-8: ASTM B557-06 tensile specimen standards (taken from ASTM [1]).

3.2.5 Scanning Electron Microscope Imaging Procedure

All Scanning Electron Microscope (SEM) images were made with a JOEL-640 SEM located at the University of Waterloo, Ontario, Canada. The SEM was used to take high quality images where a large depth of field was required such as fracture surfaces, or where grinding and polishing would not be possible such as when imaging the material's surface conditions.

3.3 Diode Laser Welding Experiments

3.3.1 Diode Laser Welding Apparatus

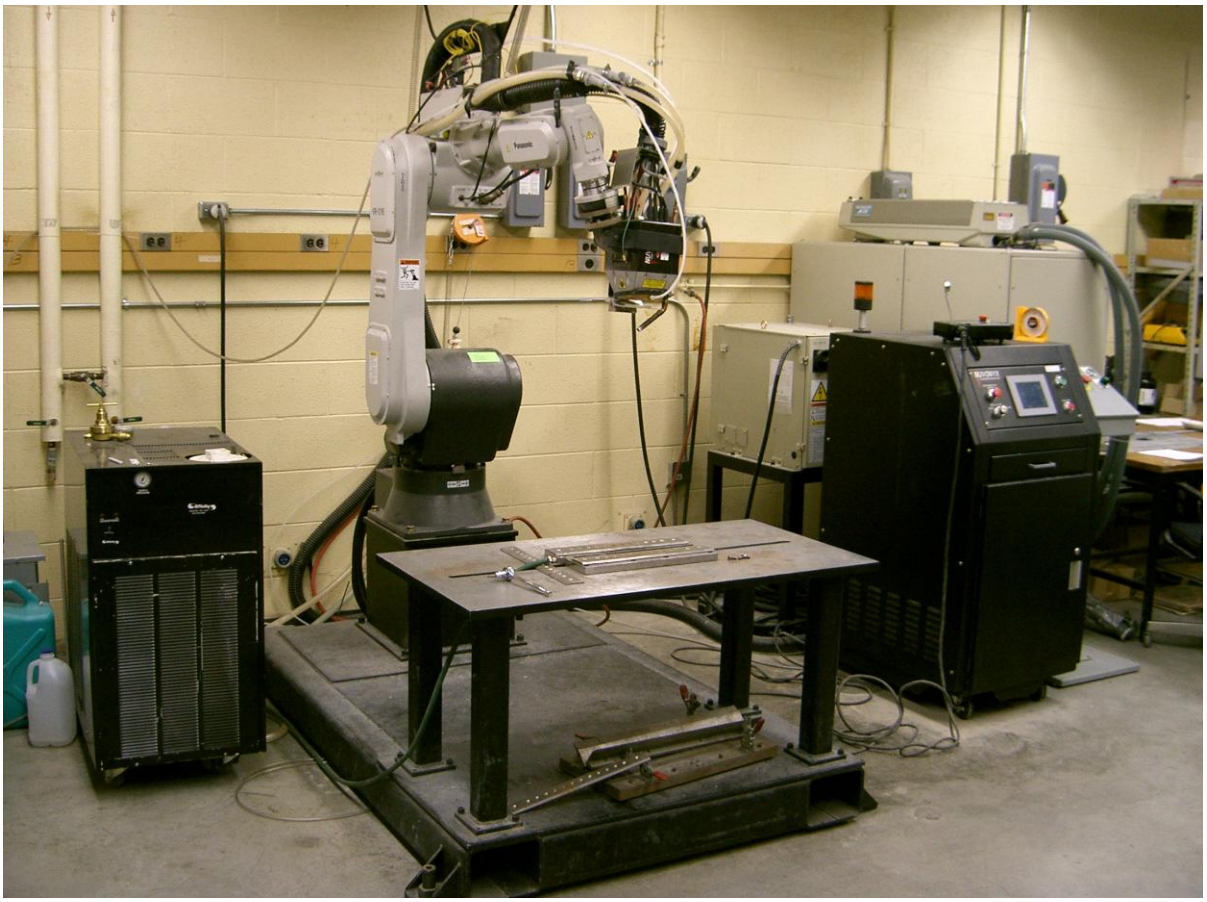

Figure 3-9: The Nuvonyx ISL-4000L 4 kW diode laser, controller, Panasonic 6-axis robotic arm, chiller, and welding table and clamps.

The diode laser welding system shown in Figure 3-9 was comprised of several distinct components; the laser head, a control unit, operation pedestal, water chiller, power supply, robotic arm, work table, and shielding gas system.

3.3.2 Diode Laser Procedure

The diode laser used was a Nuvonyx ISL-4000L AlGaAs solid-state 4 kW laser. The laser was a compilation of four separate diodes arrays. Each bank of diode arrays comprised of twenty separate diodes were individually powered and controlled. Figure 3-10 shows a schematic diagram of how the diode were arranged and focused to a single laser beam. The configuration of the diodes leads to the laser's characteristic rectangular shaped beam and intensity profile at the focal spot. The laser beam has a wave length of 805 ±5 nm. A single 90 mm focal length process lens and optically flat protective glass were used which resulted in a nominal spot size of 0.9 mm by 12 mm [12]. This permits the diode laser beam to achieve a nominal power density up to 37 MW/m^2. The laser's primary heat control system was a water chiller which circulated distilled water cooled to 19° C. Hydrocarbon-free dry air was fed into the laser head to prevent moisture from condensing in the laser head. All welds were conducted with a 7° pulling angle of travel. This tilting of the incident laser beam was done to prevent any serious back reflection from the work piece back into the laser head. The entire laser was operated and monitored by the control system which would turn the laser on and off and control the laser power output up to the laser's maximum of 4 kW. Laser powers below 0.5 kW were not used because the system experienced instability when operating below 10% of its rated limit [44].

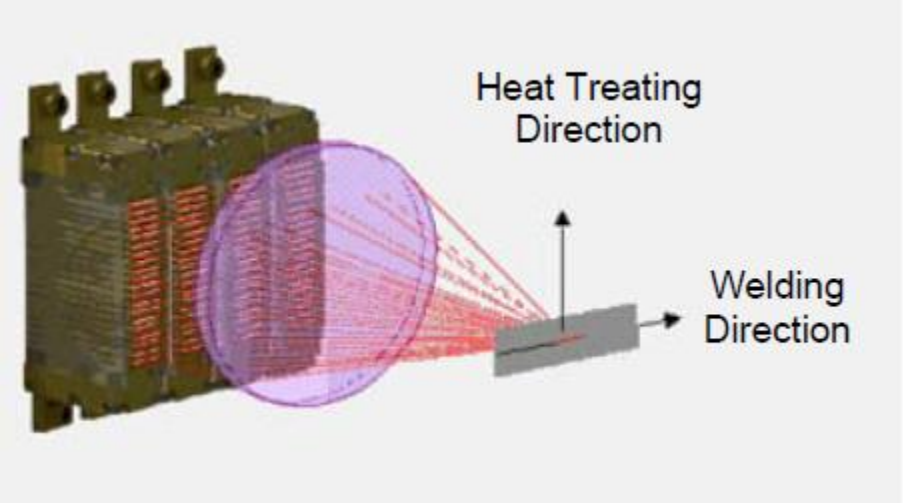

Figure 3-10: Diode array arrangement taken from Howard [12].

3.3.3 Diode Laser Robotic Arm and Fixturing

The diode laser was mounted to a six-axis Panasonic VR-16 robotic arm. The arm's software was programmed to be operable with any one of several different devices including mechanical tools, arc welding torches, or lasers. When the robotic arm was extended to its full reach of 1.7 m, it was rated to operate with a maximum payload of 16 kg. The diode laser and attached shielding apparatus had a working load of approximately 9 kg. The robot's motion was limited by the joints maximum rotational speeds and the complexity of the motion it was programmed to perform. Of the six axes used to produce motion of the work tool, the primary three joints were capable of rotational speeds up to 142 °/s while the smaller joints were able to achieve rotational speeds up to 300 °/s [44]. The robotic software provided motion smoothing between the programmed key points to prevent joint damage, since at full speed, the arm could theoretically traverse over 3.0 m of its 3.4 m diameter reach in one second. In operation, the robotic arm had a positional accuracy rated at ±0.1 mm [44].

3.3.4 Diode Laser Controller

The diode laser welder control unit shown in Figure 3-9 was a combination touch-screen and pendant interfaced PLC system with four current control units, one for each of the diode array banks. The operation pedestal acted as an extension of the PLC controller when used during welding to allow the operator to manually initiate or stop the welding process. The controller monitors the safe operation of all components to ensure the laser was not damaged during usage. The distilled water chiller was monitored for water level and temperature and if the distilled water became warmer than 20° C, a system interlock prevented operation. The controller also monitored the laser head for acceptable dew point temperature and relative humidity to ensure that the dry air purge was operating. This is a Class IV laser. Therefore, door safety interlocks were required. These were tied into the control system to prevent unaware individuals from entering the room and being exposure to the laser beam.

The laser was programmed in 'teach mode' using the pendant interface tool with which the system was programmed with key positions for the robotic arm to follow. These points were compiled by the PLC to provide the arm with a series of motions to execute when operated. The software automatically determined which joints were operated to carry out the programmed tool motions when the laser beam was triggered, and controlled the activation of the air knife which protected the lenses from weld spatter and dust accumulation. A Cartesian coordinate system was used to program the robot's motion with the end wrist joint remaining fixed to maintain the laser head position relative to the welding focal point.

The laser's focal position was determined using cross-hair sights projected by two perpendicular Class II He-Ne laser pointer line segments. When the laser was out of focus,

the line segments would not intersect, but when properly focused on a surface, they produced a cross pattern. Prior to welding, the laser would be focused by eye on the upper surface of the sample. If the laser needed defocusing into or out of plane of the surface, the computer controlled software was used to accurately move the robotic arm from the known zero point. The smallest increment the laser could be moved was 0.05 mm, where all measurements were relative to the initial surfaces zero point. Due to this possible limitation, a trial was conducted to determine the reproducibility of accurately setting the zero point. The laser was focused several times with absolute locations measured each time. After repeating this process 6 times, the difference in focal positions was not more than ±0.15 mm.

3.3.5 Diode Laser Clamping Fixtures and Shielding Gas

In the overall welding setup shown in Figure 3-9, the metal base plate was secured with bolts to the concrete floor. The robotic arm and the welding work table were both attached to the metal base plate to keep them rigid with respect to each other. Figure 3-11 shows a solid model of the weld specimen clamping fixture that was bolted onto the welding table and used for all diode laser experimental trials. The laser welding jig was made from 20 mm thick plain carbon steel and had a 20 mm wide and 15 mm deep channel cut down the center to provide space for a backing bar or shielding gas along the root side of the weld. There was a 34 mm gap between the two clamps during welding. Welding trials were attempted with larger and smaller gaps. Larger gaps resulted in an intensification of solidification cracking during welding and the smaller gaps caused interference with the thermal evolution of the weld.

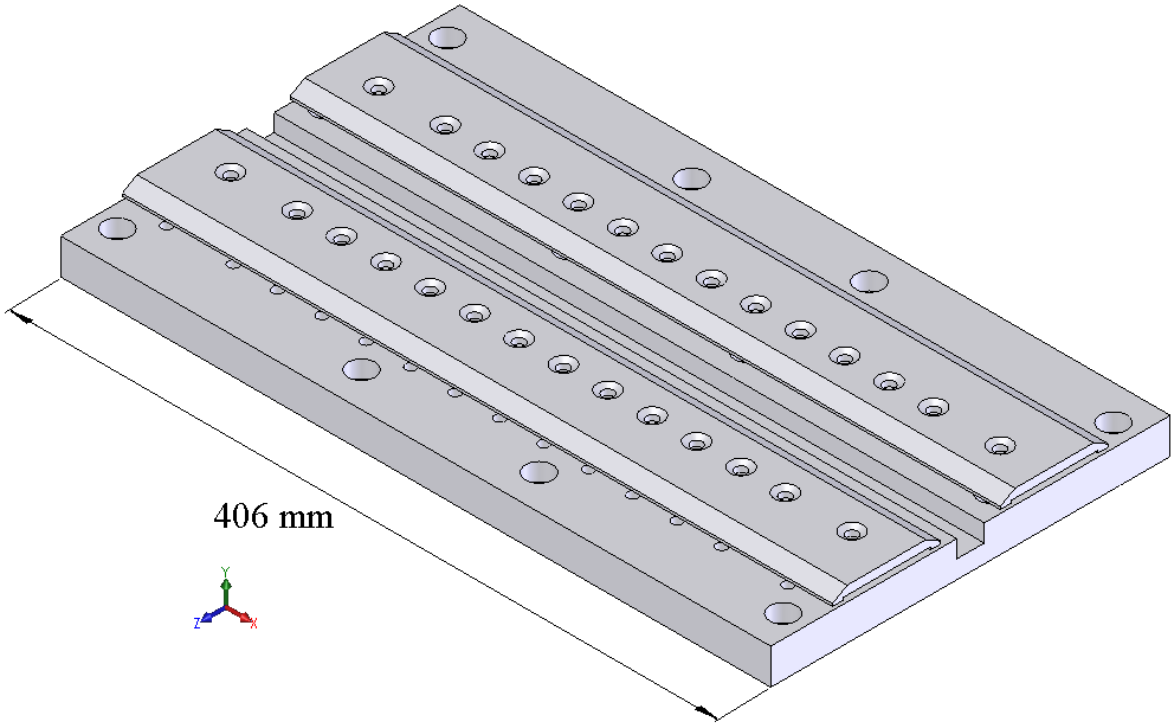

Figure 3-11: Solid model of the clamping fixture.

All welds, except where noted specifically, were shielded with helium gas from independent sources from both the top and the bottom root side. The channel along the root side provided excellent shielding with a 12 l/min (25 SCFH) flow along the specimen in the direction of welding. The entry of the channel was fitted with a gas hose fitting and caulked to prevent leaks. With the lack of baffles or points of entrapment to allow contamination combined with helium's natural buoyancy, the gas was thought to flow in a laminar fashion along the root of the sample before exiting to atmosphere.

The top of the weld did not have an enclosed environment to purge with shielding gas since access by the laser was required. This necessitated a more complicated apparatus to provide shielding. On the upper surface, the buoyancy of helium works against forming a

coherent barrier. Initial experiments were performed with a 14 mm inner diameter copper tube shielding device that provided a flow of helium from behind the weld at a 60° push angle against the direction of travel as was used by Howard *et al.* [12, 45] for diode laser welding of aluminum alloy sheet. This proved to be inadequate for the more reactive magnesium alloy sheet used in the recent study, therefore, a new shielding device was designed to meet the special requirements associated with producing diode laser welds. Figure 3-12 shows a drawing of the coaxial shielding gas nozzle that was designed and made for these experiments. The shielding apparatus provided an input for shielding gas to be fed through the cavity of the system and was attached to the laser head with previously created mounting points. The top of the shielding system had a bore cutout to accommodate an optically flat glass which permitted the laser beam to pass through, but prevented the shielding gas from escaping. Figure 3-12 shows a schematic of the laser head and shielding apparatus with a 7° inclination maintained to prevent harmful back reflections into the laser head. The shielding gas is delivered co-axially with the laser beam through the device. The shielding gas was delivered to the work piece through a final rectangular orifice measuring 15 mm by 32 mm at a flow rate of 35 l/min (75 SCFH). This allowed a helium shielded environment to be maintained on the top surface of the work piece that encapsulated the area of the weld. A front and side profile view of the anticipated shielding gas flow is illustrated in Figure 3-13 with the projected shielding flow path overlaid. In this situation, the close proximity of the shielding nozzle to the clamping bars acted to channel the exhaust helium primarily along the axis of the weld providing additional pre- and post-weld shielding. While the same flow rate was used for both shielding systems, the new apparatus imparted a much lower normal force to the weld pool compared to the higher exit velocity associated

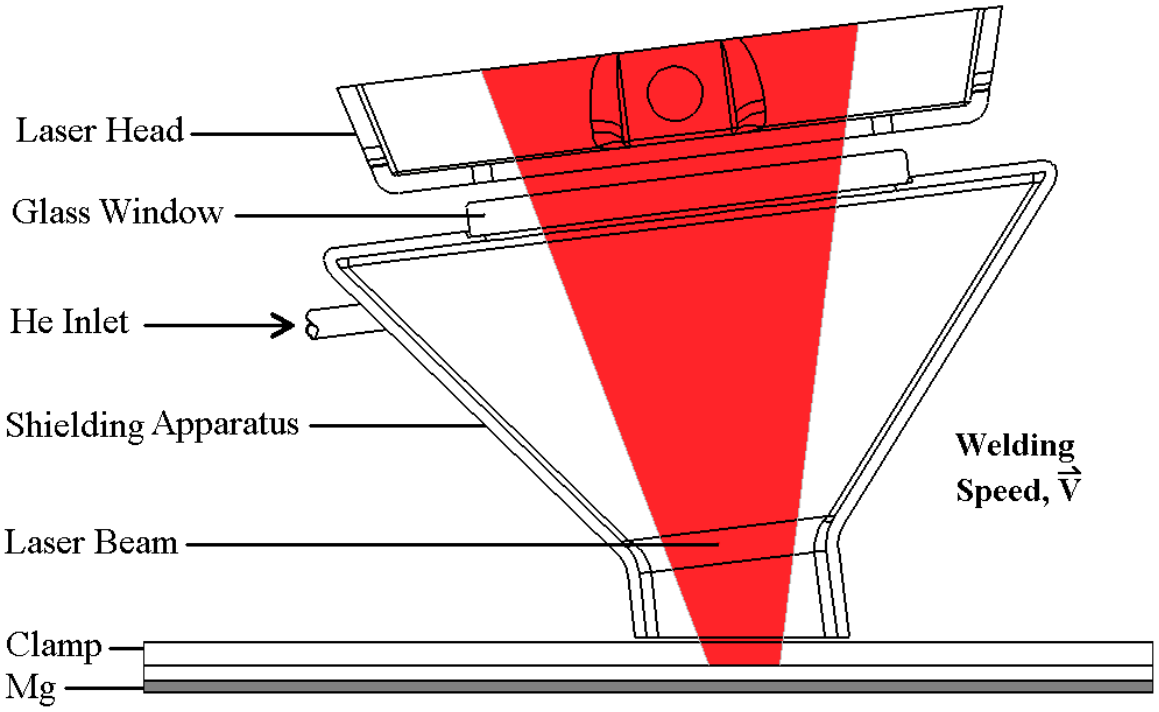

Figure 3-12: Diode laser head co-axial shielding gas apparatus.

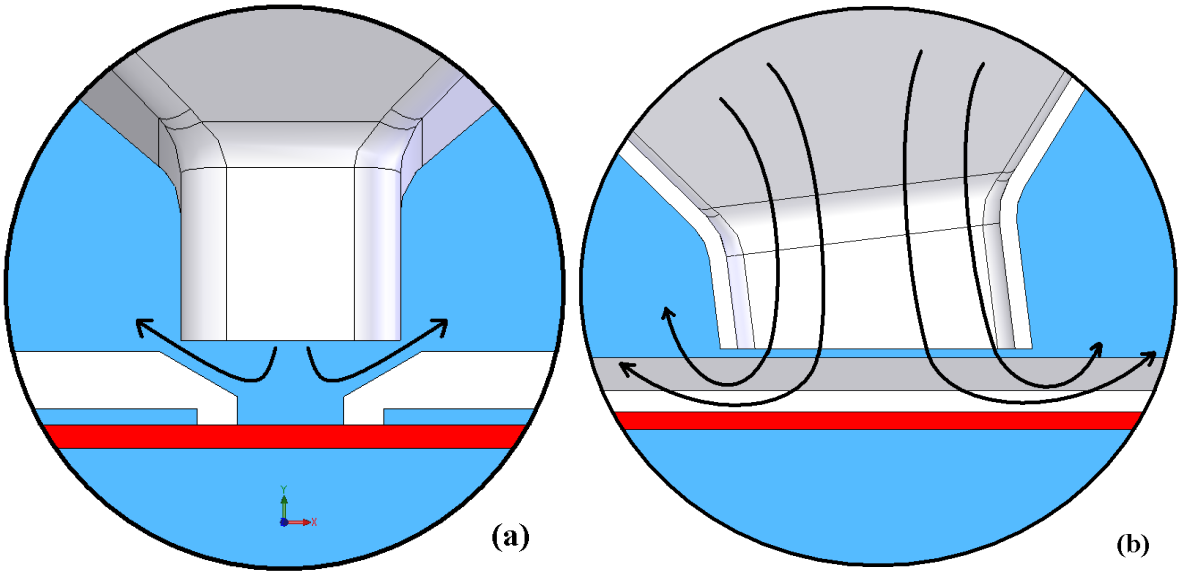

Figure 3-13: Expected helium shielding gas flow diagram for co-axial helium top shielding: a) front view and b) side view.

with the initial smaller cross-section of the copper pipe apparatus. A step-by-step procedure for operation of the robotic diode laser welding system may be found in Appendix A.

3.3.6 Diode Laser Experimental Trials

3.3.6.1 Experimental Series A

Initial diode laser welding experiments were conducted by making bead-on-plate welds on the AZ31B sheet in the as-received condition. The as-received material surface condition had a heavy layer of grey oxide present and this was not removed in Experimental Series A. The only cleaning that was done was to degrease the surface with acetone. Trials on the oxidized surface were conducted to determine if welding the material in the as-received state could produce a high quality, consistent, full-penetration weld. In this first series of trials, the travel speed was varied from 1.0 m/min up to 4.5 m/min in 0.5 m/min steps. The power was maintained at 4 kW, the laser was focused on the upper surface of the sheet and the sample was shielded with argon gas from a 14 mm ID copper pipe to the top of the weld only at a flow of 35 l/min (75 SCFH).

3.3.6.2 Experimental Series B

A second set of full factorial welding trials was conducted on the as-received samples in which laser seam welds were made on a butt-joint using a range of travel speeds and welding powers. For this series of trials, the joint interface was a sheared interface and the specimens were arranged in a butt joint configuration with inverted shear cut surfaces to allow a tighter joint fit up. Figure 3-14 shows a diagram depicting the two joint configurations where the interface was cut using a shearing process. With the mirrored shear faces, the average distance between the samples increases and the possibility of having sections with gaps

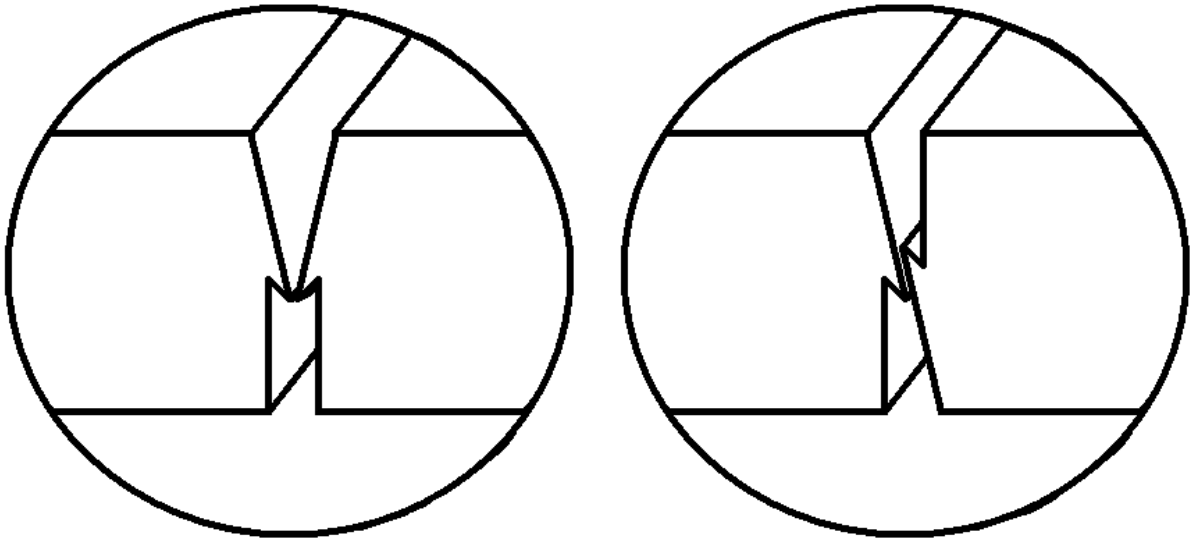

(a) (b)

Figure 3-14: Butt joint with: a) mirrored and b) inverted shear surface interfaces.

through the thickness becomes increased. As shown in Figure 3-14, the gaps between the two samples was reduced when the specimen's sheared interfaces were inverted. The improved shear joint configuration assisted in the laser beam absorption and overall joint efficiency. The inverted shear joint configuration was implemented for all welds involving sheared joint interfaces.

This series of experiments was designed to determine the effect of weld power and travel speed on the resulting weld quality. The travel speed was incremented from 1.0 m/min through 5.0 m/min in 0.5 m/min steps. These travel speeds were each tested with three different laser powers: 2, 3, and 4 kW. From Experimental Series B forward, helium was used as the shielding gas instead of argon because it has a higher ionization energy [9], and because it has been reported to increase the mechanical properties and surface quality of magnesium welds [35]. The same copper pipe shielding gas system from Experimental Series A was used for the top shielding again at 35 l/min (75 SCFH). Back shielding was

added to prevent oxidation on the reverse side of the weld and to help flush out the joint interface of contaminating gasses. The back shielding was set at a flow of 12 l/min (25 SCFH) through the root side channel in the jig.

3.3.6.3 Experimental Series C

In this experimental series, the samples were prepared with a weld joint interface that was sheared and then milled to remove any joint inconsistencies or gaps. This resulted in flat joint interfaces that provided excellent congruency and eliminated the contaminating gas pockets along the seam. In addition, stainless steel wire brushing was used to remove the surface oxide layer and expose the base metal. The samples were then individually cleaned with acetone and ethanol and blown dry with dry air to ensure a contaminant free surface. The shielding device used for Experimental Series B was replaced with the redesigned co-axial shielding gas system described previously in Section 3.3.5. All other welding parameters were held constant from Experimental Series A so that comparisons could be made between the cleaned and as-received conditions to determine if better joint preparation and surface cleaning played a role in the weldability of the AZ31B sheet.

3.3.6.4 Experimental Series D

This final series of diode laser welding trials was a full factorial series of tests where the power and travel speed were both varied. The sample preparations and shielding was maintained identical to Experimental Series C. The power was set at 2, 3 and 4 kW. For each power level, weld trials were conducted at travel speeds of 0.5, 1.0, 1.5, and 2.0 m/min. This experimental series was conducted to determine the weldability of the AZ31B sheet with optimal controllable parameters, joint and surface preparations.

3.4 CO_2 Laser Welding Experiments

The CO_2 laser used in this study was a high power density continuous wave (CW) gas laser. It was comprised of a power supply, robot controlled laser head, control device, and shielding gas system.

3.4.1 CO_2 Laser Apparatus and Procedure

The CO_2 laser used was a TRUMPF TLC-1005, and like all CO_2 lasers, operated with a wavelength of 10.6 μm. The focal distance and nominal spot size of the CO_2 laser were 160 mm and 300 μm, respectively. The much smaller spot size allowed the CO_2 laser to achieve a power density of over 70 GW/m^2 at full power, over 1000 times more intense than the diode laser. The CO_2 laser beam was projected to the work piece through the use of high precision mirrors. All welds were conducted with the laser beam delivery head tilted to a 5° pushing angle to reduce the amount of harmful back reflection from the weld surface into the laser head.

3.4.2 CO_2 Laser Mount and Controller

The CO_2 laser power supply and lasing material were not stored in the head of the device like the diode laser but was separate from the laser beam delivery head. The CO_2 laser beam was conveyed from the laser to the weld specimens via high precision mirrors. This externalization of the lasing material leads to a much lighter and more compact welding head. The laser beam delivery head contained the final focusing lenses and an air knife to protect the lens from weld spatter. The laser beam delivery head was mounted on a three-axis gantry system so that it was free to move in space above the work surface where the

sample was clamped. The controller was used to set key points and automate the laser operation during welding. The control system also managed the operation of the air knife.

3.4.3 CO_2 Laser Fixtures and Shielding

The fixture used for clamping all of the CO_2 laser weld specimens was the same system used in the diode laser experimental series. See Section 3.3.5 for detail concerning the jig dimensions, applications, and implementations.

Helium shielding gas was used during all CO_2 welding trials and was fed to both the top and root side of the weld. It was maintained at a combined 70 l/min (150 SCFH) and purged for 10 s prior to each weld to prevent shielding gas contamination. The gas was fed from a single source and was divided by a T-junction to two 6 mm ID polyurethane tubes with separate down flow control valves. One line was used to shield the root side of the weld with a contained cross flow and the other line was fixed to the laser head. Figure 3-15 depicts the general arrangement of the CO_2 laser trials where the top shielding moved with the laser head at a 45° pushing angle and was positioned to provide localized shielding to the molten pool during welding. Trial welds were conducted to determine the relative division of shielded because the flow rates were not individually measured for the top and bottom flow rates, only manually adjusted. Once determined, the same flow was used for all trials and was set-up such that it provided preferential shielding to the top surface of the weld. During the welding trials, the shielding gas was not automated and required manual activation.

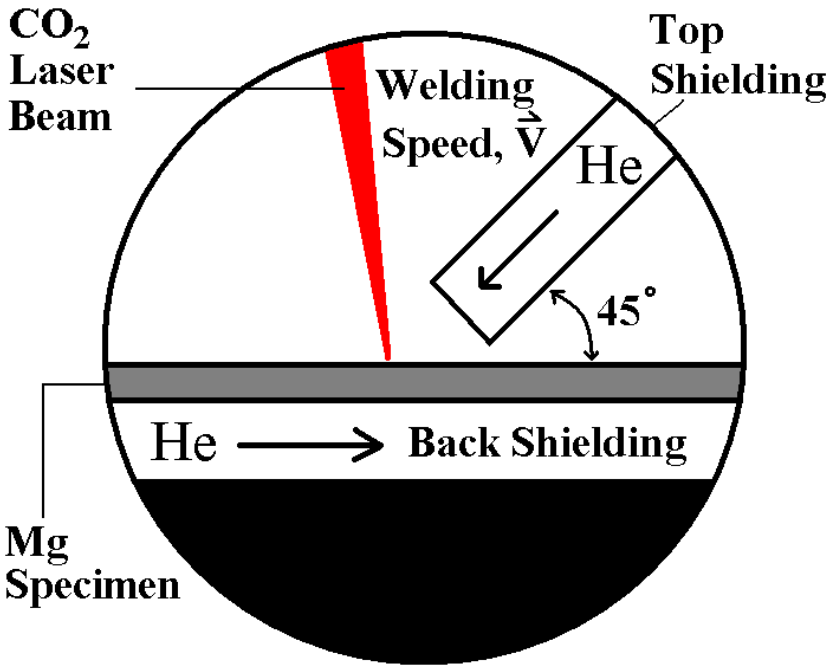

Figure 3-15: Schematic diagram of the CO_2 welding apparatus.

3.4.4 CO_2 Laser Experimental Trials

The CO_2 laser weld trials incorporated a single factorial series of welding trials to determine the effect of travel speed on the weldability of AZ31B by a high power density laser source. For all CO_2 laser weld trials, the power was held constant at 5 kW, the laser was focused on the top surface and with a 5° push angle to prevent back reflections. The travel speed was varied between 8, 10, 12, and 15 m/min to optimize the welding speed for a 5 kW CO_2 laser weld. The magnesium sheet samples used in the CO_2 weld trials were prepared similarly to the final diode laser samples. They were machined to improve the joint configuration and cleaned with acetone and ethanol.

3.5 Fibre Laser Welding Experiments

The fibre laser was the second of the two high power continuous lasers investigated. The fibre laser welding system is shown in Figure 3-16. Use of the fibre laser was provided by IPG Photonics, located in Novi, Michigan, USA.

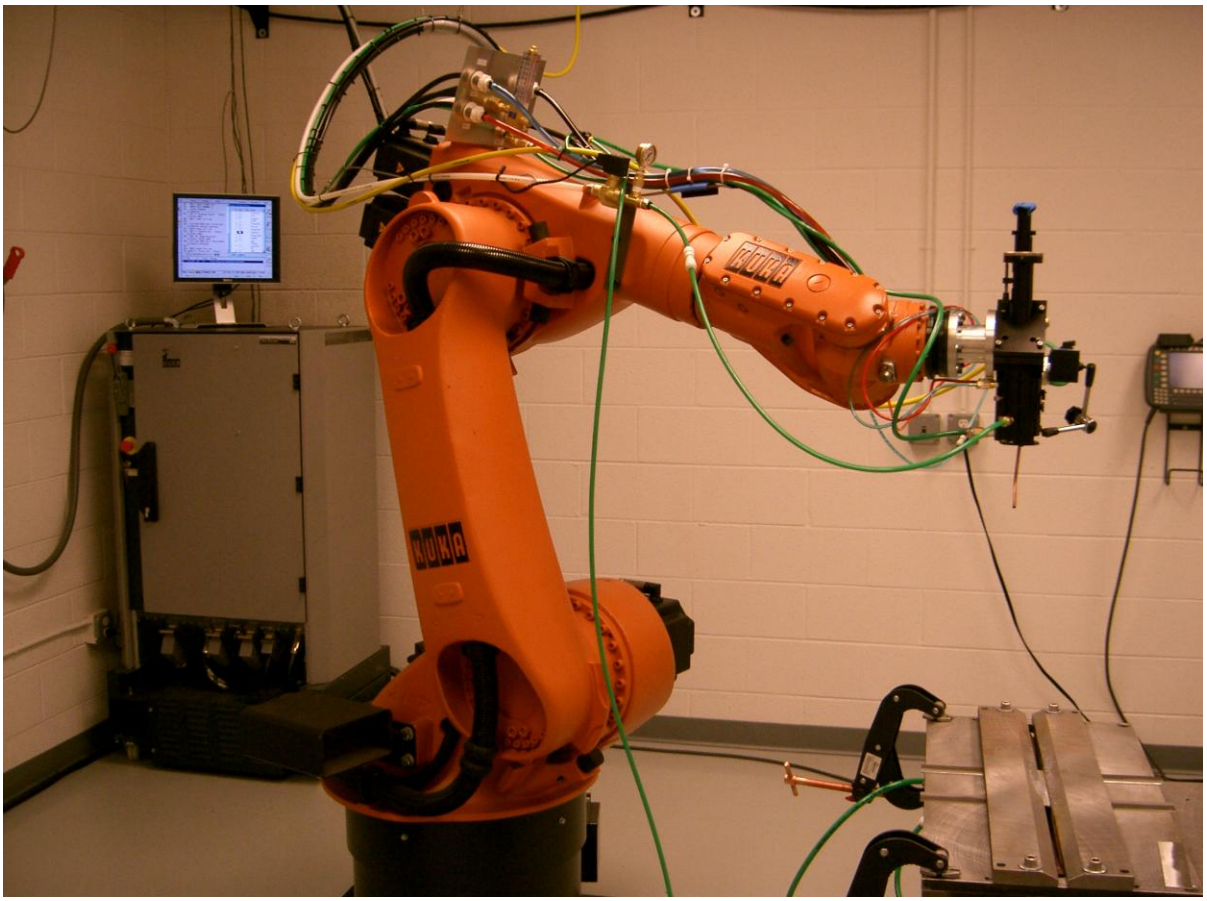

Figure 3-16: Fibre laser controller, KUKA robotic arm, mounted laser head, and welding table with clamping device.

3.5.1 Fibre Laser Apparatus and Procedure

The Fibre laser system shown in Figure 3-16 was comprised of the laser power supply, robotic arm, control system, shielding system, and clamping system. The 10 kW BIOM HIGHYAG laser was produced by Laser Technologie and was a model YLR-10000-WC fibre laser. This laser system produced a beam with wavelength between 1060 and 1070 nm

and a nominal spot size of 300 μm at the focal distance of 300 mm. Having the same spot size as the CO_2 laser, but twice the maximum laser beam power, the fibre laser could achieve a maximum power density of 140 GW/m^2. The laser was produced remotely from the site of welding and fed via a 600 μm fibre optic cable to the laser head. With the fibre laser being delivered to the work piece through fibre optic cable, the resulting laser spot was characteristically circular with a Gaussian distribution. To prevent damaging back reflections from the welding process, the laser was inclined at a 5° pushing angle. Both the laser operation and shielding system were automated to ensure consistent and repeatable welds were created.

3.5.2 Fibre Laser Robotic Arm and Fixturing

The robotic arm used to maneuver the fibre laser head was a KR-60-HA KUKA 6-axis robotic arm. This 6-axis robotic arm had a reach of 2.2 m, operating payload of 60 kg, and positional repeatability of ±0.15 mm. The three primary joints were capable of rotational speeds up to 120°/s while the three slowest of the secondary joints were rated for speeds of 245°/s [46]. The robotic software controls the sequencing of each joint to prevent any joint from running out at the end of travel. At full speed, the robotic arm was capable of traversing over 3.8 m of its 4.4 m full travel in a single second. Compared to the diode laser trials that were conducted at very slow travel speeds, the fibre laser welds progressed to speeds that were sufficiently fast that the robotic arm required a lead in to the welds to ensure that it had reached a constant travel speed before welding began. For this reason, the initial and final 20 mm of each weld were discarded due to the uncertainty of steady-state conditions had been achieved in those regions.

3.5.3 Fibre Laser Controller

The fibre laser was operated via a pendent-style interface similar to the one used to control the diode laser. Key points and welding parameters were programmed into the PLC system through the pendent and the software automatically controlled which joint was moved to achieve the required tool positions. The system was incorporated with safety protocols which would interrupt the welding process if tripped to prevent damage to individuals and equipment. The controller automated the turning on and off of the shielding gas and the air knife used during welding to ensure they were only operated when required. The focal point of the fibre laser was determined similarly to the CO_2 laser, the known focal distance was measured from the surface of the material to a hard point on the laser head to position the laser's offset distance and a Class II He-Ne laser was used to pinpoint the weld focal point.

3.5.4 Fibre Laser Clamping Fixture and Shielding Gas

The jig fixture used to secure the samples for fibre laser weld trials shown in Figure 3-17 was a variation of the jig used for previous trials. The clamping bars were bolted down at the ends without any spacers which resulted in deflection of the bars. This produced a positive inflection in the clamping bars when secured and prevented the clamp from making contact with the sample except at the two ends.

Helium shielding gas was used for all fibre laser welds. Shielding was delivered from both the top and root sides of the weld seam. The root shielding gas tube can be seen in Figure 3-17. During welding, the shielding gas was provided through a 3 mm ID copper tube

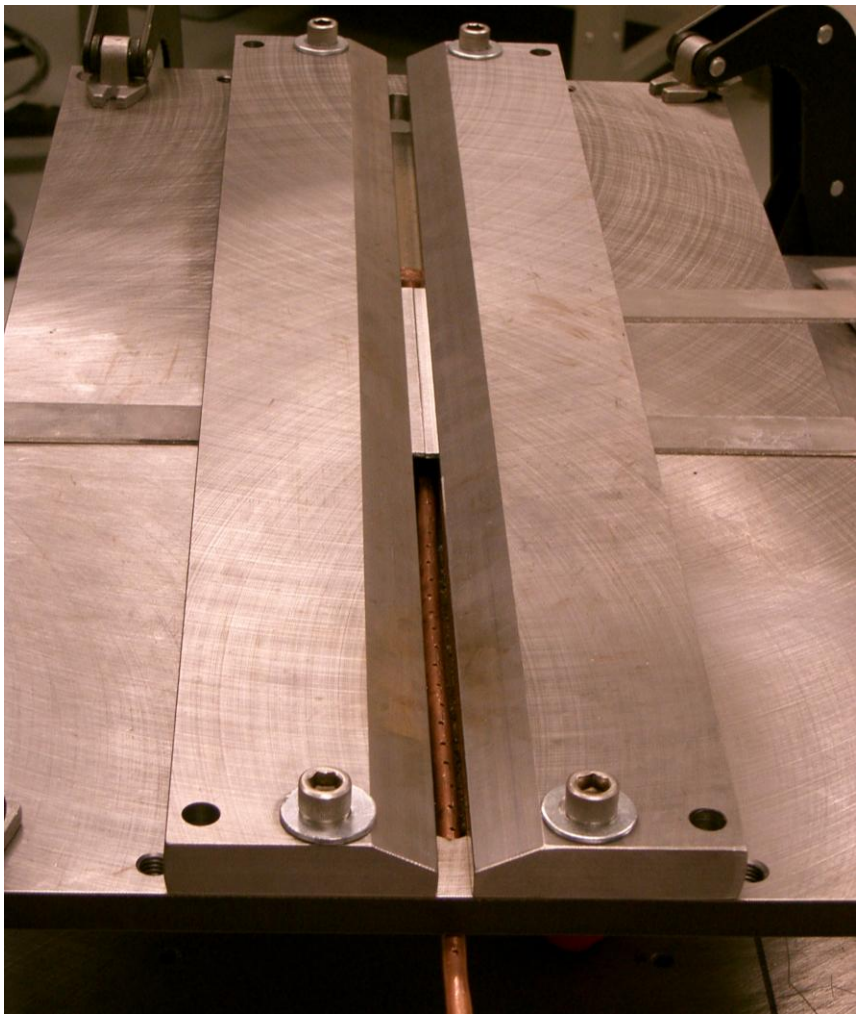

Figure 3-17: The fibre laser welding fixture with perforated copper tube used for back shielding.

with small holes drilled into it at 1 cm intervals along the entire length of the weld seam. Similar to the CO_2 laser shielding system depicted in Figure 3-15, except with the travel direction reversed, the shielding for the top surface was delivered across the weld from ahead of the weld at a 45° angel through a 3 mm ID copper pipe. All shielding gas was all delivered from a single supply at 80 l/min (175 SCFH) split by a T-junction between the top and root shielding tubes.

3.5.5 Fibre Laser Experimental Trials

With the fibre laser, a full factorial series of experiments was conducted to characterize the effects of both welding travel speed and laser power on weld quality. The laser power was incremented from 2.0 kW to 6.5 kW in 1.5 kW steps and the travel speed was similarly incremented from 50 mm/s through 300 mm/s in 50 mm/s steps. This resulted in 24 weld parameter combinations. The weld specimens were prepared in a butt joint configuration similar to the diode laser trials in Experimental Series D. The samples were sheared to size, machined flat, cleaned with acetone and ethanol, and stainless steel wire brushed prior to welding. For the welding parameter characterization trials, the edges of the samples were slightly chamfered by hand to remove machining burrs and sharp corners.

Chapter 4

Results and Discussion

4.1 Diode Laser Welding Results and Discussion

4.1.1 Experimental Series A

The initial diode weld trials were conducted at 4 kW power as bead-on-plate welds. The samples were shielded with a pushing cross flow of argon from the top but received no back shielding. Experimental Series A was used to investigate the relationship between travel speeds and weld quality when using the 4 kW laser at full power on samples with minimal surface preparation.

4.1.1.1 Weld Bead Surface Quality

Prior to welding, the weld specimens were degreased with acetone leaving the as-received grey oxide layer on the surface. Figure 4-1 shows the top and bottom surfaces of some of the conducted diode laser beam welded specimens where the welding direction

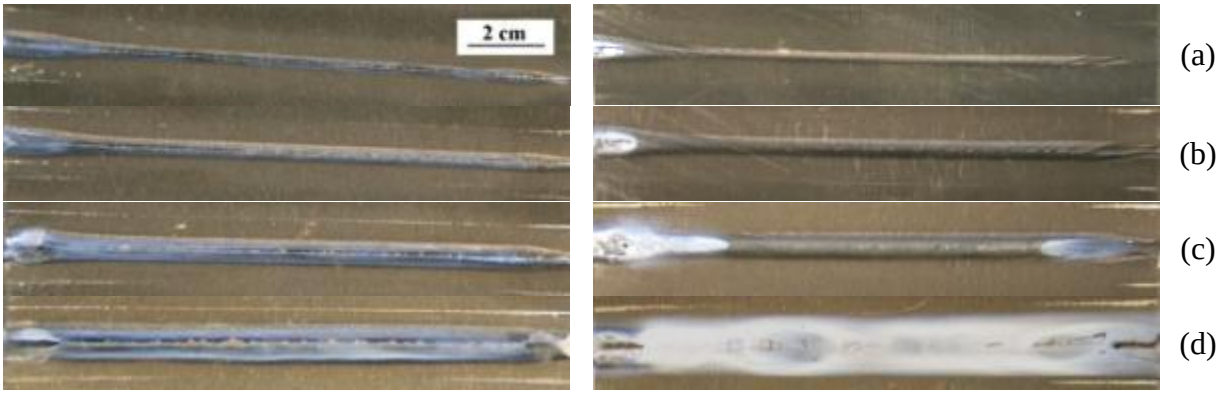

Figure 4-1: Top and bottom weld bead surfaces of bead-on-plate welds made using 4 kW at: (a) 4.0 m/min, (b) 3.0 m/min, (c) 2.0 m/min, and (d) 1.0 m/min.

progressing from right to left. The fastest travel speed of 4.5 m/min in Figure 4-1a was the limiting upper travel speed. Beyond this setting, the laser did not have sufficient power to produce a consistent full-penetration weld. At 0.5 m/min, the magnesium experienced sufficient heating to promote active boiling which disrupted the weld pool sufficiently to cause blowholes and melt-back in the weld.

This experimental series showed how the coherent grey oxide and hydroxide layer [1] remained intact and was not removed by the laser beam welding process even though melting of the underlying magnesium alloy occurred. A film of magnesium oxide soot produced during welding was observed on the weld surfaces as a white soot layer that was easily brushed off. All samples showed small quantities of further oxidation along the top surface, but the high travel speed welded samples showed heavy oxidation along the root side, since there was no additional protective back shielding. The appearance in only the low travel speed trials shows how effectively the existing oxide layer shielded the weld samples while it was intact. At the slow travel speeds below 1.5 m/min, the laser beam linear power density was increased sufficiently to cause active mixing and boiling of the weld pool. This

disturbance broke the coherent oxide layer and exposed the molten magnesium to the atmosphere where it reacted to produce the white soot. However, at travel speeds above 2.0 m/min, the original oxide was able to maintain a coherent layer that inhibited the reaction of the molten AZ31B with the atmosphere. All samples experienced disruption of the oxide layer on the upper surface where the laser was incident. The bead quality was similar in all samples with smooth surfaces devoid of cracks or solidification bands and reacted as expected to the alterations in travel speed. With the slower travel speeds, the laser beam line power density was increased and the resulting welds were able to maintain larger weld pools producing proportionally wider welds. Below 1.5 m/min, the original oxide was unable to expand to cover the entire fusion zone and this left an exposed seam along the centerline of unoxidized metal.

4.1.1.2 Weld Cross Section Analysis

For each of the performed weld samples, the weld metal area (WMA) and melted base metal area (MBMA) were measured. As illustrated in Figure 4-2, the WMA is the fusion zone area less any pores or significant cracks, while the MBMA is the actual cross-sectional area of the weld metal.

WMA is a useful value to quantify thermal fields and is easily measured. MBMA was used to calculate the weld efficiency and, in conjunction with the WMA, can be used to estimate the amount of vaporized material. When using the MBMA, it is assumed that the sample has obeyed a conservation of volume and that no contraction occurred in the fusion zone once the clamping force was released. Using the MBMA, the overall welding process

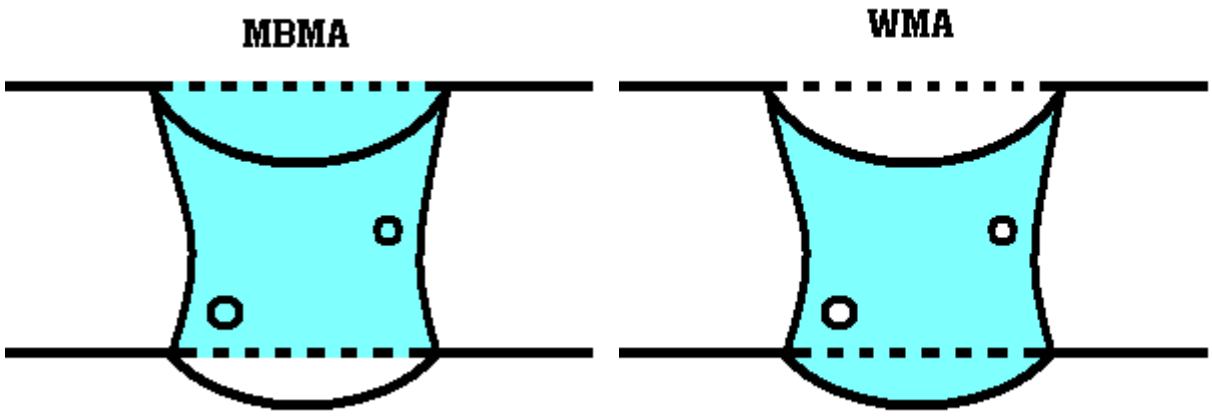

(a) (b)

Figure 4-2: Weld schematic depicting: a) the melted base metal area and b) weld metal area.

efficiency, called the melting ratio (MR) was calculated using Equation 4-1 taken from Deutsch [47] and the listed thermo physical material property values for AZ31 magnesium alloy were taken from the ASM Handbook [2]:

$$MR(\%) = \frac{100\left[(C_p(T_m - T_o) + H_f)\rho \bullet \text{MBMA}\right]}{\frac{Q}{v}} \qquad \textbf{(4-1)}$$

Cp = Specific heat (1.180 kJ/kg•K)
T_m = Melting temperature (923 K)
T_o = Room temperature (293 K)
H_f = Latent heat of fusion (340 kJ/kg)
ρ = Density (1.77 kg/m^3)
MBMA = Melted base metal area (m^2)
Q = Power (4 kW)
ν = Travel Speed (m/s)

From this calculation, the relationship of MR versus travel speed was determined and plotted in Figure 4-3. In calculating the MR, only the travel speed, ν, and the MBMA were variable and inversely related to each other. At approximately 3.0 m/min, the rate of change of these two variables was balanced and the overall MR was maximized when the weld

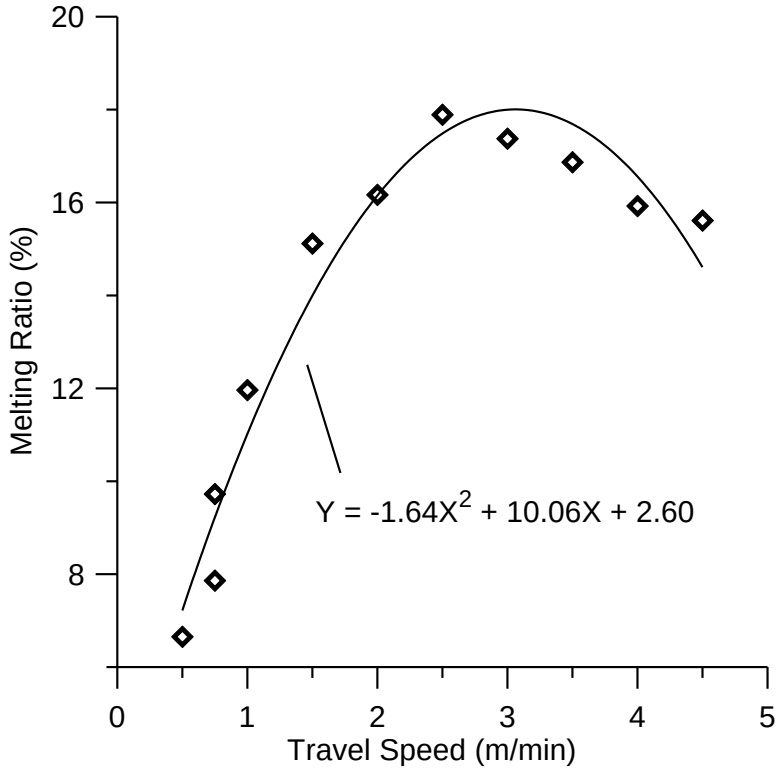

Figure 4-3: Diode laser melting ratio versus travel speed.

efficiency reached approximately18% or only 18% of the laser power was absorbed and used to heat and melt the magnesium sheet. The balance of the energy was lost due to reflection of the laser beam off the surface or due to conduction of heat into the surrounding material.

Transverse sections from each weld were taken and Figure 4-4 shows representative selections of the welds conducted on the 2 mm thick AZ31B sheet. The weld width decreased with increasing welding speed. The low surface tension of the molten magnesium alloy resulted in a significant drop through in all but the fastest weld travel speeds. The weld made at 3 m/min (Figure 4-4b) shows a dark region originating from the top surface being pulled into the weld pool. Like the manganese particles, the magnesium's original oxide layer remained solid during welding due to its much higher melting point of approximately 2800 °C [2]. During welding, the oxide layer on the upper surface was preferentially broken

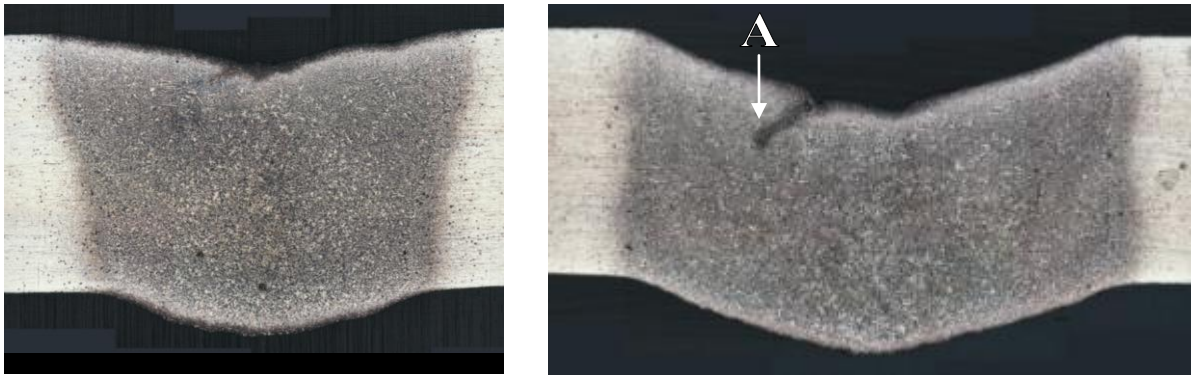

(a) (b)

(c)

(d)

Figure 4-4: Transverse sections of diode laser welds made at 4 kW and: a) 4 m/min b) 3 m/min c) 2 m/min and d) 1 m/min on 2 mm thick AZ31B.

by localized boiling during laser welding. These small disrupted particles of oxide were then pulled into the solidifying weld pool. This observed dark mixing region was most pronounced in the 3 m/min weld section but could also be identified in several other travel speeds to varying degrees. At 2 m/min, the weld experienced a greater degree of mixing and subsequent dispersion of the incorporated oxide is observed in the weld made at 2 m/min (Figure 4-4c). The weld made at 4 m/min (Figure 4-4a) has only the initial indications of the surface oxide defect because the high travel speed would have had the least weld pool mixing.

The welds conducted at 3.0 m/min entrained a large quantity of the surface oxide while confining the defect to a small area. With a high concentration of incorporated oxide particles Figure 4-5 shows the effect of the surface oxide in the solidification microstructure. The incorporated oxide particles created locations for solidification micro-porosity to form. There was no evidence of solidification micro-porosity found in the remainder of the fusion zones of any of the welds.

The graph in Figure 4-6 shows the measured drop through of the welds. Two significant observations about this graph are that at 3.5 m/min, there was a significant decrease in overall drop through from 0.6 mm to 0.3 mm, and that no sample resulted in a weld with less than 10% drop through relative to the sheet thickness of 2 mm. A side effect of the low surface tension was a localized thinning out of the weld pool. This can be seen in the slow travel speed trials where material vaporization was exacerbated with prolonged exposure to the laser beam. The fastest travel speed welds showed little evidence of mixing or boiling with the oxide layer being essentially uninterrupted.

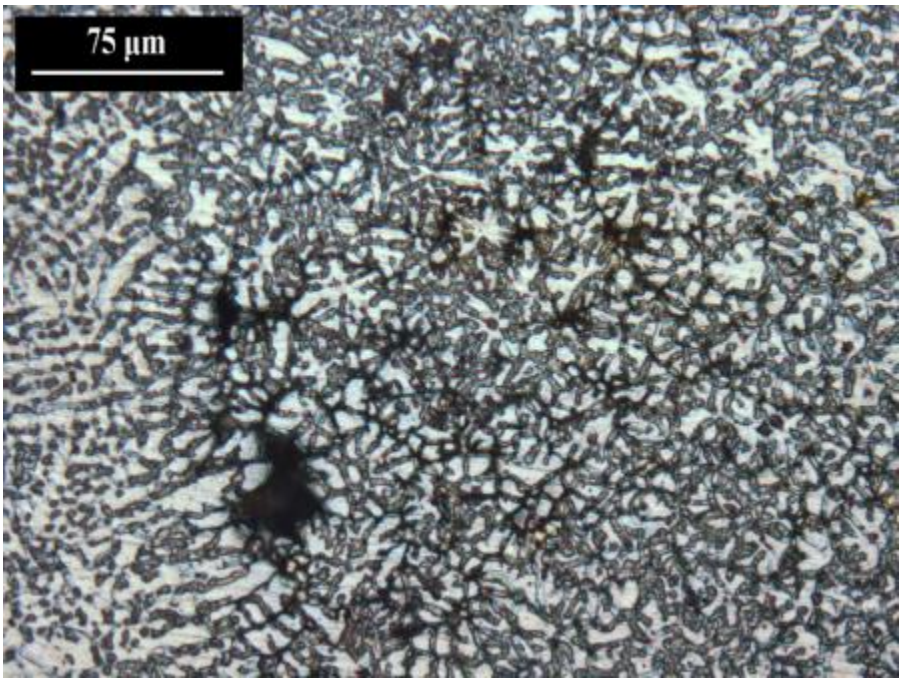

Figure 4-5: Dark region of a surface oxide defect in the diode laser weld made at 4 kW and 3.0 m/min shown in Figure 4-4b at A.

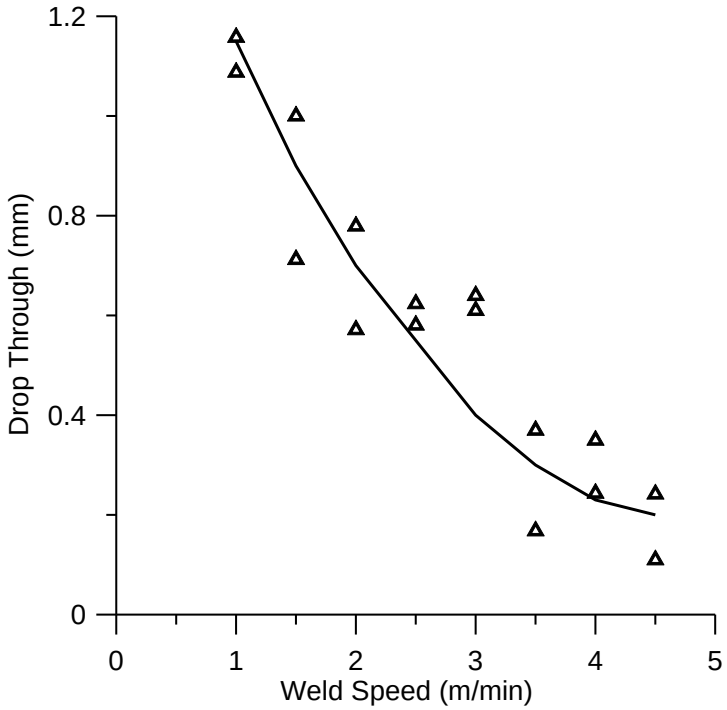

Figure 4-6: Drop through versus laser weld speed for bead-on-plate welds made using the diode laser at 4 kW.

While the original oxide layer was left intact, it provided excellent shielding for the molten pool during welding. When it was disturbed by mixing or boiling, the upper oxide layer was pulled into the weld pool or permitted exposure to the environment along the root surface.

The original base metal microstructure seen in Figure 3-1 had a relatively uniform equiaxed grain structure with little evidence of segregation or intermetallics beyond the presence of the manganese particles. The weld solidification structure was completely different. The fusion zones of all the sectioned welds were comprised entirely of dendritic solidification structures (see Figure 4-4 and Figure 4-5). Both columnar and equiaxed dendrites formed during solidification depending primarily on the welding travel speed and the location in the fusion zone. A representative columnar-dendritic solidification structure is shown in Figure 4-7. This microstructure was found only in the slow travel speed weld samples near the fusion boundary where solidification took place at a slower speed with a high thermal gradient. Figure 4-8 shows a representative equiaxed-dendritic solidification structure. This solidification microstructure occurred in all welds along the weld center-line and formed the majority of the weld microstructure in the higher travel speed weld trials.

Similar to aluminum, the relationship between the thermal gradient and the solidification rate controlled the occurrence of constitutional supercooling, which determined the resulting microstructure. Due to magnesium's very high thermal conductivity, the buildup of thermal energy was limited, which kept the thermal gradient low. When the welding speed was increased, the solidification rate similarly increased due to the reduced amount of time the weld segment was affected by the laser. Figure 4-9 depicts a relative correlation between the

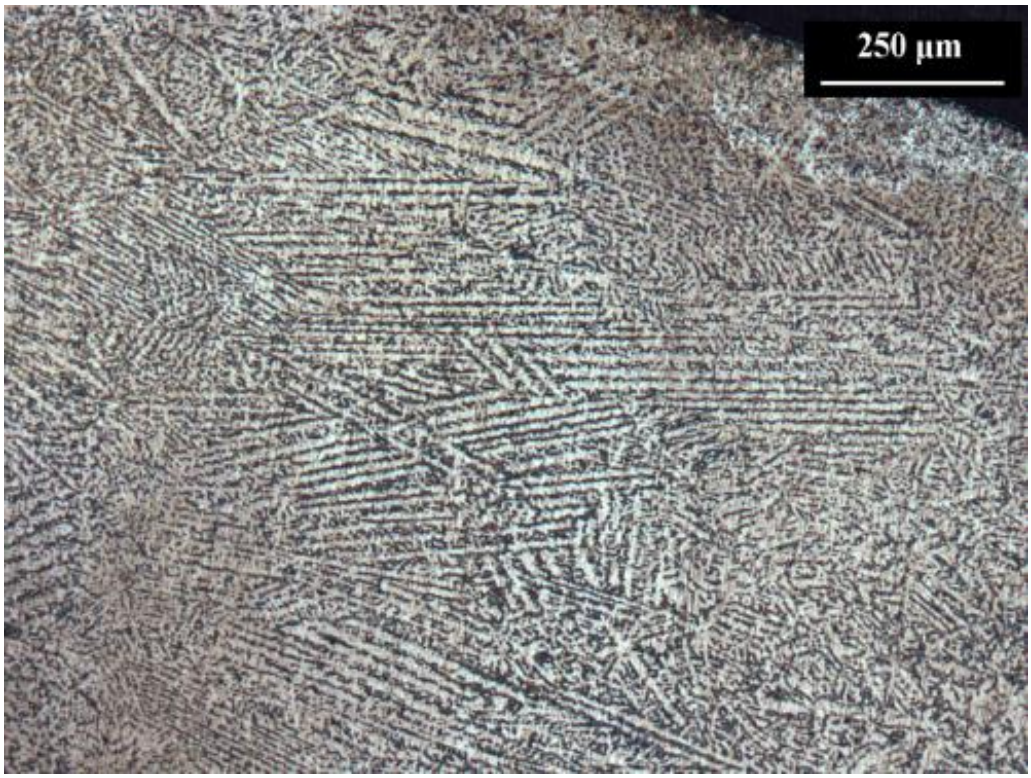

Figure 4-7: Representative columnar-dendritic solidification structure found near the fusion boundary of the diode laser welds where the solidification growth rate was low.

thermal gradient and rate of solidification and the expected solidification structure. This model proposed by Kou [10] predicted the observed columnar-to-equiaxed grain transition (CET) that occurred when the travel speed was increased and the solidification structure switched from a columnar to an equiaxed-dendritic structure. The CET is beneficial in preventing centerline solidification cracking, but requires a large quantity of heterogeneous nucleation sites, high growth rates, and low thermal gradients [10,48]. The fine equiaxed structure achieved in Figure 4-8 suggests the nucleation points were available, likely from the alloyed manganese particles, while the higher welding travel speeds both increased the solidification growth rates and decreased the surrounding thermal gradients to initiate the CET.

Figure 4-8: Representative equiaxed-dendritic solidification microstructure found in the center of the diode laser welds where the solidification growth rate was high.

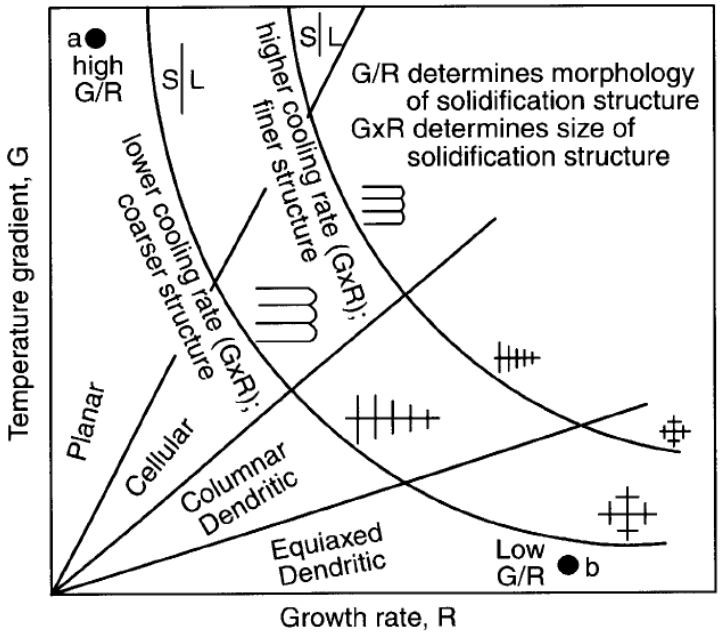

Figure 4-9: Solidification morphology prediction based on the temperature gradient and growth rate (taken from Kou [10]).

4.1.1.3 Tensile Test Results

Base metal tensile tests were performed in accordance with the ASTM standard full size rectangular tensile samples Section B557-06 [1] to provide a benchmark for evaluation of all subsequently tested weld samples. Figure 4-10 shows results of these tensile tests. Of the two sets of tensile test specimens used, one set was oriented transverse and the other parallel to the rolling direction. The samples tested in-line with the rolling direction proved to have superior mechanical properties with plastic yielding at 277 MPa and ultimately failing at 313 MPa after 9.9 mm cross-head displacement. Cross-head displacement was used instead of strain because no extensometer was used during tensile testing and it facilitates the future comparisons between these base metal tensile tests and subsequent non-homogeneous transverse welded tensile tests.

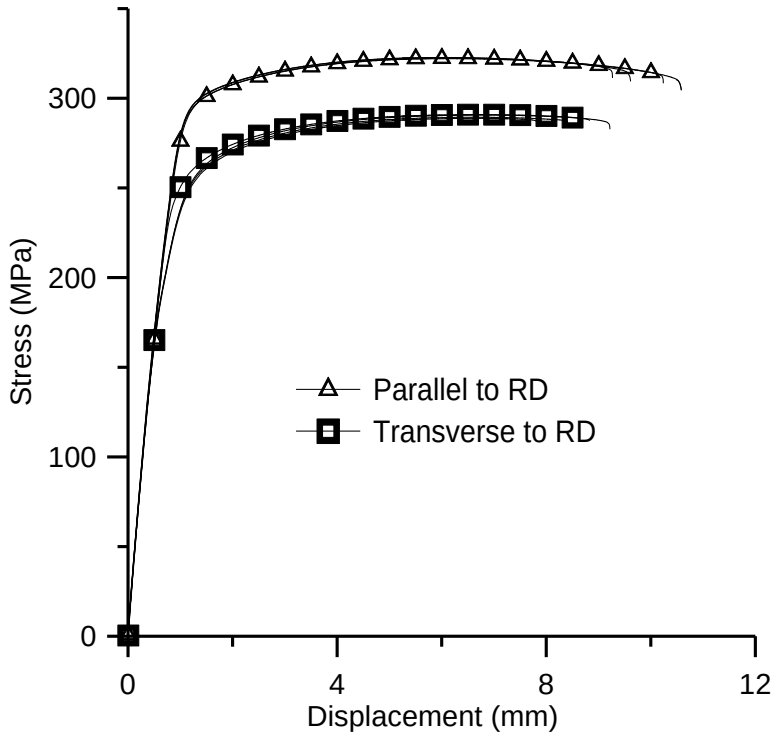

Figure 4-10: Measured stress versus cross-head displacement of AZ31B-H24 base metal tensile specimens.

The 4 kW diode weld conducted at a travel speed of 3.5 m/min was selected as the optimized weld from Experimental Series A due to its low drop through, low entrainment of surface oxide, uniform penetration, and high MR. This set of weld parameters were used to create tensile samples to investigate transverse tensile strength of the diode laser welds. Figure 4-11 shows the results of testing the samples to failure. All specimens failed in the weld metal and the scatter of the data is very large compared to the base metal samples with ultimate tensile strength ranging from below 120 MPa to over 180 MPa. The welded tensile results were plotted with the base material results in Figure 4-12 where the significant decrease in overall mechanical properties can be more readily seen. There was little or no evidence of plastic deformation, rather, the 1.2 mm displacement of the cross-head at failure is much less then that exhibited by the base metal. This indicates that strain localization around weld defects such as oxide inclusions or solidification micro-pores played a primary role in limiting the overall mechanical properties of the bead-on-plate diode laser welds. The solidification cracks and micro-pores associated with the entrained surface oxide would have caused severe strain localization, subsequently decreasing of the overall yield and ultimate tensile strength and elongation to failure of the samples.

All base metal tensile specimens fractured within the narrowed region of the tensile coupon with a 45° fracture surface. This varied from the diode laser welded specimens where all samples fractured at the weld centerline where the drop through was greatest. The fracture was always flat and perpendicular to the plane of the sheet.

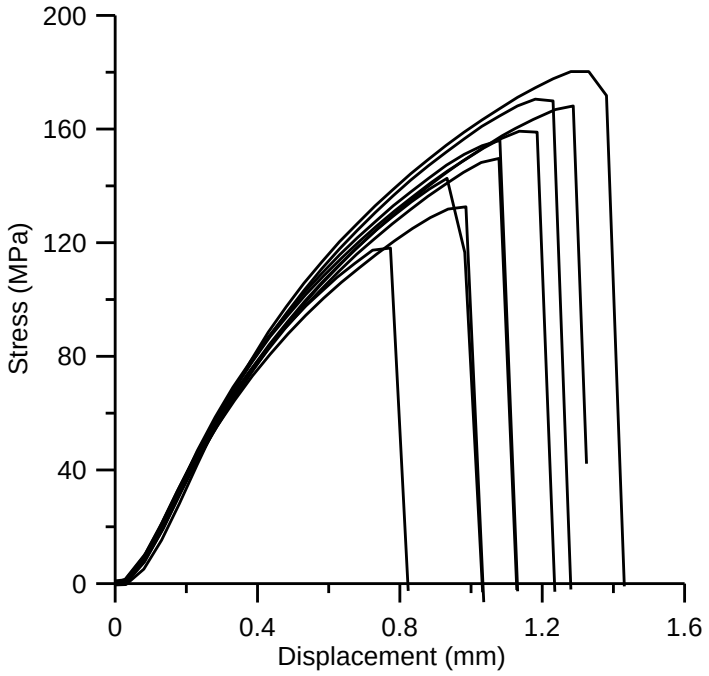

Figure 4-11: Measured stress versus cross-head displacement of the diode laser weld made at 4 kW and 3.5 m/min.

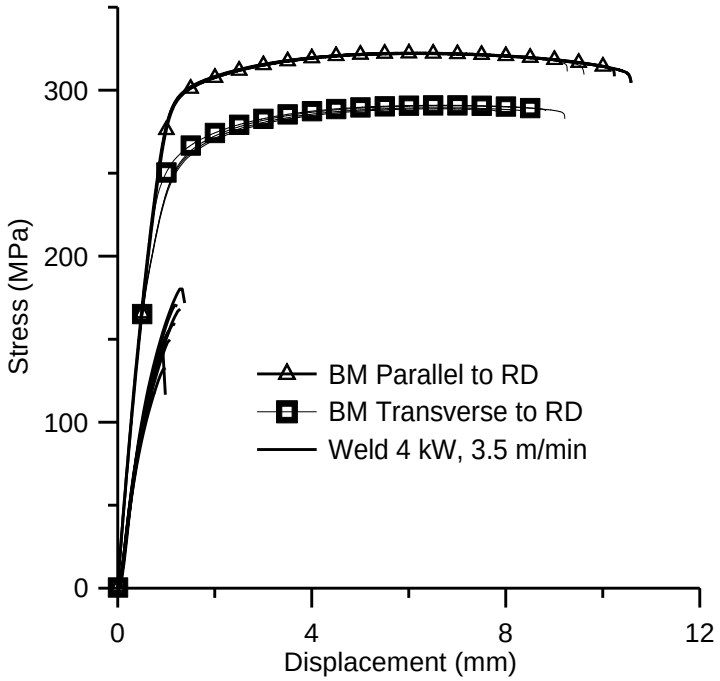

Figure 4-12: Diode laser weld transverse tensile test results comparison with base metal properties.

Fractography was conducted on the base material sample and showed a ductile fracture surface seen in Figure 4-13 with no distinguishable grains or grain boundaries. Figure 4-14 displays a representative fracture surface of the diode laser weld sample which experienced a much more brittle failure morphology. In the weld fracture surface, the dendrite solidification structure is discernable inferring that the failure progressed primarily along the solute rich interdendritic regions.

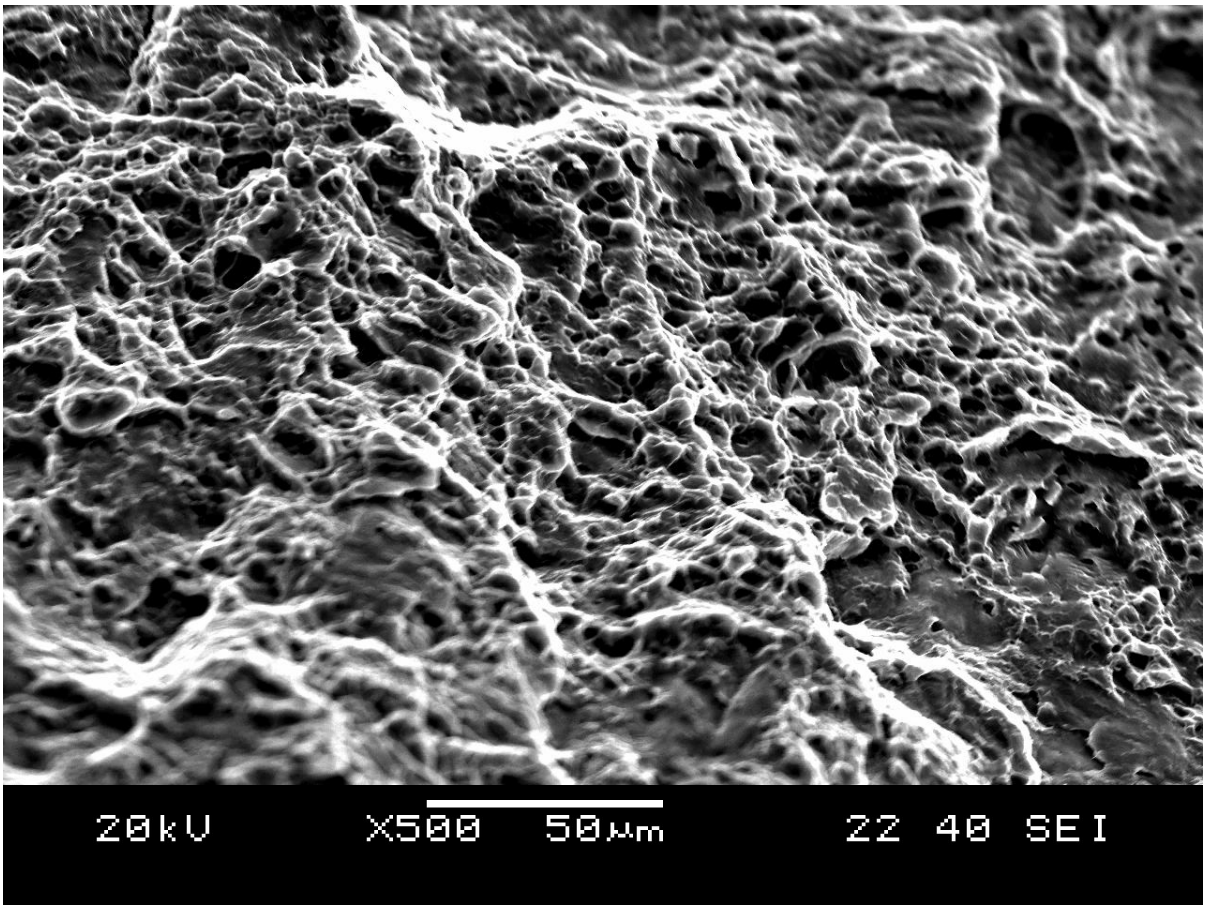

Figure 4-13: SEM image of the base metal ductile fracture surface.

The weld drop-through and change of fracture mechanism from ductile to brittle fracture were identified as the most significant issues limiting the tensile strength of the welded specimens. Since post-weld heat-treatments were beyond the scope of the current

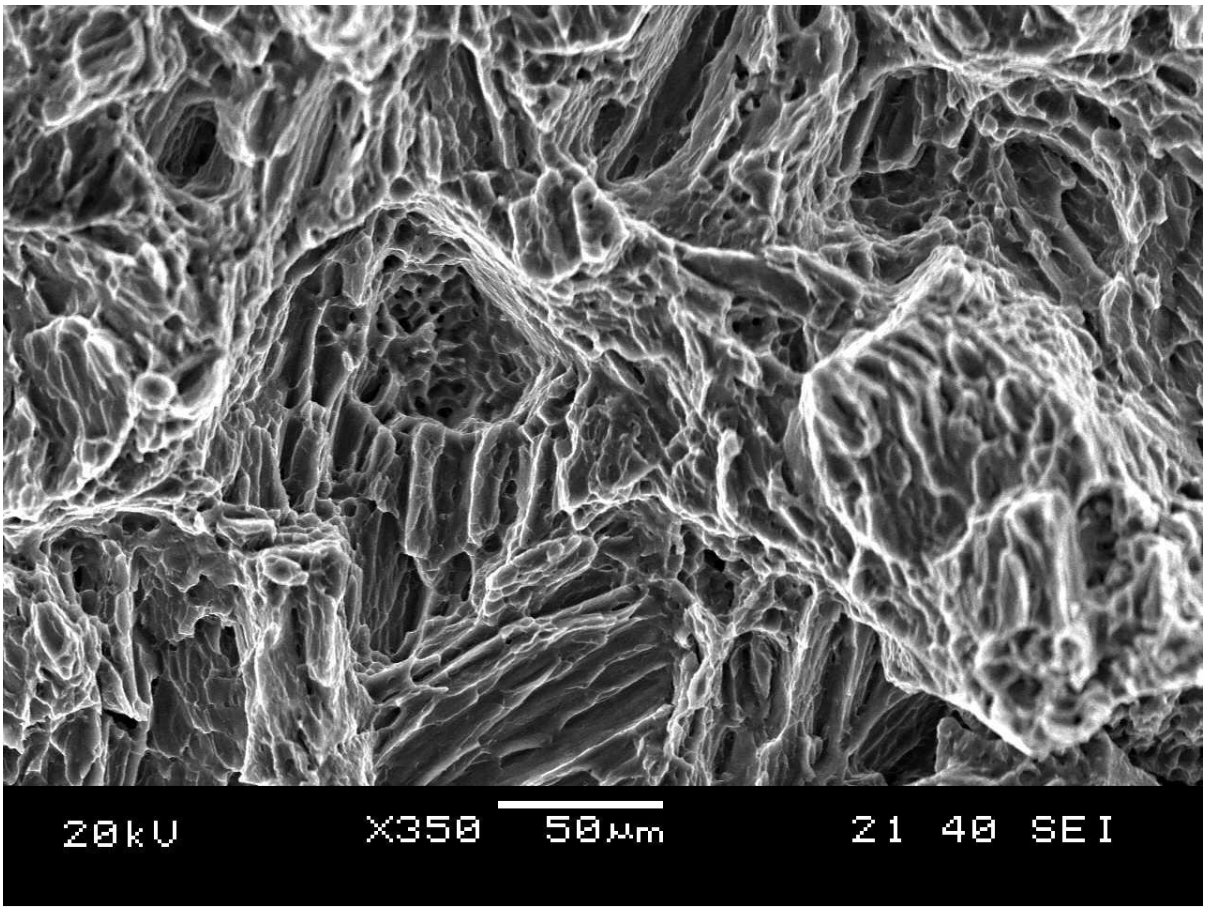

Figure 4-14: SEM image of the diode laser weld brittle fracture surface.

investigation, only dendritic solidification structures were achieved in the fusion zone. An equiaxed grain structure such as was observed in the base material was not possible to replicate during solidification of the weld pool. Kou [10] and Grong [49] have both investigated a similar process of dendritic solidification in aluminum alloys based on extensions of the Scheil equation. Both columnar and equiaxed dendritic structures incorporate alloy segregation along the inter-dendritic regions. In the AZ31B magnesium alloy, this can result in the creation of intermetallics such as $Mg_{17}Al_{12}$, although no evidence of any intermetallics was found in the diode laser welds. For complete columnar-dendritic structures, the possibility of macro-segregation is much greater than for equiaxed-dendritic

structures. This is because the columnar structures segregate the solutes preferentially towards the weld centerline. Leung [50, 51] and others [52], have investigated the negative effects that aluminum-magnesium intermetallics have on joint strength. Since having a solute-rich alloy increases the likelihood of intermetallic compounds forming where failure was identified to take place would be further detrimental to the overall material properties, the equiaxed solidification structure was determined to be preferential.

4.1.2 Experimental Series B

The trials conducted in Experimental Series A identified the range of travel speeds that were likely to produce sound diode laser weld specimens. Welds in Experimental Series B were conducted on specimens with sheared interfaces in a butt joint configuration. Dynamic modifications were made from the initially planned set of welding trials during experimentation. Trials were omitted where previous parameter combinations in Experimental Series B showed signs of incomplete weld penetration at high travel speeds or where signs of blowholes appeared at slow travel speeds. Conversely, welds were also added where the threshold to incomplete penetration or the appearance of blow holes had not been achieved through the planned experiments. This resulted in the identification of a bounded region for weld parameter combinations that would produce visually acceptable welds.

4.1.2.1 Weld Bead Surface Quality

Figure 4-15 shows the initial acceptability chart based upon visual inspection of the welds conducted for Experimental Series B. Outlined is the region where the created welds had consistent and repeatable surface profiles. Select welds were attempted at 1 kW but produced only partially penetrated samples down to the slowest tested travel speeds of

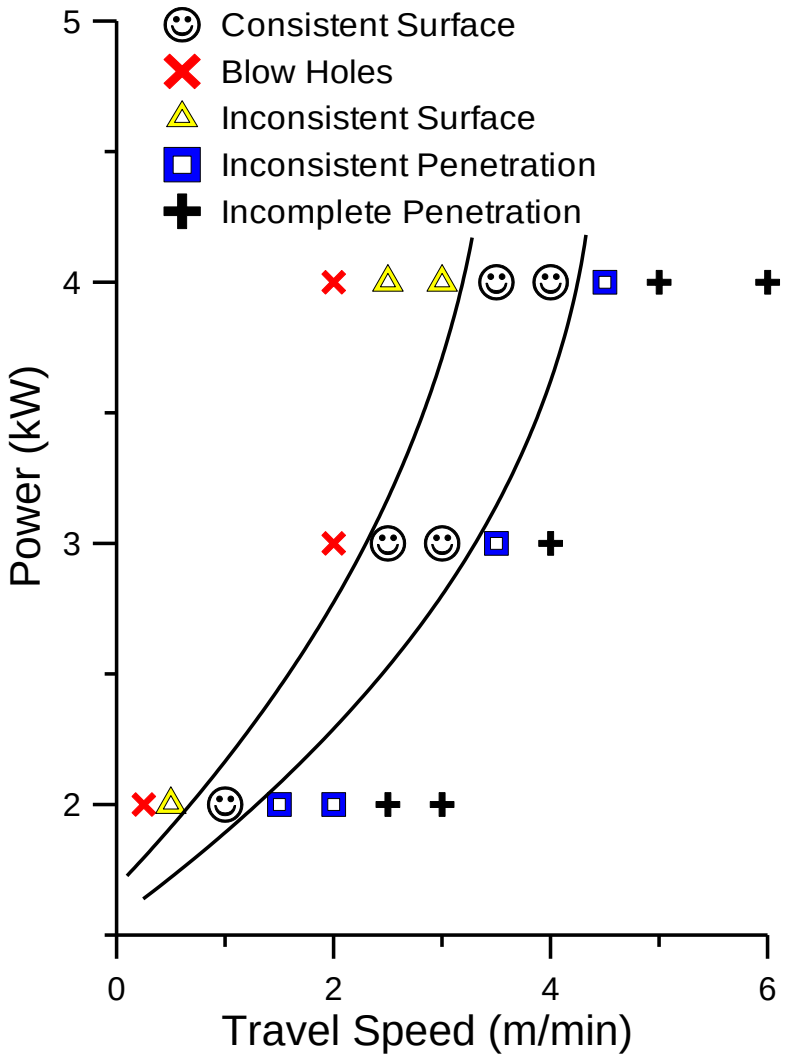

Figure 4-15: Experimental Series B diode laser welding acceptability chart.

0.25 m/min. The 1 kW data points were omitted from the acceptability chart, but would conform to the plotted data which predicts only inconsistent and partial penetration welds are possible below the 1.5 kW power level.

Photographs of two of the consistent weld samples completed in Experimental Series B are shown in Figure 4-16. These welds were devoid of surface solidification cracks or porosity. Many of the samples exhibited a visible seam along the root side of the weld. This defect was investigated and found to be superficial; disappearing if scratched and was

determined to be a residual effect of the original oxide layer. When welded, the freshly sheared edge was oxide free, while the top and bottom surfaces still retained the original oxide up to the joint edge. The laser welds exhibited under-fill and drop-through of the weld pool which resulted in an elongation of the root surface which the oxide was not able to accommodate. This additional distance produced a thin region along the center of many of the consistent welds where unoxidized magnesium was left exposed. For many of the weld trials to the left of the bounded area in Figure 4-15, coupling was a significant problem, because the edges of the specimens would melt and surface tension acted to pull back the melt on each edge. This opened a gap for the laser beam to pass through the sample, drastically reducing the laser beam absorption. Figure 4-16c shows an example of this, where the sheet exhibited through-thickness melting of the edges of the specimens without coupling for the vast majority of the weld. The finished weld was essentially two separate sheets with the previous shear interface having been melted, showing signs of sagging due to gravity. In the slow travel speed welds, this feature was more pronounced, resulting in the weld samples melting back much more drastically during welding producing very wide gaps. In the slow travel speed welds to the left of the bounded region where coupling was achieved, the large width of the weld fusion zone combined with the force from the shielding gas overcame the surface tension and produced blow holes along the length of the weld.

The difficulty with producing a consistent high strength weld was attributed to the poor joint fit-up associated with the shear surfaces. The large gaps inhibited joint coupling and promoted the occurrence of melt pull-back and incomplete fusion.

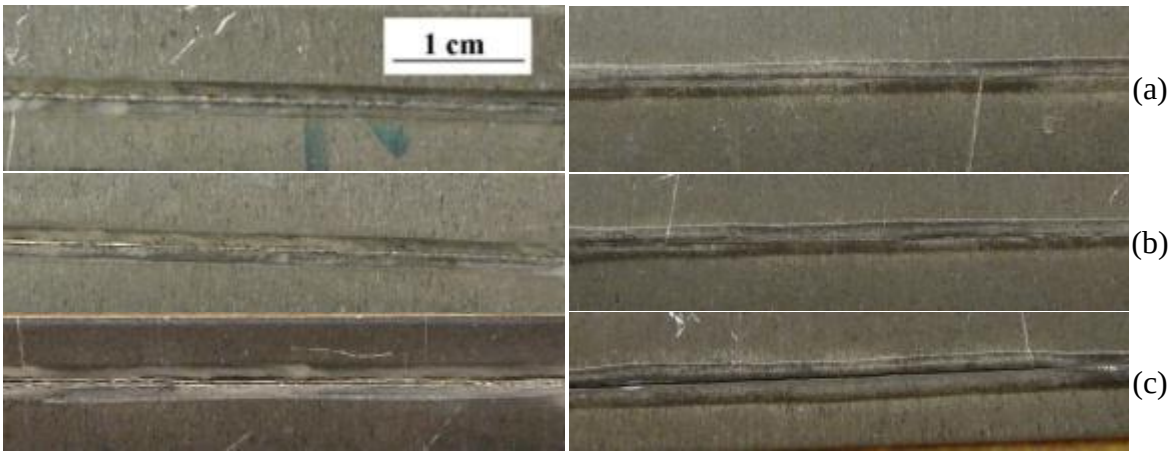

Figure 4-16: Diode laser weld top and bottom surfaces made at: a) 4 kW and 4 m/min, b) 3 kW and 3 m/min, and c) 2 kW and 2 m/min.

4.1.2.2 Weld Cross Section Analysis

Due to the significant amount of weld defects found with only visual inspection of the samples, the majority of the metallurgical analysis was omitted. Since most of the weld parameters were not even able to produce a coherent weld, sections were only taken to corroborate what was hypothesized previously. Figure 4-17 shows an example of an included oxide layer. This was a commonly occurring defect in many of the samples and would limit the overall strength of the weld when tested in tension.

These identified defects were primarily attributed to a lack of sheet coupling which produced significant root seams and centerline solidification cracking. These seams appeared to be exacerbated by the surface oxide being pulled into the joint interface when coupling was not initially achieved. The material would melt back, pulling the surface oxide into the joint, and then achieve coupling while the oxide remains in the interface thereby inhibiting the formation of a homogeneous weld. Solidification cracking was identified most commonly at higher weld travel speeds where the solidification was complete before enough

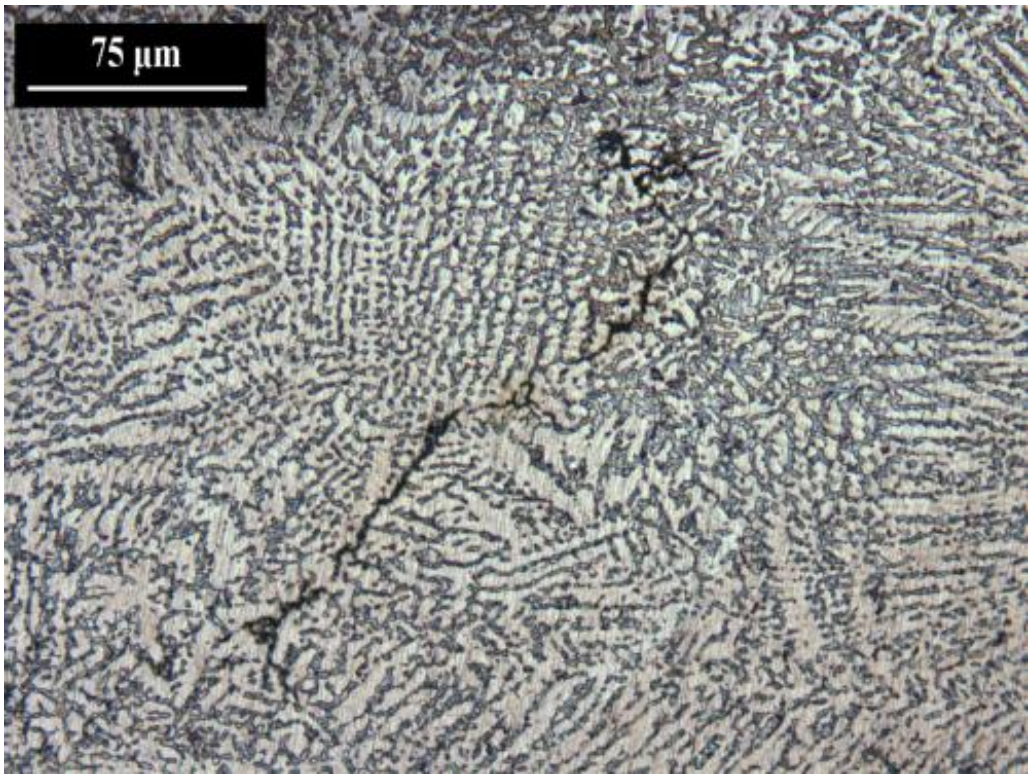

Figure 4-17: Oxide inclusion in a 4 kW, 1.5 m/min diode laser weld.

of the weld heat was dissipated. This led to high stresses in the weld as the material contracted, pulling on the newly solidified metal producing centerline cracking in the fusion zone. The presence of oxides in the fusion zone intensified the solidification cracking but the defect was present even when no oxide contamination was observed. The cracking was minimized by the use of a narrow distance between the clamps but was still unavoidable at higher travel speed weld trials.

Samples were still found to be primarily gas pore free with only small infrequent pores such as the one imaged in Figure 4-18. These were likely from gas pockets that were trapped in the shear surface interface or a result of absorbed hydrogen from incorporated hydrated oxide segments. Figure 4-19 shows an example of a centerline solidification crack. It can be seen to progress along the dendrite grain boundaries and is representative of crack initiation

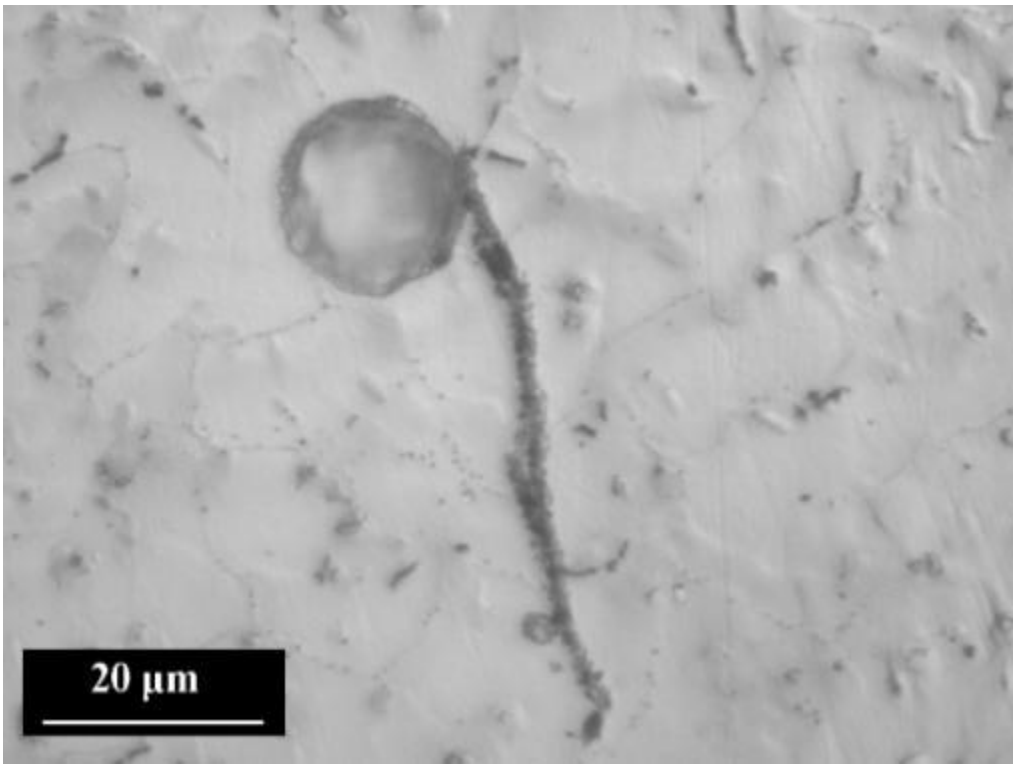

Figure 4-18: Gas pore and oxide stringer.

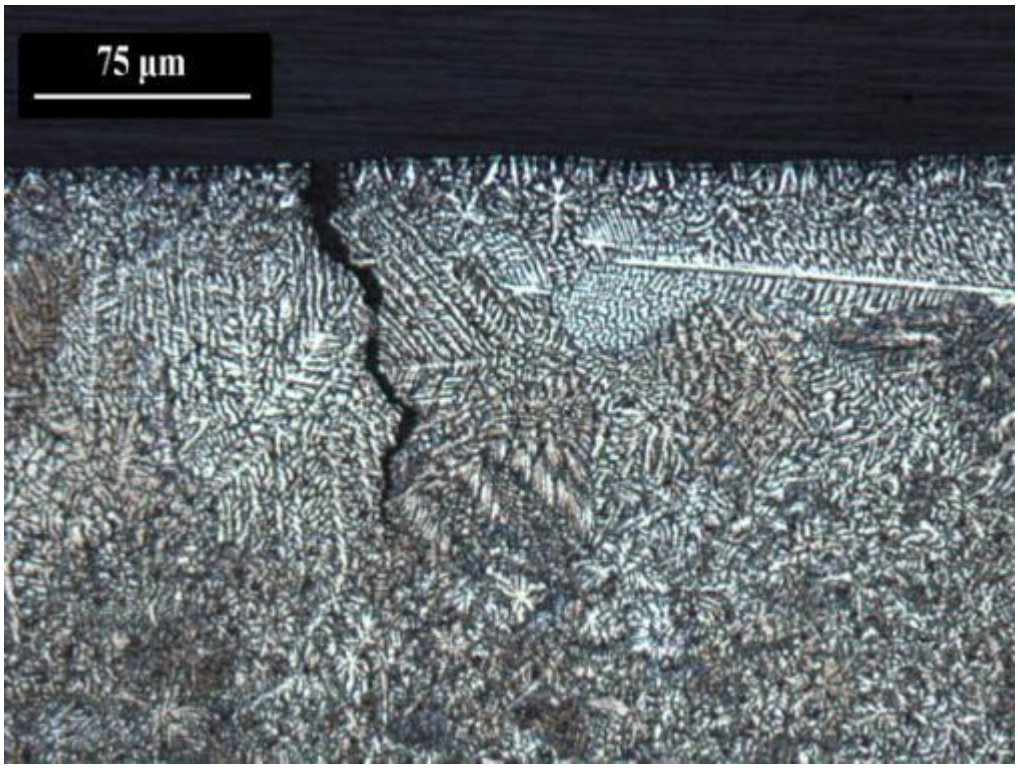

Figure 4-19: Solidification crack at a diode laser weld center line.

caused by the thermal contraction of the weld during solidification. With the high frequency of centerline solidification cracking and brittle oxide layer inclusions in the majority of the welds from Experimental Series B, there were no welds that were deemed to be suitable or worthwhile for further analysis or tensile testing

4.1.3 Experimental Series C

The same parameters used in Experimental Series B were used in Experimental Series C; however, the weld specimens had fully cleaned, machined joint interfaces that were stainless steel wire brushed to mechanically remove the pre-existing grey surface oxide layer prior to welding. With the removal of the original surface oxide layer, it was discovered that the laser was not able to produce a weld of any significant penetration. No welds were produced using any of the parameters in Experimental Series B. This series of trials showed the other major benefit of having the oxide layer present on the material during welding; the relative absorptivity of the oxide layer is substantially higher than the cleaned and wire brushed base material. The oxide layer was removed to avoid its incorporation into the weld pool but this then requires that the parameters be optimized again to account for the low absorptivity associated with the oxide-free base metal.

4.1.4 Experimental Series D

Experimental Series D was performed to examine the weldability of the magnesium samples with excellent joint fit-up and full surface cleaning. The samples offered the highest quality joint preparations possible while still being feasible in real world production.

4.1.4.1 Weld Bead Surface Quality

With Experimental Series C showing the significant reduction in laser beam absorption compared to series B, it was reasoned that to complete a full penetration diode laser weld on a fully cleaned sample, the welding speed would have to be reduced dramatically. Figure 4-20 shows the acceptability chart for the welds created in Experimental Series D. The weld samples were grouped visually into one of three categories; consistent weld profile, inconsistent weld profile and solidification crack. Inconsistent weld profile was used to describe the welds that could not maintain a stable weld pool. This was generally due to the fact that the laser could not achieve the minimum initial heating required to melt the magnesium alloy. In several of these samples, there would be short regions of melting, often not enough to fully penetrate the sample. The high thermal conductivity of the magnesium would dissipate any built up heat prior to the formation of a full penetration weld pool.

Solidification cracks were extremely prevalent in all welds conducted at 2 kW power level and those in the transition zone between the consistent welds and the partial penetration welds. With the welds conducted in series D, there were likely no oxides to exacerbate the solidification cracking problem and so these trials illustrate the true hazard that solidification cracking poses with magnesium welding. In this region, the weld pool was solidifying quicker than the surrounding material could dissipate the accumulated thermal energy. This caused the majority of the thermal shrinking forces to be subjected upon the fusion zone.

The region where consistent weld profiles occurred was at the high weld power levels with very slow travel speeds. At the high power settings, the laser had sufficient energy to overcome the reflective qualities of the cleaned magnesium sheet and produce a stable weld

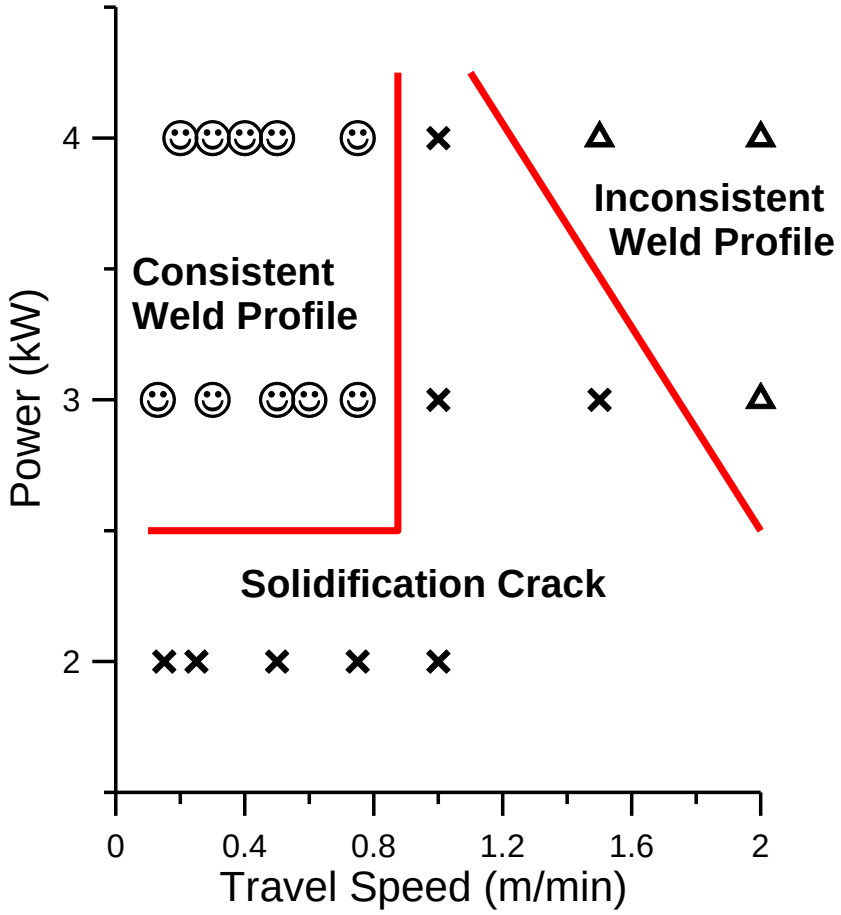

Figure 4-20: Experimental Series D diode laser welding acceptability chart.

pool while traveling slow enough to allow the weld pool to settle before the solidification process was complete.

From these completed weld samples, three sets of parameters were selected for further analysis; 3 kW and 0.5 m/min, 3 kW and 0.75 m/min, and 4 kW and 0.75 m/min. The fastest consistent weld profile travel speeds were chosen because these samples had the smallest overall material losses. A slower speed sample was also used for comparison purposes.

4.1.4.2 Weld Cross Section Analysis

Several transverse sections were taken from selected welds in the consistent weld profile grouping. Figure 4-21a shows the weld conducted at 3 kW and 0.50 m/min and Figure 4-21b

shows the 4 kW, 0.75 m/min laser weld. Similar to previous diode laser weld samples investigated, these welds had a very low frequency of gas pores. With the removal of the surface oxide, the two remaining defects were the weld drop-through and clamping induced cold cracking such as that shown in Figure 4-22.

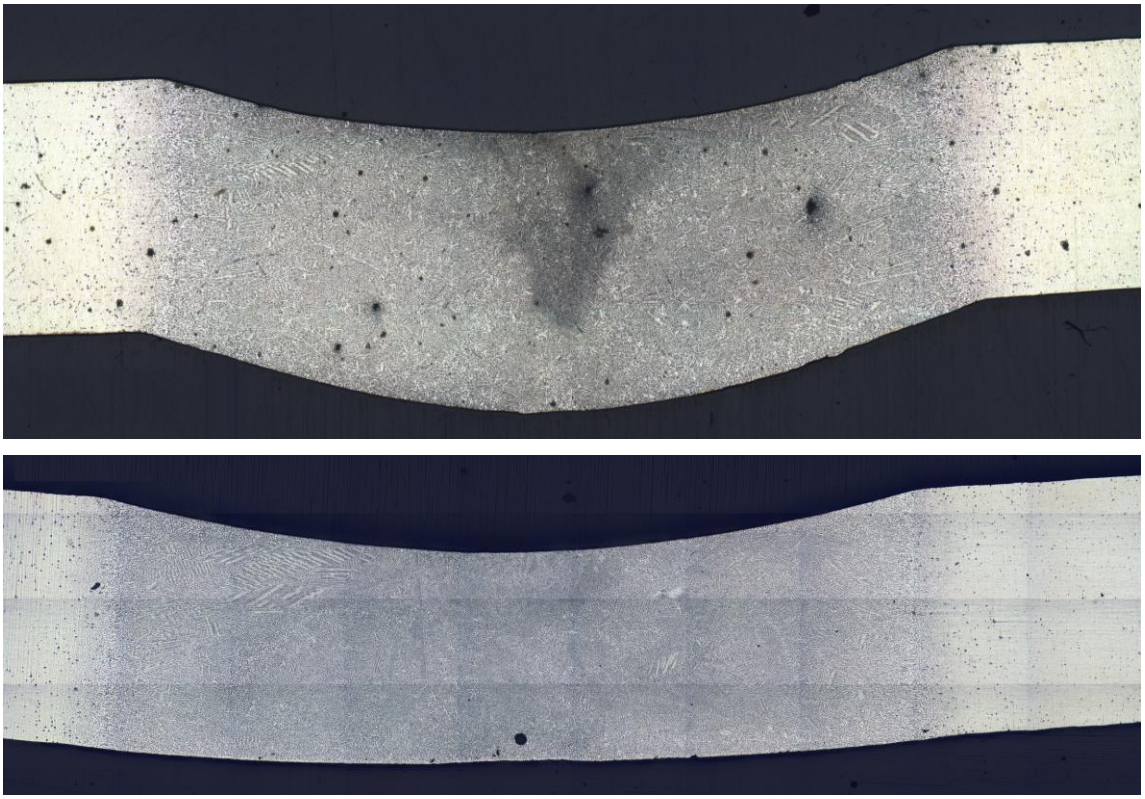

(a)

(b)

Figure 4-21: Diode laser weld transverse section made at: a) 3 kW and 0.50 m/min, and b) 4 kW and 0.75 m/min on 2 mm thick sheet.

The cold cracking was not as prevalent as the solidification cracking was in Experimental Series B. Instances of crack formations were still found when the welding parameters resulted in a weld pool where the surrounding material was not uniformly heated, the high thermal contractions after welding would exceed the weld strength and cause cracking. Figure 4-22 shows a crack initiating at the root of the weld extending along the centerline of the weld. With the 3 kW and 0.50 m/min weld, the thermal forces were not

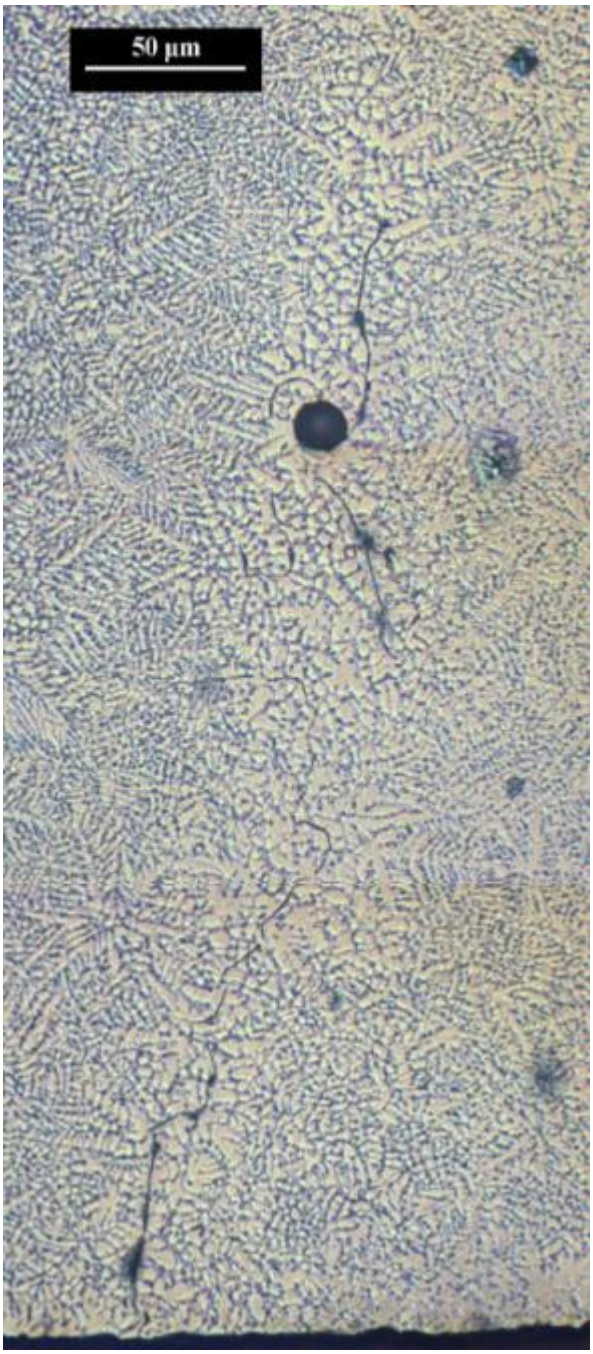

Figure 4-22: Cold Crack originating from the root surface in a 3 kW and 0.50 m/min diode laser weld.

sufficient to propagate the crack fully through the thickness, but this shows it was a significant problem and that visual inspection alone could not identify a sound weld. Had the sample been tested with liquid penetrant, this crack would have been identified non-

destructively, but only because it originated at the surface which is not necessarily true of all the solidification cracks experienced during diode laser welding. The other samples sectioned did not show signs of solidification cracking or porosity.

The weld drop-through, melting ratios, and MBMA values are listed in Table 4-1 for the three analyzed welds. For all three samples, the drop through, MBMA, and MR are very similar showing very little variation with changing input power or weld travel speed. The one major difference occurred when the power was increased to 4 kW and the root side of the weld experienced very little sagging. This phenomenon was observed in other samples as well and was generally experienced by weld pools where a large amount of material was lost due to boiling. Figure 4-23 shows a sample welded at 3 kW and 0.13 m/min where the fusion zone was significantly reduced due to material loss and the root of the weld was almost completely flat and co-planar with the bottom sheet surface. This effect was a result of the reduced weld pool, with the high amount of vaporization reducing the volume of the weld pool, the surface tension of the magnesium and the increased backpressure created by the high rate of vaporization was able to maintain a planer lower surface.

Table 4-1: Experimental Series D weld profile analysis.

Power kW	Travel Speed m/min	Sag µm	Drop Through µm	MBMA mm²	WMA mm²	Melt Ratio
3.0	0.50	665	547	12.9	13.4	6.7
3.0	0.75	658	454	12.6	12.8	9.7
4.0	0.75	174	493	13.6	12.2	7.9

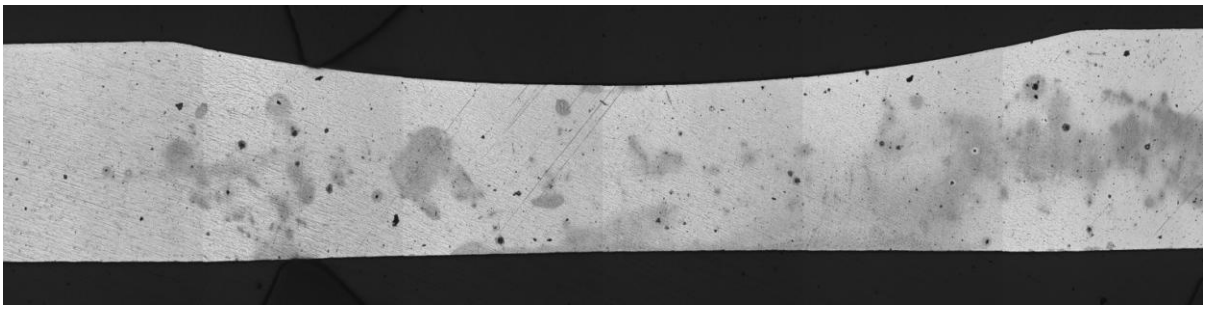

Figure 4-23: Diode laser weld transverse section made at 3 kW and 0.13 m/min on 2 mm thick sheet.

4.1.4.3 Hardness and Tensile Test Measurements

The 0.50 and 0.75 m/min 3 kW diode laser welds conducted on 2 mm thick sheet, were tensile tested and compared against each other in Figure 4-24. The presence of the solidification crack in the 0.5 m/min sample explains the lower ultimate strength experienced at failure of 156 MPa. This was approximately the same strength as the bead-on-plate samples achieved from Experimental Series A. The 0.75 m/min samples had an average ultimate strength of 184 MPa which was the highest failure strength measured from welds made using the diode laser system. The other important observation was that the line of fracture in the tensile samples transitioned back to a 45° ductile surface. Figure 4-25 shows a representative fracture surface of each tensile specimen. The 0.50 m/min travel speed samples all experienced fracture on a perpendicular plane along the centerline of the weld. This is characteristic of brittle or fast fracture through a low fracture toughness material with pre-existing flaws such as that shown in Figure 4-22. Figure 4-26a shows the fracture surface where the extent of the solidification crack can be seen as the smoother dark grey region. Conversely, the 0.75 m/min tensile samples fracture, seen in Figure 4-26b, progressed in a more ductile fashion similar to the base metal samples, following a 45° path originating from the top center of the fusion zone.

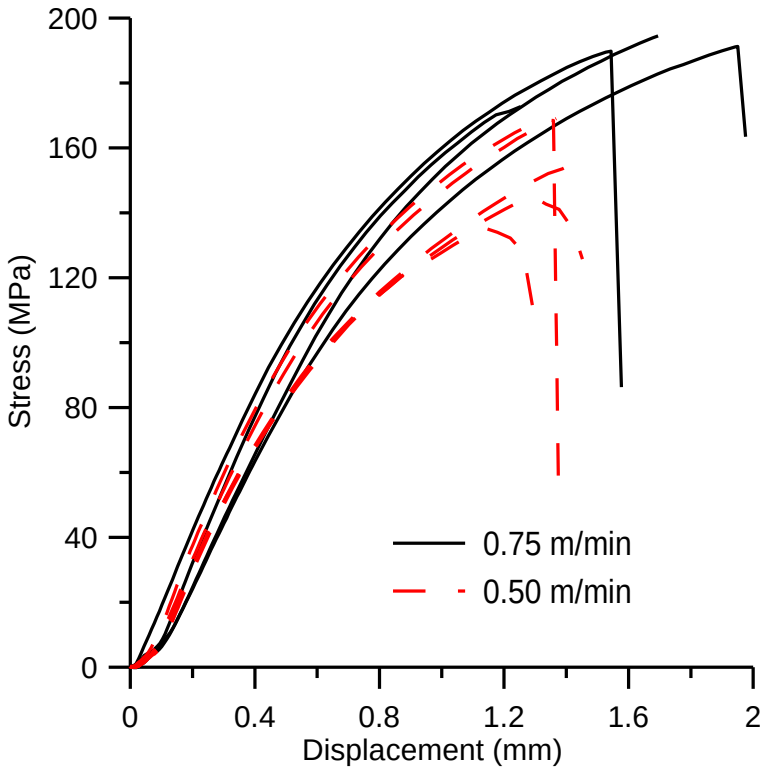

Figure 4-24: Measured stress versus cross-head displacement of the diode laser welds made at 3 kW and 0.75 m/min and 3 kW and 0.5 m/min.

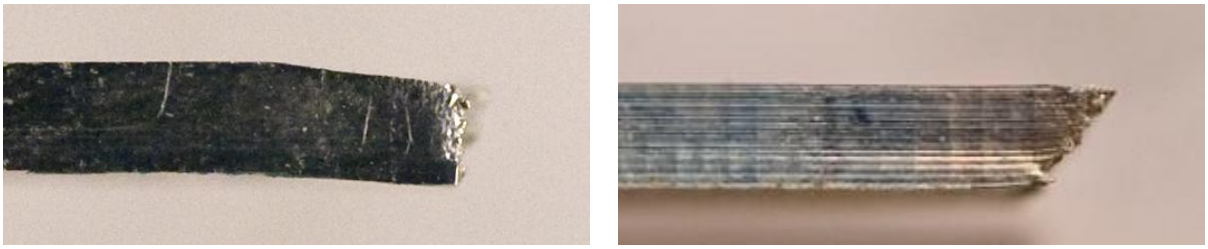

(a) (b)

Figure 4-25: 3 kW diode laser weld tensile fracture half sample profiles exhibiting: a) brittle fracture mode at 0.5 m/min and b) ductile fracture mode at 0.75 m/min.

The hardness profiles shown in Figure 4-27 are the individual hardness line profiles taken towards the top, mid-plane, and bottom of the weld. Figure 4-28 shows all three line profiles combined as an amalgamated plot. The hardness data was collected from the centerline of the weld and moves outwards into the base material. The scatter on the data collected from the three individual line hardness profiles shown in Figure 4-27 was

(a)

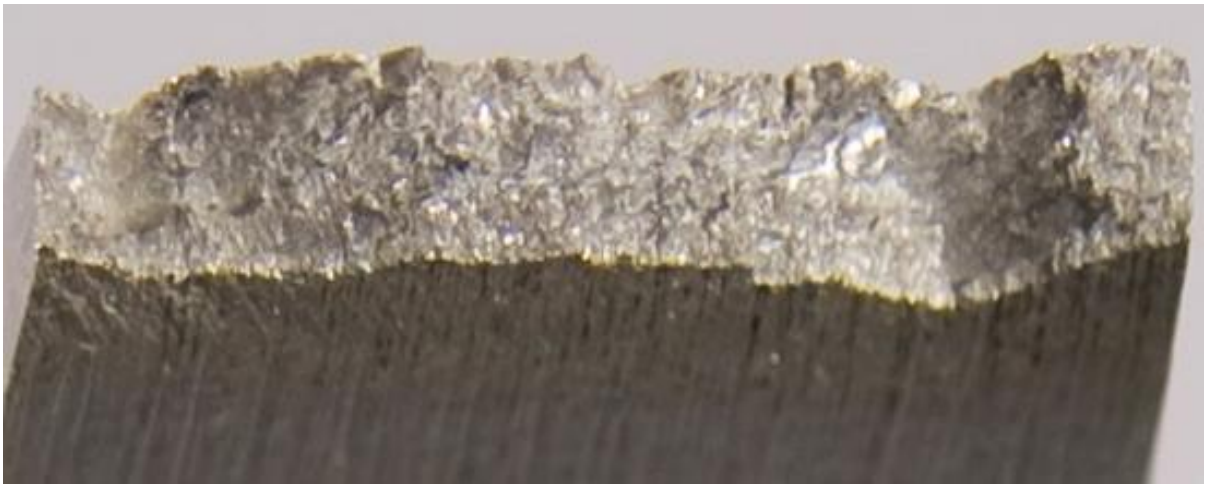

(b)

Figure 4-26: 3 kW diode laser weld tensile fracture half sample surfaces exhibiting: a) brittle fracture mode at 0.5 m/min and b) ductile fracture mode at 0.75 m/min.

consistent for all tested samples. The high sample density ensured a clear perspective was achieved of what had happened in the material. The profile shown is similar for all of the welds in that the fully annealed, as-solidified metal in the weld fusion zone was always the softest region, slightly below 60 VHN_{25} and around 6 mm wide, and the hardness of the material in the heat affected zone transitions evenly from the fusion zone hardness to the base metal hardness of 77 VHN_{25}. The softening shown in the fusion zone and heat affected zone was an unavoidable consequence of welding a base material that was strain hardened and partially annealed. When the laser melted the material, any residual strain hardening was eliminated leaving the fusion zone in an F temper state. The surrounding heat affected zone experienced additional annealing and recrystallization, reducing the alloy from a H24 state

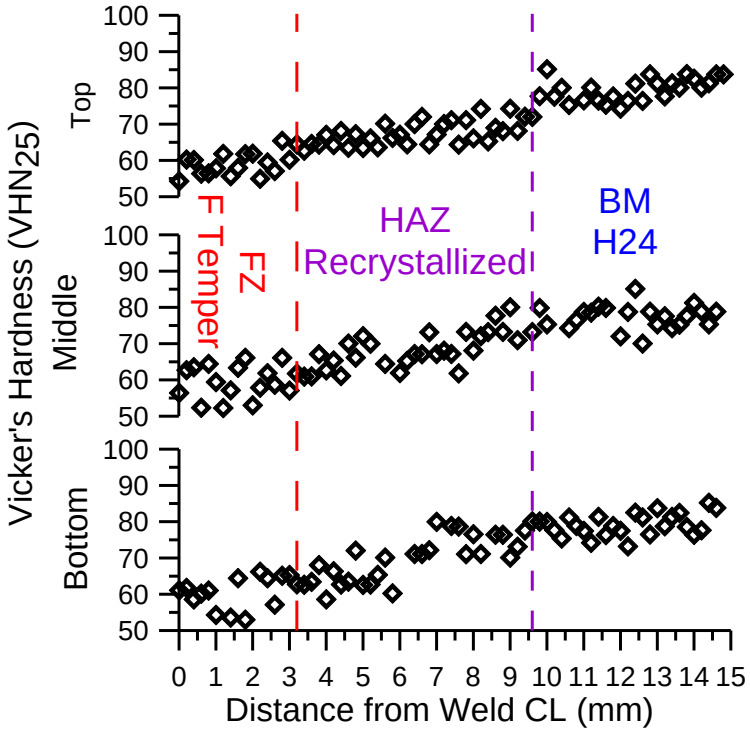

Figure 4-27: 3 kW and 0.50 m/min diode laser weld Vickers hardness profiles collected from the top, middle, and bottom of the sheet thickness.

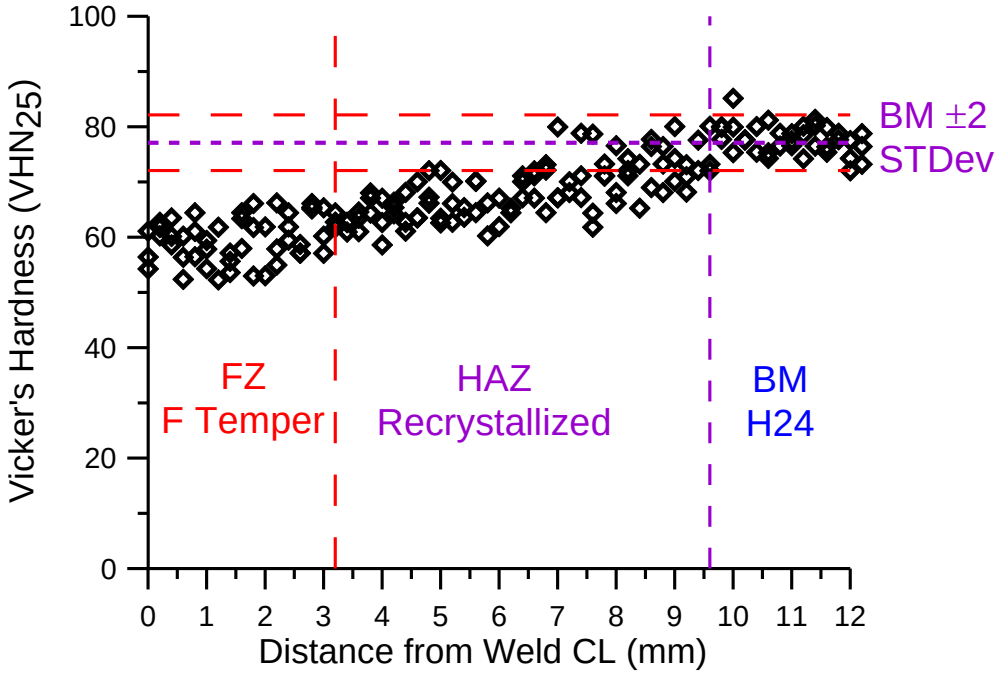

Figure 4-28: Amalgamated Vickers hardness profile of the diode laser weld made at 3 kW and 0.50 m/min.

toward an H20 or O temper with increasing proximity to the fusion zone. The only difference from weld to weld was the width of the fusion zone as it was discovered that the clamping arrangement did have a thermal dampening effect on the welds heat affected zone. This was determined since the base metal hardness was achieved at the same distance from the weld center line for all samples despite alterations in the welding parameters, approximately where the clamps were in contact with the welding samples. Since the fusion zone was the location of all tensile failures and the softest region, the impact the clamps had on the overall weld strength was determined to be negligible.

Figure 4-29 shows the tensile results for the two high speed welding conditions. The 3 kW sample was previously reported in Figure 4-24, but is shown again to provide a point of reference. The 4 kW weld samples failed with an ultimate strength of 168 MPa ± 8 MPa and fell between the previous two tested 3 kW welds. The fracture surface in the 4 kW samples was similar to previous welds, occurring at the weld centerline. All samples from the 4 kW weld trial experienced failure with a square fracture surface such as shown in Figure 4-25a. No evidence of solidification cracking or serious porosity was found in the 4 kW joints. The premature joint failure was attributed to the bulk material loss and sagging of the fusion zone, which was unavoidable when operating at slow travel speeds and maximum power.

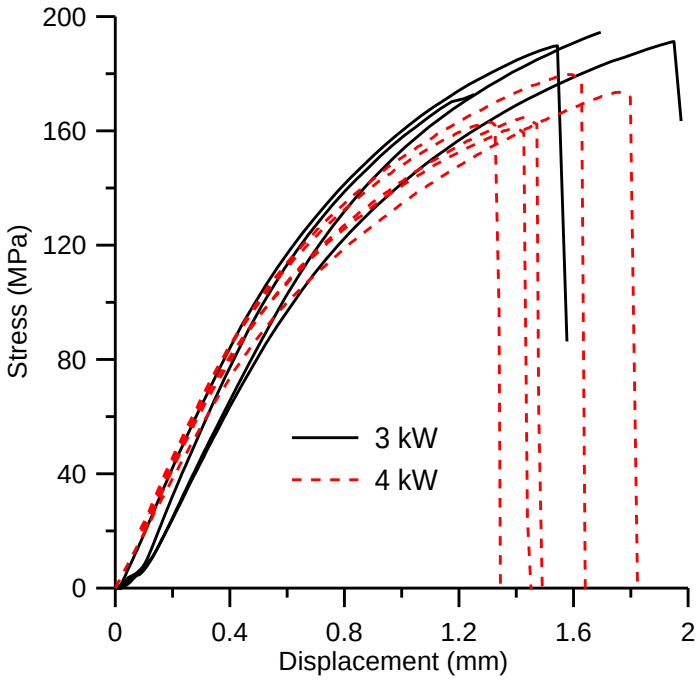

Figure 4-29: Measured stress versus cross-head displacement of the diode laser welds made at 4 kW and 0.75 m/min and 3 kW and 0.75 m/min.

4.1.5 Diode Laser Weld Tensile Test Comparison

The results of all four sets of tensile tests are shown in Figure 4-30 normalized as a percentage of the respective base material values in the rolling direction. The as-received test was from Experimental Series A and the remaining three test results were from Experimental Series D. The bead-on-plate weld tensile results were comparable to the 3 kW, 0.50 m/min test results. They both suffered from pre-existing cracks in the fusion zone, oxide inclusions for the former and solidification cracks for the latter. The other welds made at 0.75 m/min in the cleaned condition provided stronger joints with the 3 kW series proving to be the optimized conditions achieved using the diode laser welding process. As Figure 4-30 shows, the yield strength of all welds were only 40-50% of the base metal yield strength and the ultimate strengths of all the diode laser welds ranged from 50-60% of those

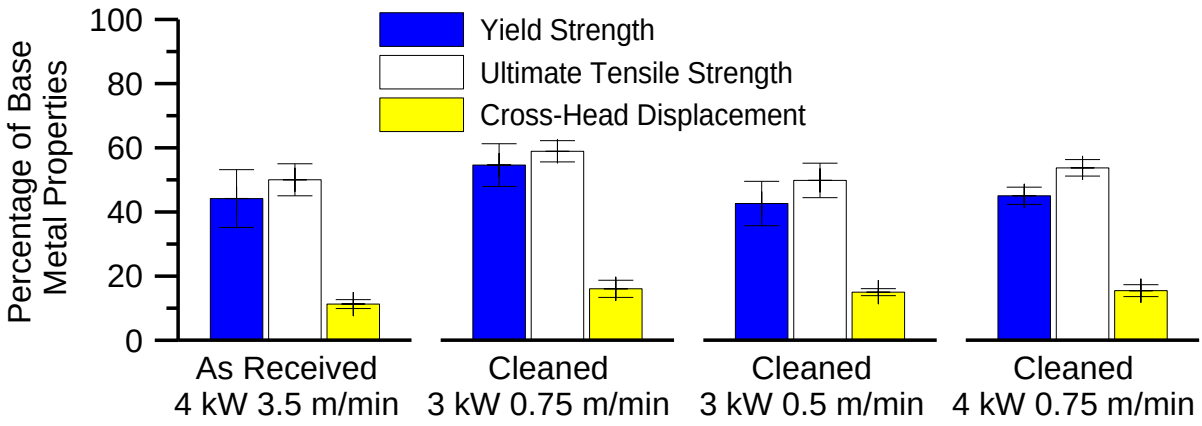

Figure 4-30: Diode laser tensile trials comparison as a percentage of the base metal properties in the rolling direction.

achieved in the base metal. All samples failed in the weld metal at a cross head displacement of only 10% of the base metal's properties. Material hardness is often used as an indicator for the material ultimate tensile properties. The fusion zone material was approximately 20% softer than the base material but testing showed it to be almost 50% weaker. This suggests that the weld defects such as cracks, pores, oxides, or other embrittling phases had caused additional strain localization which further limited the material's ductility and disproportionately decreased the yield and ultimate failure strengths of the welds.

The diode laser welding process was limited to conduction-mode welding because of its low overall laser power density, and as such, produced a characteristic weld profile that was relatively free of gas porosity but prone to both weld drop-through and solidification cracking. In summary, visually acceptable conduction-mode laser seam welds could be made in AZ31B 2 mm thick sheets with the diode laser welding process and a very limited range of process parameters provided the joint was machined, all surface oxides were removed by stainless steel wire brushing prior to welding, and that the top and bottom weld bead surfaces were shielded from the atmosphere during welding using helium shielding gas. In all cases,

the yield and ultimate transverse tensile strengths of the diode laser welds were less than 60% of the base metal properties and the displacements to failure were less than 10% of the base metal. There was little evidence of plastic deformation prior to failure. This was generally attributed to the strain localization around the weld defects such as oxide inclusions, solidification micro-porosity, or hydrogen pores.

4.2 CO_2 Laser Welding Results and Discussion

All CO_2 laser welding was performed using 5 kW laser beam power shielded with helium along both the top and root surfaces of all welds. All samples were prepared with milled edges and cleaned with acetone and ethanol. With the higher laser energy and tighter focal point, the CO_2 laser had over 1000 times the laser power density of the diode laser and was able to perform welding in keyhole mode. This produced welds with a much higher penetration-to-width ratio than the conduction-mode welds produced using the diode laser. The travel speeds investigated were 8 through 15 m/min, and were much higher than those of the diode laser trials.

4.2.1 Weld Bead Surface Quality

The 8 m/min weld shown in Figure 4-31 and the 12 m/min weld shown in Figure 4-32 are very similar despite the difference in welding travel speed. Both welds exhibit evidence of undercutting, weld spatter, and irregular, overlapping folds of weld metal. These weld defects are detrimental to the overall strength of the welds and result in an overall poor weld bead quality. Figure 4-33 shows the sample welded at 15 m/min. This upper surface is different from the previous two weld beads. At 15 m/min, the boiling process ejected the metal from the centerline and the solidification rate was increased to a point where the

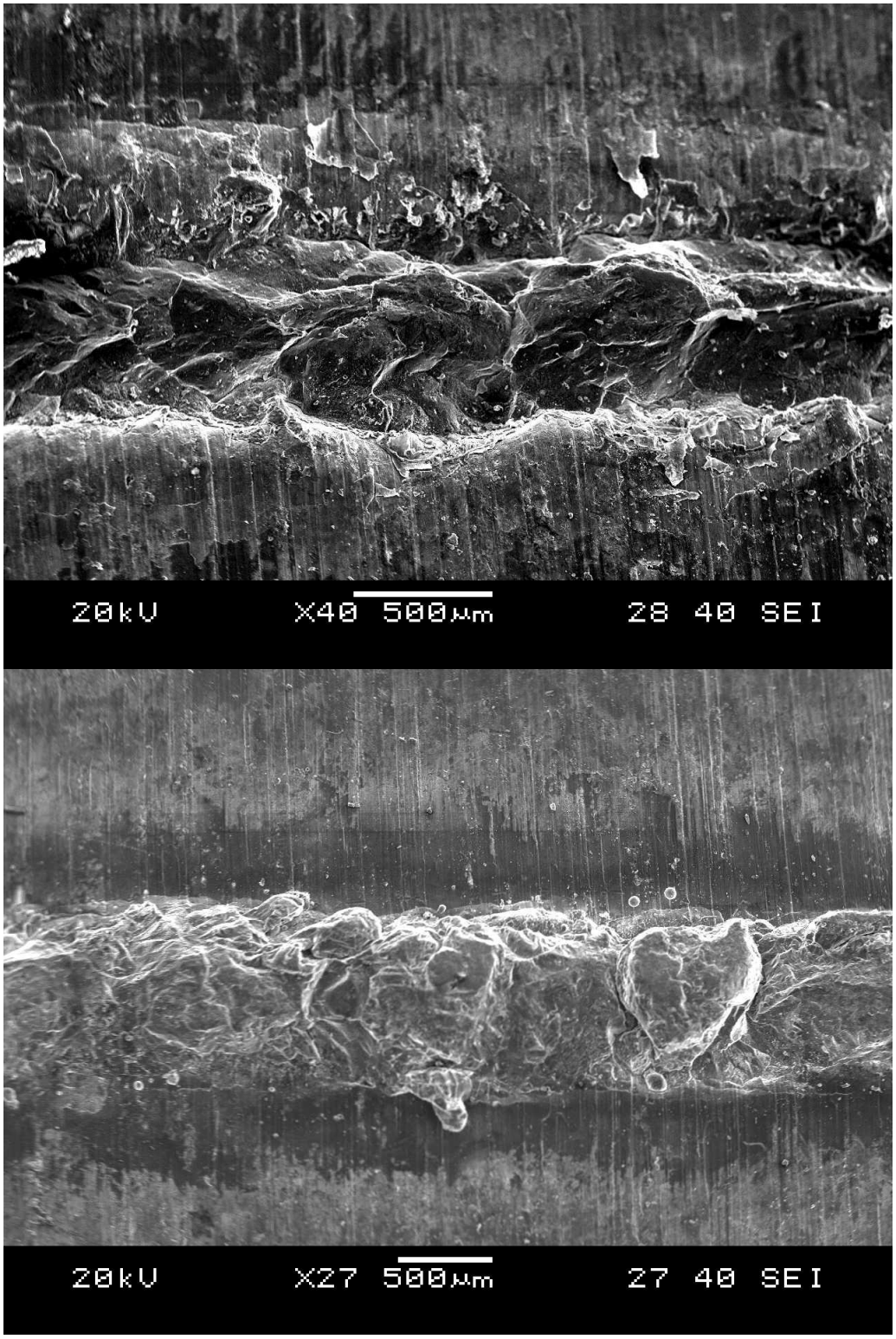

(a)

(b)

Figure 4-31: CO_2 laser weld made at 5 kW and 8 m/min: a) top and b) bottom bead surfaces.

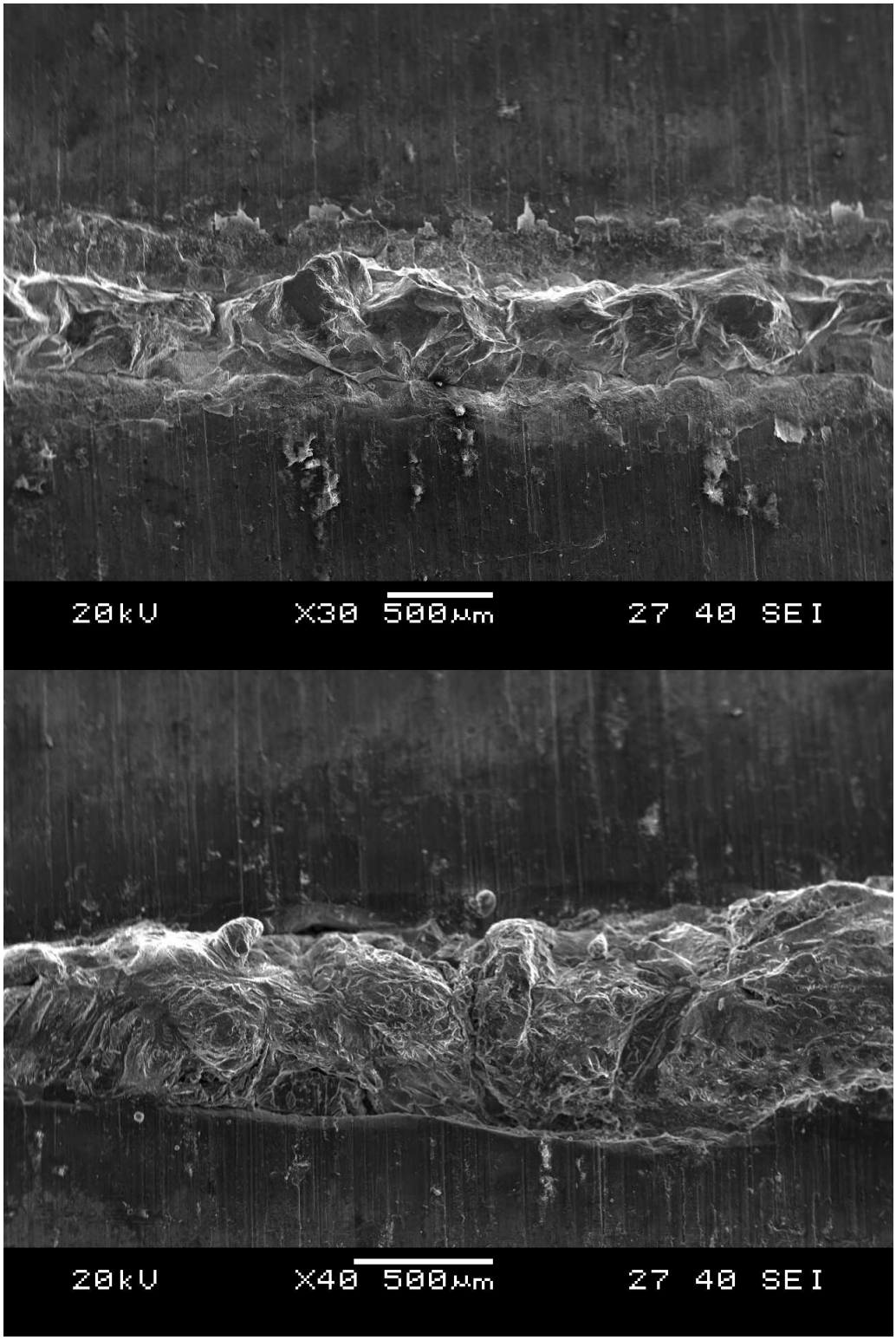

(a)

(b)

Figure 4-32: CO_2 laser weld made at 5 kW and 12 m/min: a) top and b) bottom bead surfaces.

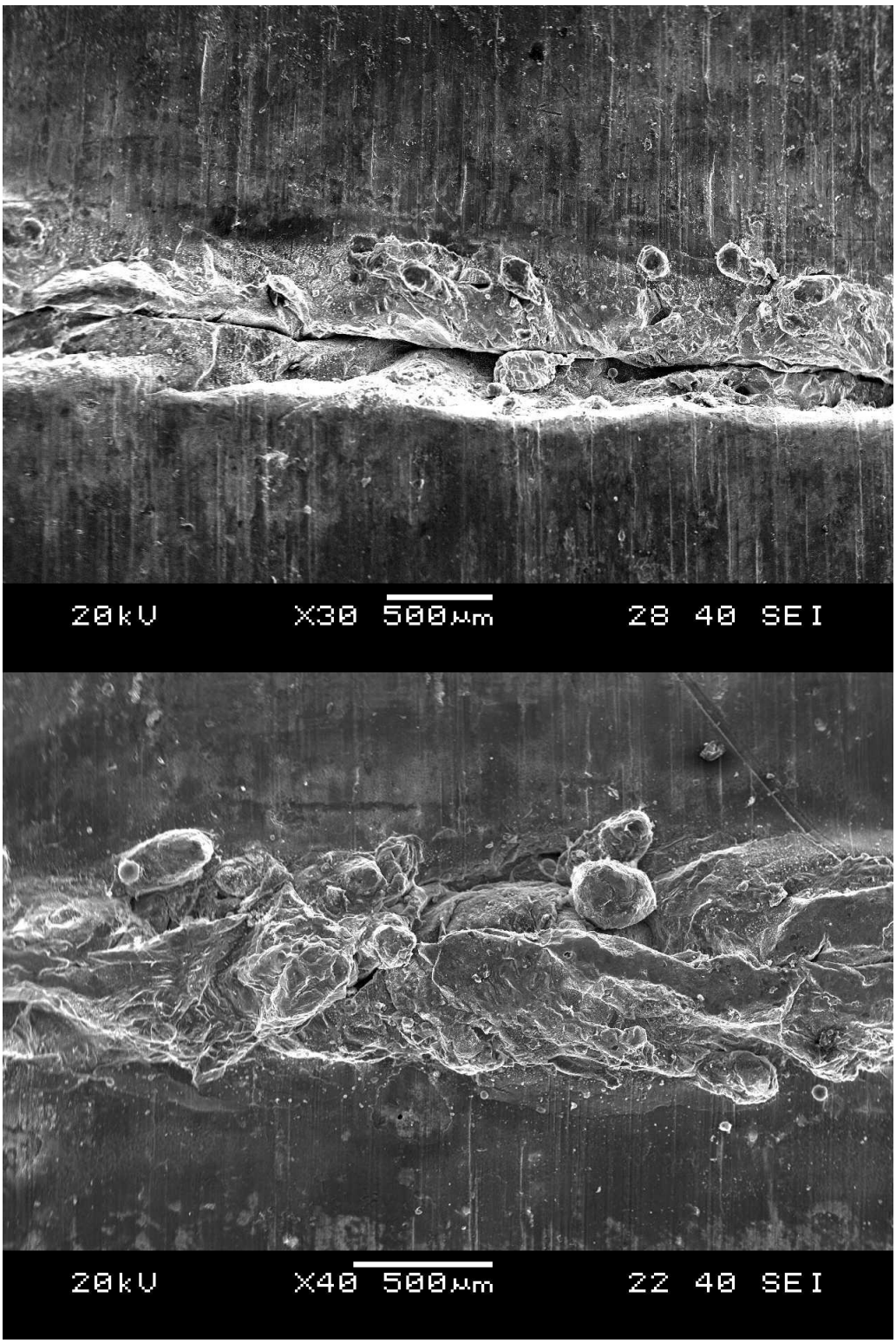

(a)

(b)

Figure 4-33: CO_2 laser weld made at 5 kW and 15 m/min: a) top and b) bottom bead surfaces.

magnesium could not backflow to reform a consistent profile along the weld centerline. This created a centerline seam along the entire length of the weld and rendered this travel speed unviable for mechanical testing.

All of the lower weld bead surfaces exhibited similar features with evidence of spatter, drop-through, expulsion, and overlapping folds of weld metal. These were reasoned to be a result of the creation of the keyhole, high solidification rate, and low surface tension which prevented a continuous root weld surface from forming that could support the molten pool. The shielding used in the creation of the CO_2 welds was also a much more confined jet of helium which would have put more pressure on the top surface and promoted increased drop through. As with the upper surfaces, the 8 and 12 m/min trials were similar in quality and quantity of defects compared to each other despite the travel speed difference. The 15 m/min sample, however, showed a more erratic profile, larger quantity of expelled material and higher concentration of crack initiation points with overlapping solidification.

The surface quality of the 8 and 12 m/min welds were poor and had an abundance of crack initiation points that would inhibit the mechanical performance of the welds. The 15 m/min welds were unacceptable with severe solidification shrinkage along the top of the sample and weld expulsion along the root surface.

4.2.2 Weld Cross Section Analysis

Representative transverse sections of the CO_2 laser welds can be seen in Figure 4-34. The welds all showed a common solidification structure typical of 5 kW CO_2 laser welds. The CO_2 laser welded sections depict the features of operating in the keyhole welding mode, characterized by the high depth-to-width ratio and narrow symmetric fusion zone profile.

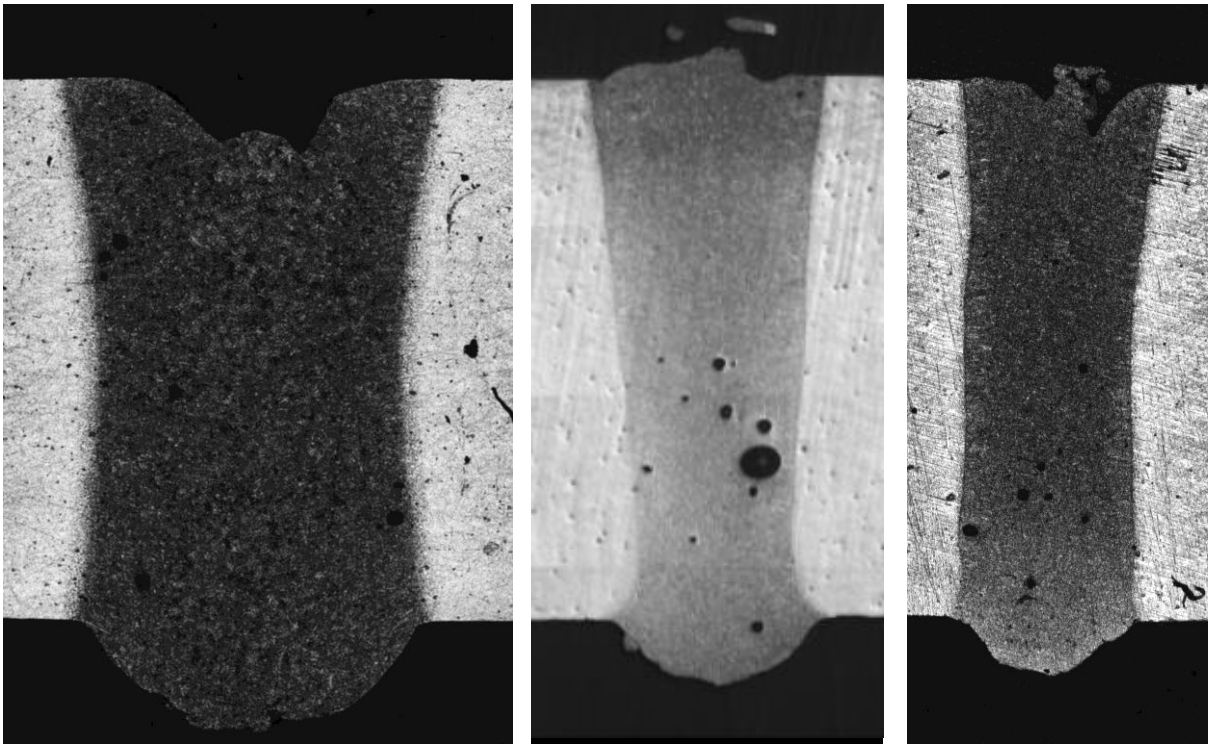

(a) (b) (c)

Figure 4-34: Transverse sections of 5 kW CO_2 laser welds in 2 mm thick AZ31B conducted at: a) 8 m/min, b) 12 m/min, and c) 15 m/min.

The weld microstructures were primarily equiaxed dendritic with only localized instances of columnar-dendritic structures adjacent to the fusion boundary such as may be seen in Figure 4-35.

Drop-through and under-fill continued to be reoccurring defects in the CO_2 laser welding of AZ31B. With the narrow profile of the keyhole weld samples, the under-fill was much smaller in comparison to the drop-through which was exacerbated by the characteristic high rate of material vaporization. Bulk mass loss combined with the violent boiling made the weld upper surfaces inconsistent with certain sections of the weld length experiencing inconsistent profiles and overlapping folds of weld metal. The occurrence of solidification cracking was not observed in any of the CO_2 laser weld trials. This is an advantage of

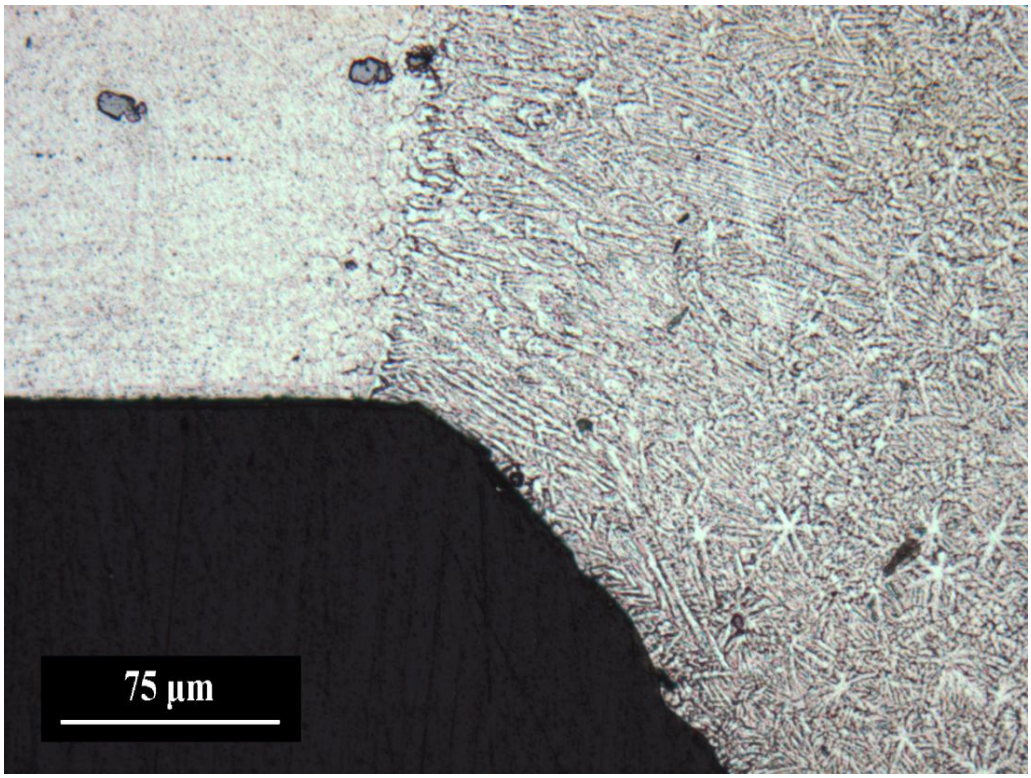

Figure 4-35: Columnar dendrites found in the root side weld toe of the CO_2 laser beam weld made at 5 kW and 15 m/min.

welding with keyhole-mode processes, since the residual restraint stresses are proportional to the volume of heated and molten metal that resolidifies and contracts. Keyhole-mode welding heats a much smaller volume than conduction-mode welding and as such, there is less thermal contraction during solidification. This is believed to be why no solidification cracking was found in the keyhole-mode CO_2 laser welding trials.

As may be seen in Figure 4-34, the CO2 welds exhibited gas porosity. Occluded vapour pores due to keyhole instabilities are normally found toward the center-line of the keyhole mode welds. These observed pores are more likely hydrogen pores as many of them were associated with the fusion boundary where the hydrogen pores would normally be expected to nucleate when solidification begins. There was insufficient time for these bubbles to float

out, so they remained trapped in the weld. Pores act as strain concentration points that reduce the effective cross sectional area and strain distribution of the weld [8, 53].

Figure 4-36 shows the relation between the weld travel speed and fusion zone width. The trend follows a predictable pattern that higher travel speed results in a smaller fusion zone. At 12 m/min, an aberration to the trend was discovered where the size of the fusion zone was drastically decreased and then at a slower speed, the size of the fusion zone reverts back in-line with the determined trend. This narrow weld was thought to be caused by the stabilization of the keyhole at this particular welding condition where a much larger portion of the laser energy was able to pass through the material thickness without being absorbed. At both 10 and 15 m/min, the keyhole suffered from weld pool instability, and with the repeated collapse of the keyhole, the absorption of the laser was improved.

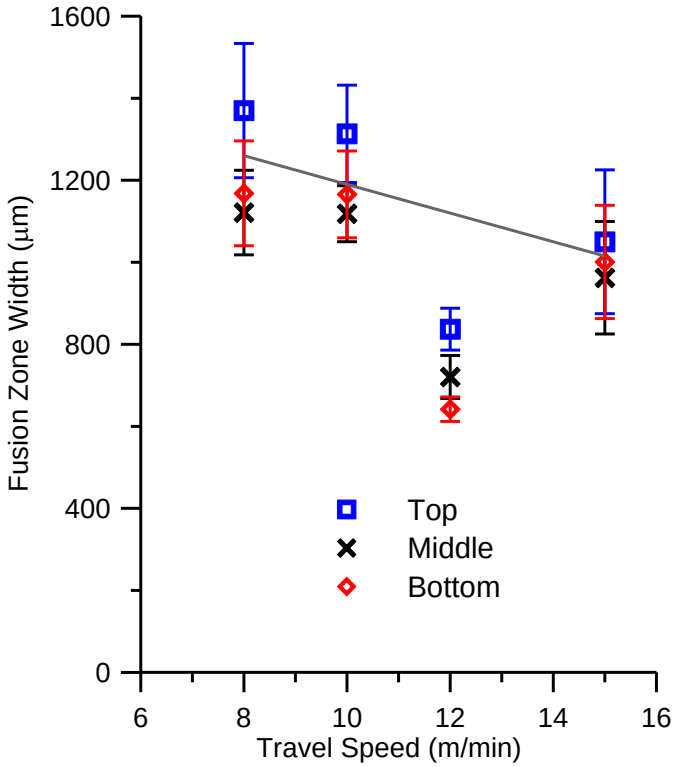

Figure 4-36: CO_2 laser weld width versus travel speed.

Figure 4-37 is a plot of melting ratio versus travel speed. A similar trend to the weld widths is seen where the 12 m/min trial was the lowest recorded melt ratio of any of the CO_2 laser weld trials. Compared to the diode laser melting ratios which achieved a maximum of 18%, the CO_2 laser welding process was more erratic with the lowest efficiency weld achieving a 10% melting ratio and the 15 m/min weld experienced much higher weld efficiency, exceeding 20% on average.

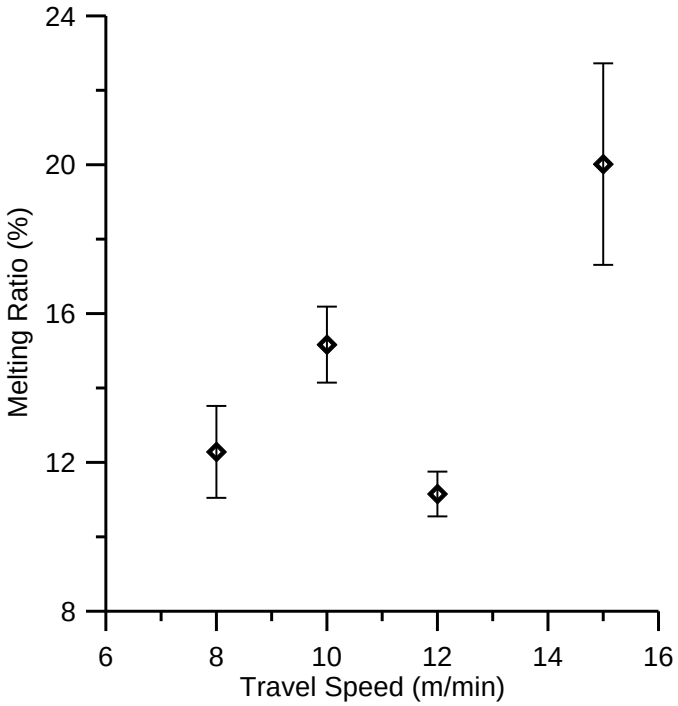

Figure 4-37: CO_2 laser welding melting ratio versus travel speed.

4.2.3 Tensile Tests and Micro-Hardness Measurements

Transverse tensile tests were performed on welds made at 8 and 12 m/min. These were chosen for further investigation as they were the two extremes of weld width and had more consistent weld bead quality compared to the 15 m/min travel speed trials. The results of the CO_2 transverse tensile tests are shown in Figure 4-38. Both travel speeds resulted in tensile samples that experienced almost no base metal plastic deformation as the overall stress

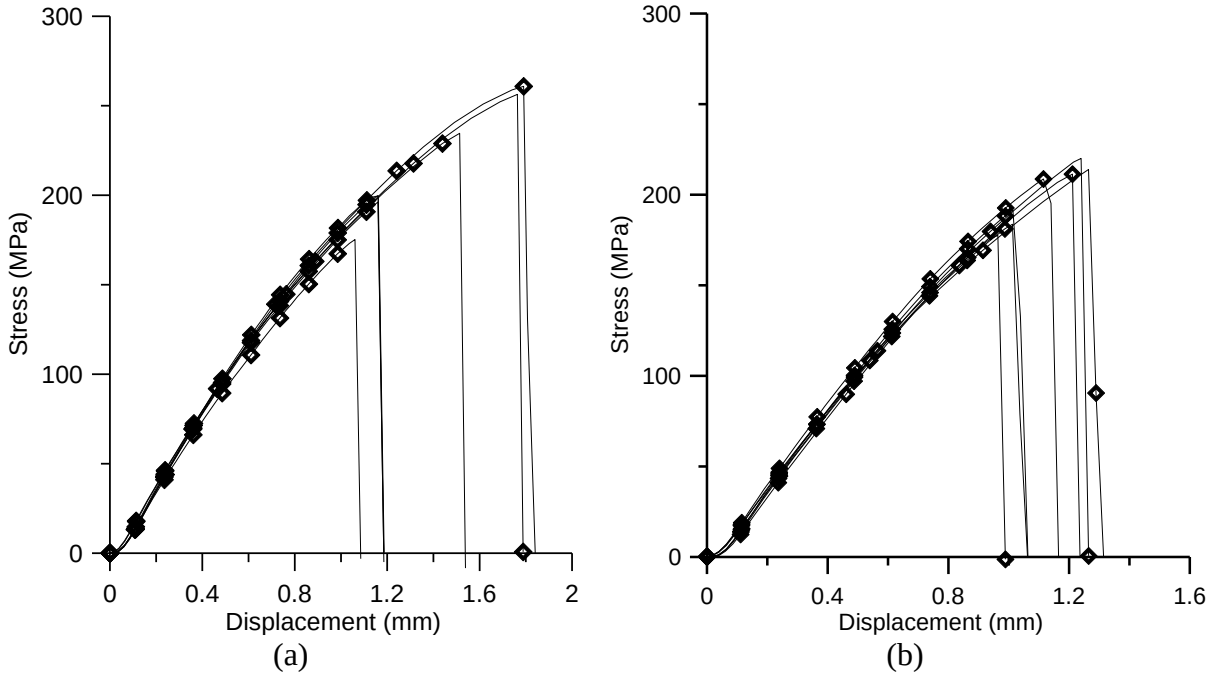

Figure 4-38: Measured stress versus cross-head displacement of the CO_2 laser welds made at: a) 5 kW and 8 m/min and b) 5 kW and 12 m/min.

versus elongations graphs were essentially straight lines. This was experienced in the previous diode laser trials where the weld material was also weaker than the surrounding base material. This caused the sample to experience strain localization in the weld fusion zone resulting in the sample failing in the weld metal before it experienced significant elongation compared to the base metal.

The results of the tensile trials are summarized in Figure 4-39 as a percentage of the base metal properties. The welds made at 8 m/min can be seen to have the higher ultimate strength at an average value of 222 MPa compared to those made at 12 m/min which averaged only 200 MPa. The elongation was also slightly greater in the 8 m/min samples while the yield point was higher at the 12 m/min travel speed. This is a related occurrence as the low speed trail produced a much wider weld fusion zone that, like in the diode trials, is

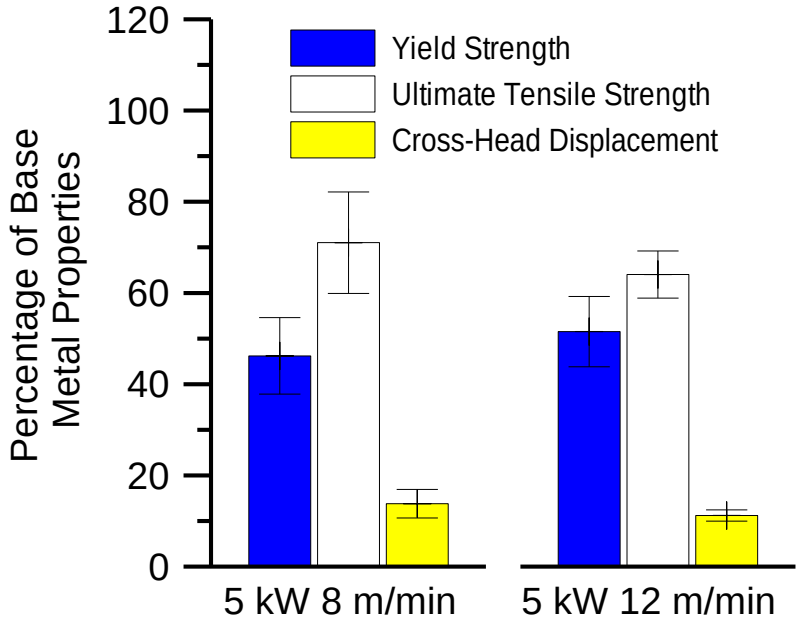

Figure 4-39: CO_2 laser weld transverse tensile properties as a percentage of the base metal properties in the rolling direction.

where all samples experienced failure. With the weld being the weak point in the sample, it was also the only region that experienced deformation before failure. Therefore, with the wider fusion zone, there was more material to deform, which allowed for greater overall elongation but still only achieved approximately 12% of the elongation of the base material.

The CO_2 tensile results demonstrated an improvement over the conducted diode weld samples with an increased from 58% to 70% of the ultimate tensile strength of the base metal. Neither the yield strength nor the elongation experienced by the weld samples was affected by the change of welding process. Similar to the diode laser welds mechanical properties, the inconsistent weld profiles and abundance of strain localizing defects in the CO_2 laser welds prevented the CO_2 welds from achieving properties approaching those of the base metal.

A representative micro-hardness profile for the CO_2 laser trials is shown in Figure 4-40. The profile is softest in the fusion zone at an average value of 60 VH_{25}, and then through the heat affected zone, the measured values increase to the base metal hardness of approximately 75 VH_{25}. These results are similar to the previous reported results in the diode laser welding trials, the only difference being that the CO_2 laser operated in keyhole-mode welding, so the weld widths are narrower.

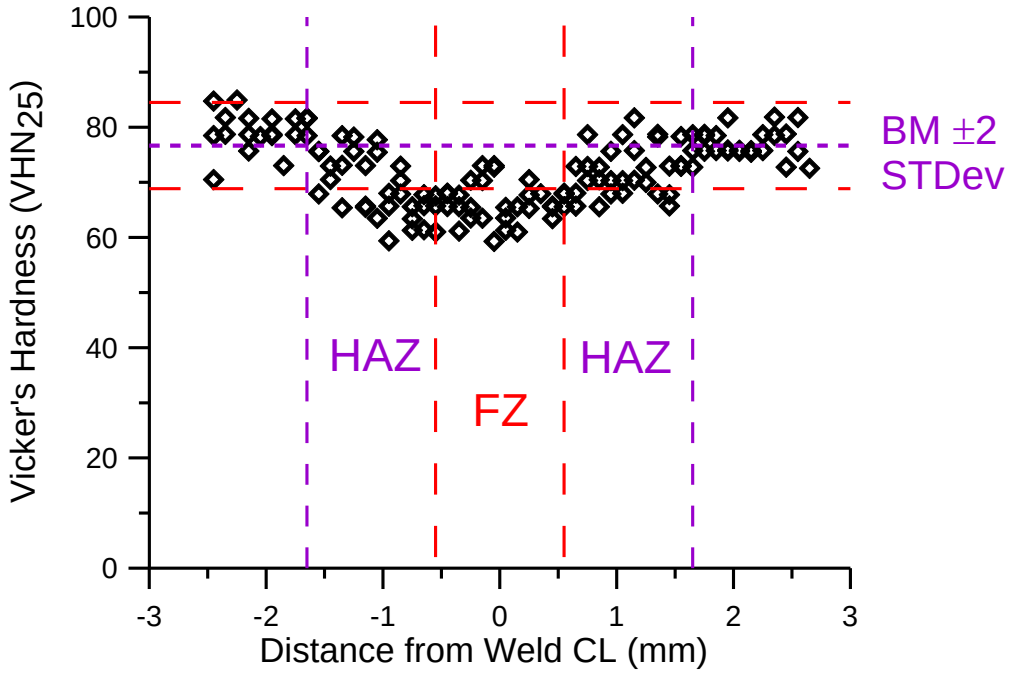

Figure 4-40: Vickers micro-hardness profile of the CO_2 laser weld made at 5.0 kW and 15 m/min.

The 5 kW CO_2 laser welding process produced low surface quality welds. The welds exhibited excessive boiling, expulsion, under-fill, drop-through, overlapping solidification, hydrogen porosity, and center-line under-fill at high travel speeds. The occurrence of solidification cracking was avoided by welding in keyhole mode instead of conduction mode. This limited the size of the weld and the heat affected zone and increased the overall process speed. Fracturing in the fusion zone of all samples, ultimate tensile failure occurred at an

average of 70% of the base materials ultimate tensile strength, otherwise, the optimized CO_2 welds were comparable to those previously achieved with the diode laser system, achieving yield strengths of approximately 50% and cross-head displacement at failure averaging 12% of the base metal properties. Overall, the CO_2 laser welding process was able to produce stronger weld specimens than the diode laser system at much higher welding speeds.

4.3 Fibre Laser Welding Results and Discussion

All fibre laser welding samples were prepared with milled edges and cleaned with acetone and ethanol and had the surface oxide removed by stainless steel wire brushing. The weld parameter optimization was conducted on samples with chamfered corners and similar to the CO_2 laser, the fibre laser was operated in keyhole-mode.

4.3.1 Weld Bead Surface Quality

The visual appearance and weld bead surface quality of the fibre laser welds are classified and are presented in Figure 4-41 as a function of weld power and laser travel speed. Visually acceptable weld beads were achieved at a combination of low laser power and low travel speed. At low power and high travel speeds, the welding process did not have enough energy to fully penetrate the sheet. The largest region was classified as rough weld surfaces and was evident with the high laser power settings. With a laser beam power density of 90 GW/m^2 at the focal plane for 6.5 kW, power settings beyond 6.5 kW were not tested because they would only produce further unacceptable welds before progressing to a cutting process at higher power levels. Power settings below 2 kW, 28 GW/m^2 at the focal plane, were not used because the 10 kW fibre laser was not stable below 1.5 kW power.

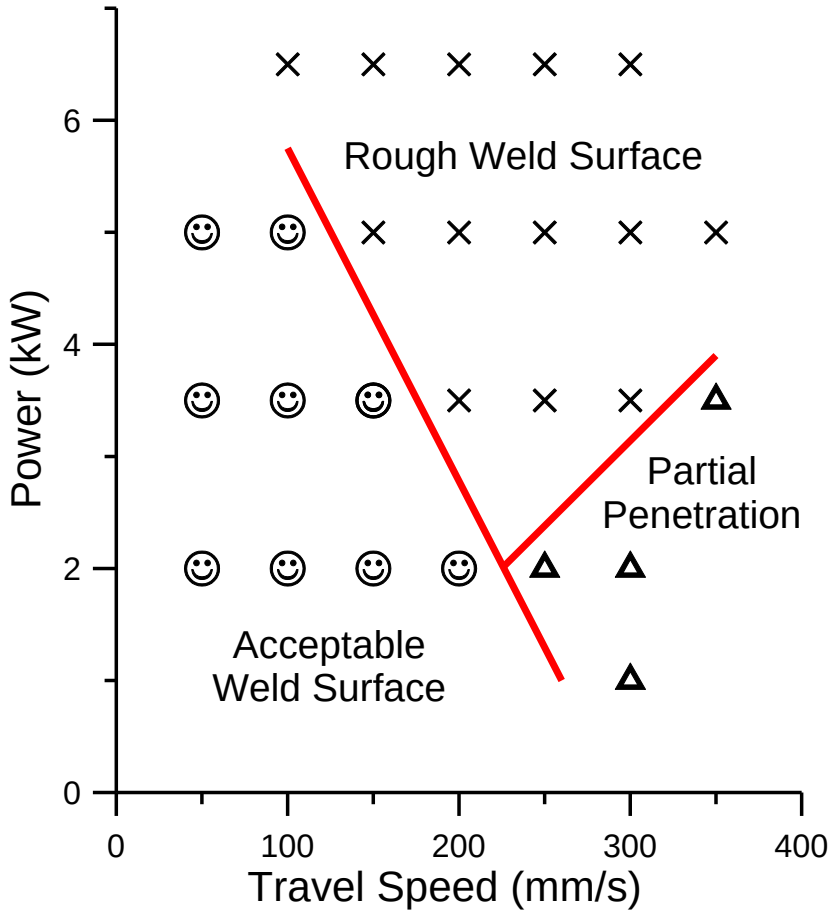

Figure 4-41: Fibre laser welds acceptability chart.

The top and bottom root weld bead surfaces of welds made using three different sets of weld parameters are shown in Figure 4-42 through Figure 4-44. The first two welds were made using 2 kW and welding speeds of 50 and 150 mm/s, respectively. Figure 4-42a and Figure 4-43a show the effect of increasing the travel speed on the solidification pattern of the weld pool. At the slow travel speed, the solidification time was increased and the trailing edge of the molten pool exhibited a rounded ripple pattern. When the welding travel speed was increased to 150 mm/s, the crescent pattern became noticeably elongated along the weld seam transitioning to a V-shaped solidification profile. The solidification wave pattern was produced by the weld pool lapping over the previously solidified material and creating cold

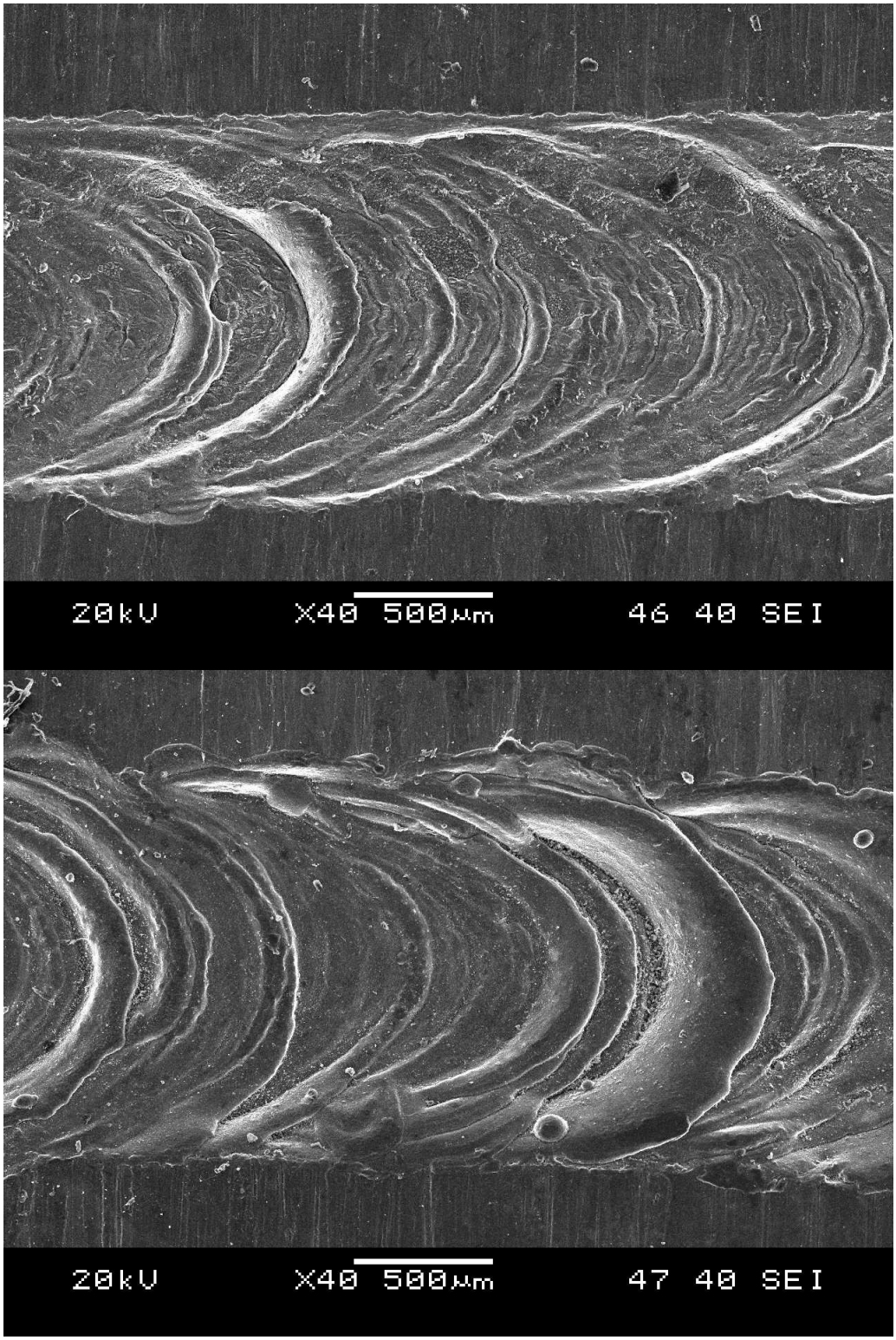

(a)

(b)

Figure 4-42: Fibre laser weld made at 2 kW and 50 mm/s: a) top and b) bottom weld bead surfaces.

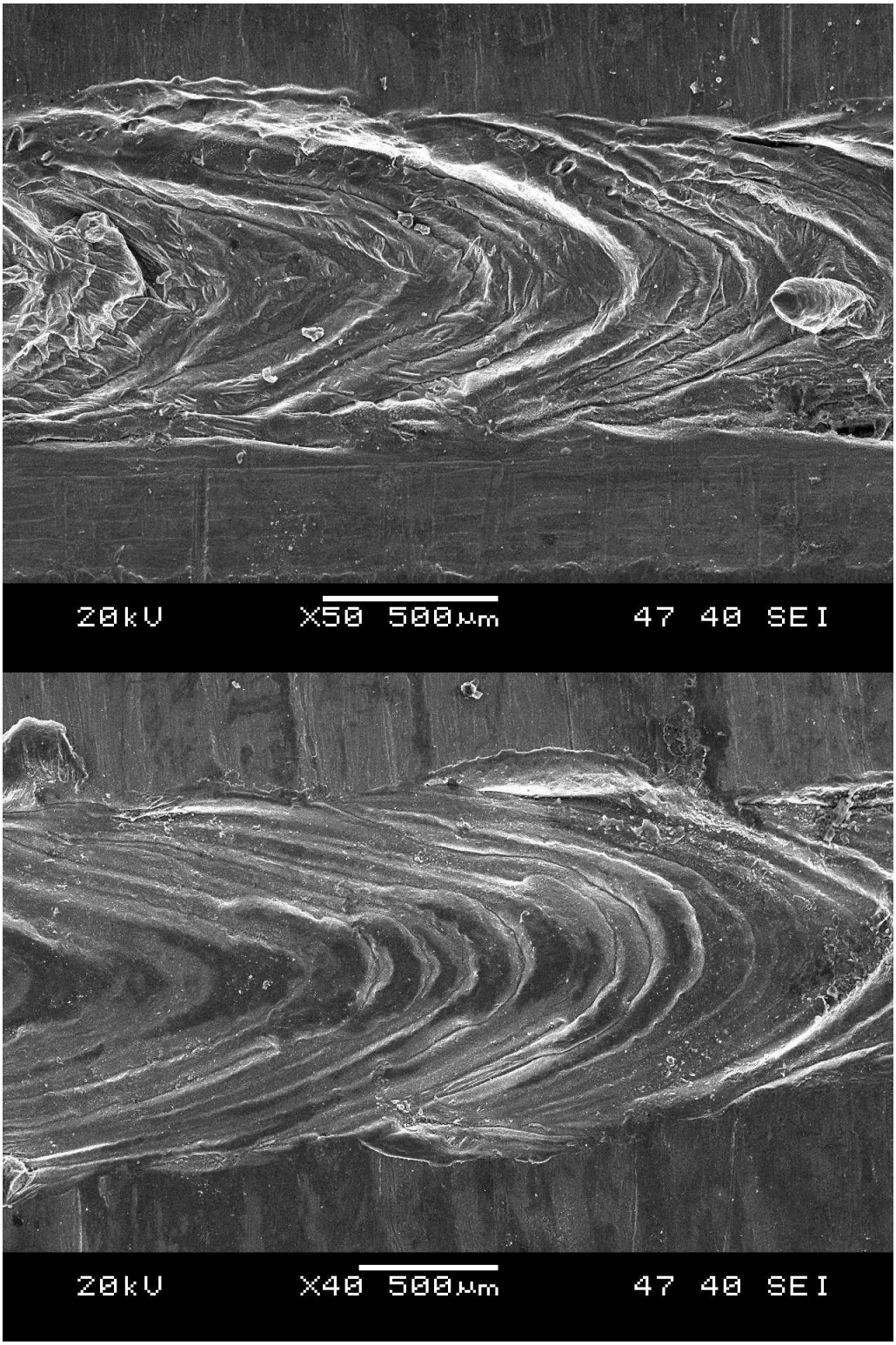

(a)

(b)

Figure 4-43: Fibre laser weld made at 2 kW and 150 mm/s: a) top and b) bottom weld bead surfaces.

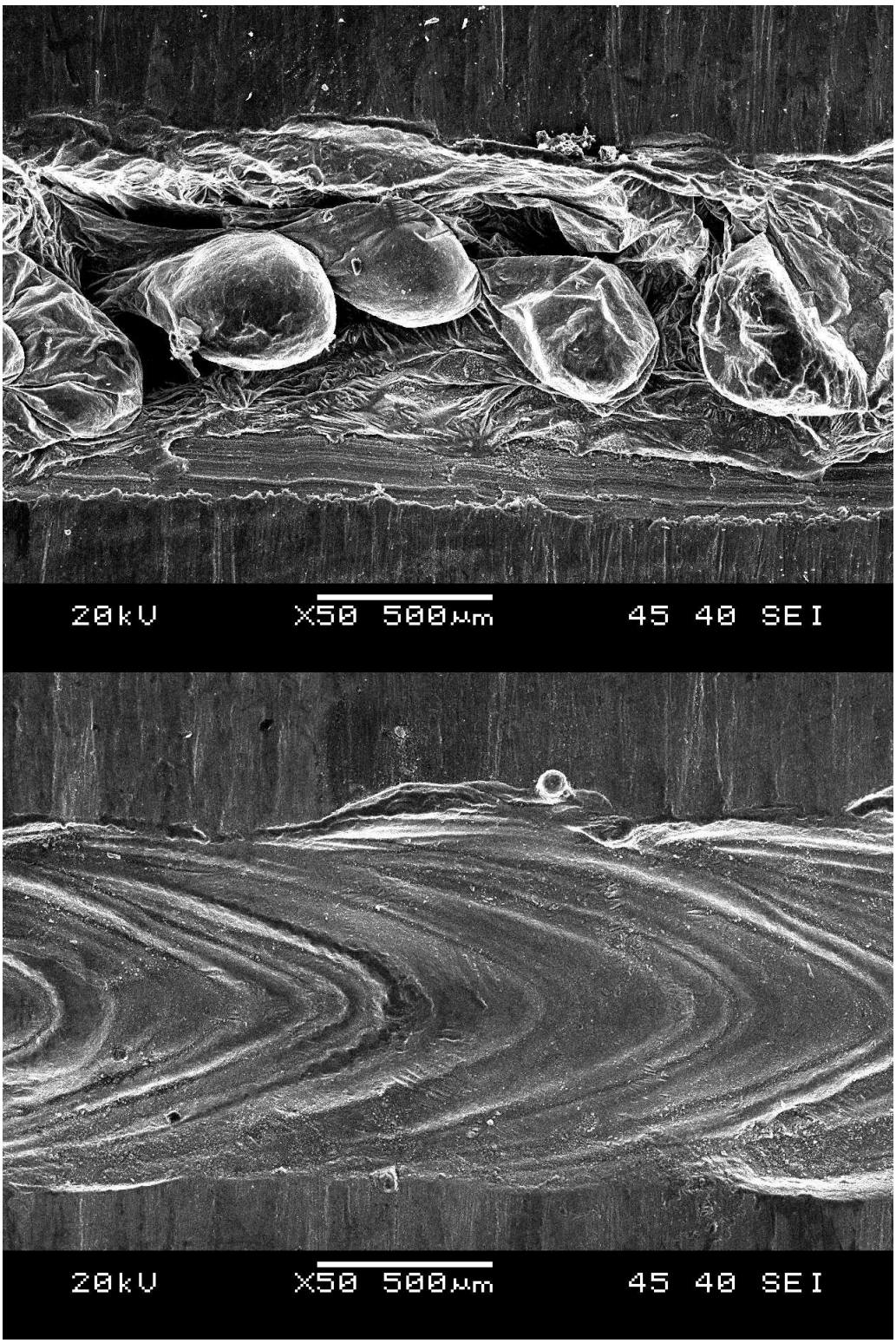

(a)

(b)

Figure 4-44: Fibre laser weld made at 5 kW and 150 mm/s: a) top and b) bottom weld bead surfaces.

shuts. Cold shuts generally have poor wetting along the upper edge and will act as crack nucleation points during tensile or fatigue loading. Both the slow rounded weld bead surface profile and the elongated sharper patterns were consistent and well distributed along the entire length of the welds. These were both classified as acceptable welds, while the third weld made at 5 kW and 150 mm/s, shown in Figure 4-44, was classified as an unacceptable rough surface weld. The bottom surface profile of all three samples exhibited an acceptable quality profile with similar transition from the low travel speed welds' almost circular crescent shape to the high travel speeds' increasingly angular weld pattern. The upper surface of the third weld at 5 kW and 150 mm/s was representative of the welds in the rough surface profile region. The high power input and reduced solidification time resulted in significant molten metal expulsion from the weld pool that froze before the molten metal was able to settle and reform an even surface. Similar to the CO_2 laser weld trials, the high energy density fibre laser beam led to boiling of the magnesium alloy and the droplet-like structure of solidified expulsion jets as shown in Figure 4-44a which were retained in the final weld bead solidification structure. The expulsion experienced in these weld left a large number of sharp corners in the weld bead surface that would act as crack initiation points when the weld is subject to tensile or fatigue loading. The welds in the partial penetration region were identified by the root side of the weld which did not show any signs of melting and along with the rough surface welds, were determined to be unacceptable for further testing.

4.3.2 Weld Cross Section Analysis

All of the 2 kW fibre laser welds as well as all of the 150 mm/s welds were sectioned for analysis. Three sections were prepared, shown in Figure 4-45, one from each region of the acceptability chart in Figure 4-41. In Figure 4-45a, the acceptable surface quality sectioned sample shows excellent surface conditions despite having experienced some reduction of the cross sectional area due to the chamfering of the interface edges to remove machining burrs. This chamfering can be seen along the bottom surface of Figure 4-45c. No evidence of cold shuts was found in any of the polished sections. The surface ripples shown previously could be discerned but no seams or overlap problems were identified. The center sample is a representative section from the rough surface region and was sectioned through one of the expelled droplets. This section illustrates how the solidified expulsion jets are physically attached to the fusion zone. The strength of any weld with these droplets will also be further limited by the pre-existence of the incipient cracks along the welds upper surface on either side of the expelled jet. Similar to the cold shuts, the expulsion jet forms a very sharp edge with the remainder of the fusion zone when they are still attached. These incipient cracks can be seen along the top of the fusion zone in Figure 4-45b. All of the welds experienced hydrogen porosity but to a far lesser extent than was documented with the CO_2 laser welding process where large scale hydrogen pores were consistently found. For the fibre laser weld sections, the average pore was under 50 μm and these were only found intermittently. This significant decrease in hydrogen porosity can be attributed to the fact that the pre-existing grey hydrated oxide was removed from all weld specimens surfaces prior to welding by stainless steel wire brushing.

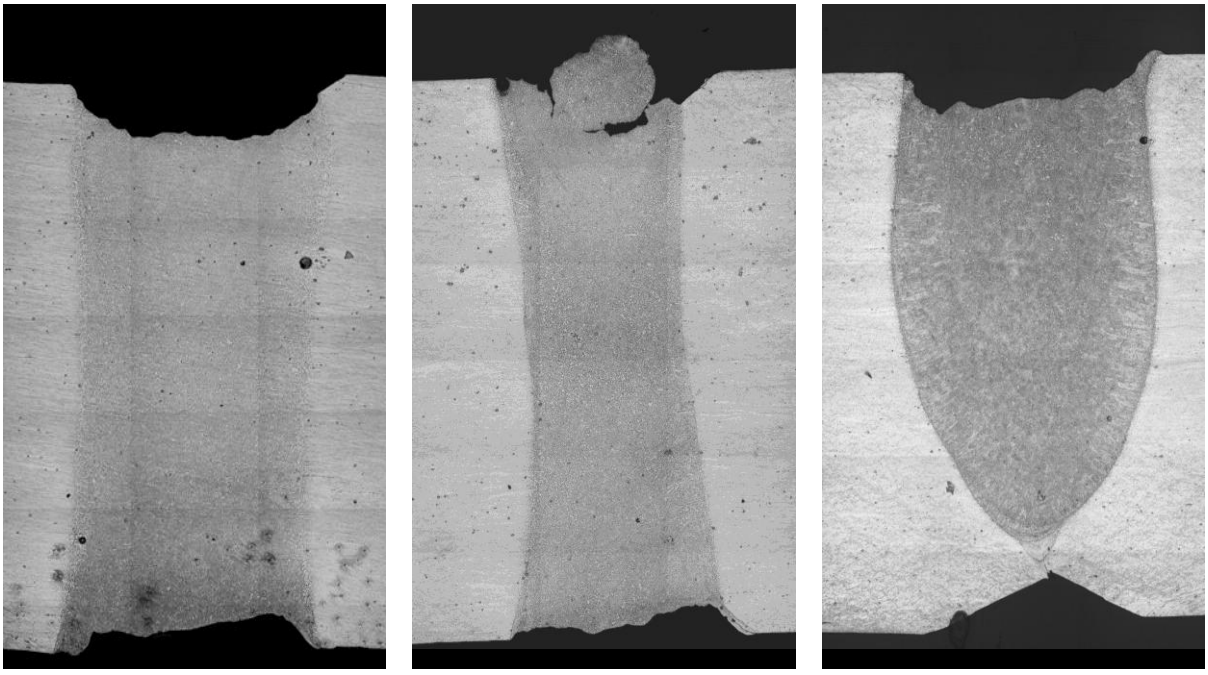

(a) (b) (c)

Figure 4-45: Representative transverse sections of the 2 mm thick sheet fibre laser weld fusion zones made at: a) 2 kW and 50 mm/s, b) 3.5 kW and 150 mm/s, and c)2 kW and 250 mm/s.

Figure 4-46 and Figure 4-47 depict the weld profile measurements conducted on the samples welded at 150 mm/s. As the fibre laser power was reduced, the resulting MBMA increased. This was an unexpected result, generally, as more power is put into the system, the resulting fusion zone would also increase. The cause of this was determined to be a result of the keyhole. In all cases at 150 mm/s, the keyhole was formed and permitted a large portion of the laser energy to pass through the sample. The higher power settings had such high power density so the material experiencing the incident laser was vaporized and transformed into plasma at a higher rate. This created a more stable keyhole, which inhibited the laser energy from entering the weld since the majority of the laser beam passed through the larger, more stable keyhole without interacting with the weld metal. The low power

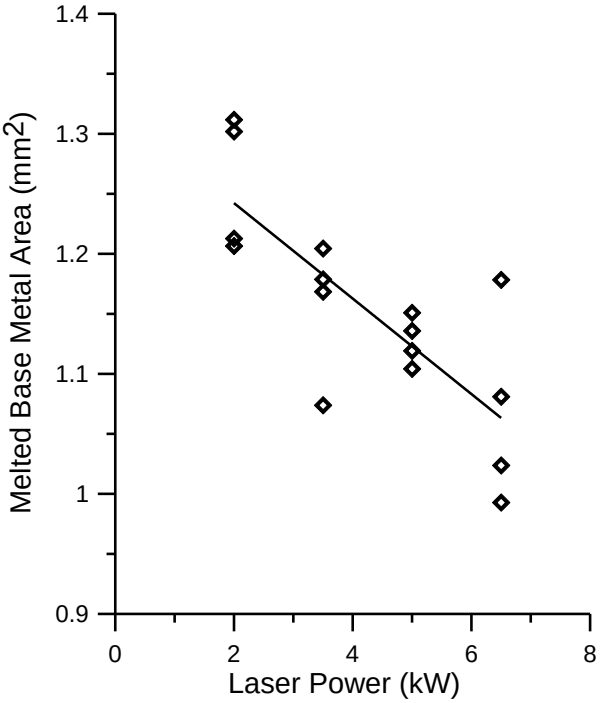

Figure 4-46: MBMA versus laser power for the fibre laser welds made at 150 mm/s travel speed.

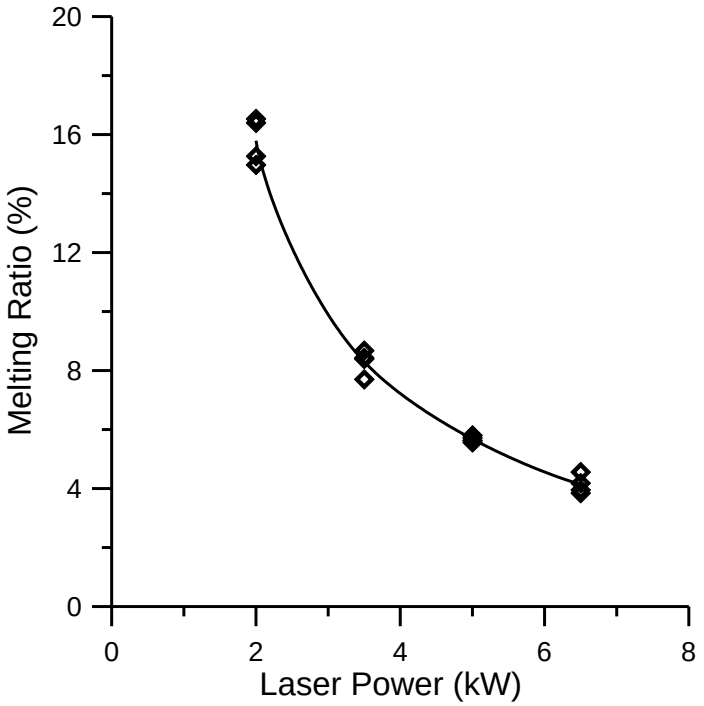

Figure 4-47: Melting ratio versus laser power for the fibre laser weld made at 150 mm/s travel speed.

levels would also have experienced possible keyhole instability that would have led to the keyhole collapsing and additional incidence of the laser on the molten pool. This would have also increased the weld heating of the low power trials over the higher power settings. The consequence of this significant loss of energy coupling at the high power levels was then the observed overall reduction of the fusion zone area. The results of the variable power input showed similar results in the melting ratios, seen in Figure 4-47, where the higher power settings were less efficient. The highest efficiency was achieved at the lowest power setting where the largest weld fusion zone was produced with about 16% melting ratio.

A similar set of plots were created for the samples welded at 2 kW and are shown in Figure 4-48 and Figure 4-49. The welds conducted at 2 kW power setting did not present any indication that this power produced significant boiling or weld pool expulsion. The measurement of the MBMA was again the more interesting of the two plots and depicted a trend that the size of the fusion zone is primarily unaffected by the travel speed. The 300 mm/s trial did not penetrate even half the sheet thickness and at such a high travel speed, could not create a keyhole. The other extreme of travel speed, at 50 mm/s, simply had so much time to heat the weld pool that the magnesium's' thermal capacity to transfer the energy away from the weld was exceeded and the MBMA was able to grow.

The melting ratio versus travel speed plot in Figure 4-49 shows that the laser efficiency increased with welding speed to a maximum value of about 27% at 250 mm/s where there was a transition to partial penetration welding. At 27% melting ratio, much better than the diode or CO_2 laser efficiencies (max 18%), the fibre laser melting ratios indicate the absorptivity of the magnesium was much higher for the fibre laser beams wavelength.

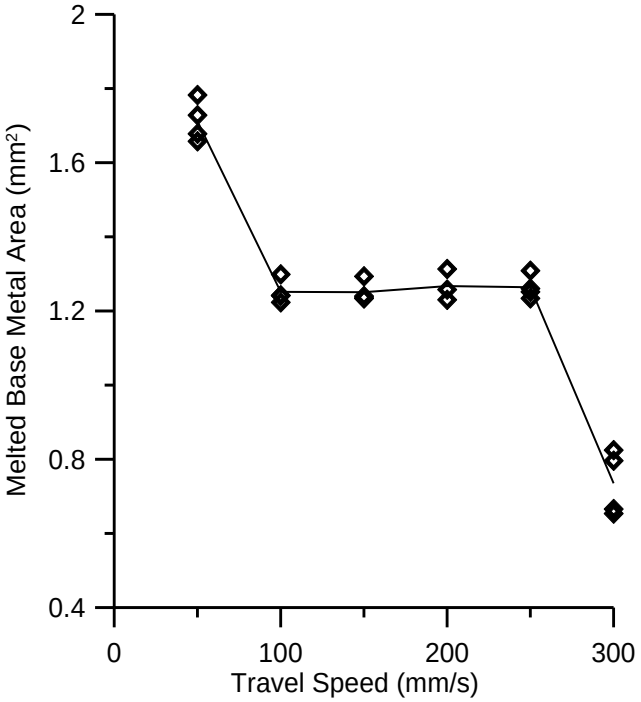

Figure 4-48: MBMA versus laser power for the fibre laser welds made at 2 kW laser beam power.

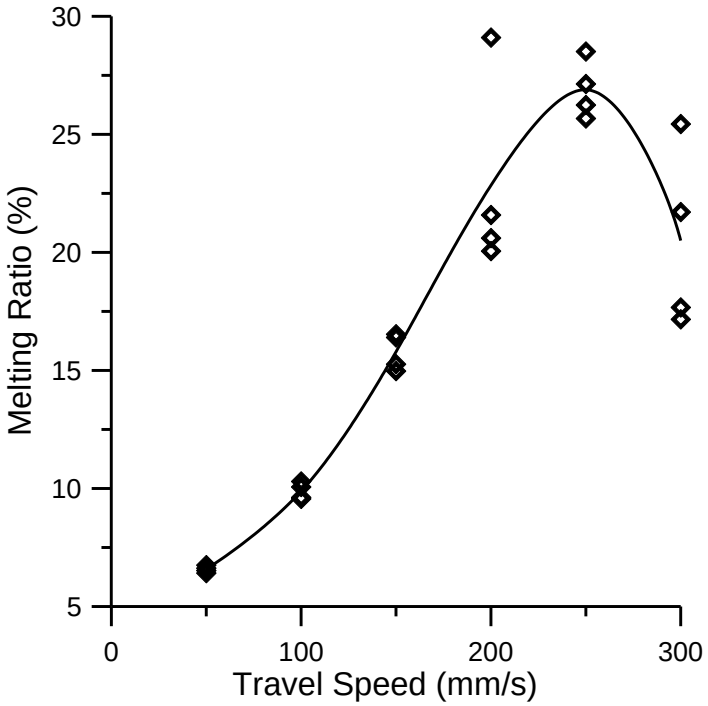

Figure 4-49: Melting ratio versus laser power for the fibre laser welds made at 2 kW laser beam power.

Deutsch *et al.* [47] have reported on melting ratios realized with Nd:YAG laser welding processes when working with 5754 and 5182 aluminum alloy sheet. The maximum MR reported approached 30%. This was similar to the highest melting ratios produced with the AZ31B magnesium with the fibre laser but much higher than either the diode lasers efficiency of 18% or the CO_2 laser's 20%. Nd:YAG generally offers higher efficiency welds for aluminum because the spectral absorptivity of aluminum is highest in the vicinity of the laser's 1.06 μm wavelength [9, 12, 17, 45]. No such data was found for magnesium from the collected data.

4.3.3 Microhardness and Tensile Test Results

From the analysis of the weld sections, the 2 kW fibre laser welds were determined to be the most promising due to the lack of heavy boiling or expulsion. Therefore, full size samples for transverse tensile testing were made using two travel speeds of 50 and 100 mm/s. The tensile sample edges were not chamfered in the tensile welding samples. This increased the amount of metal available to the weld pool and minimized the reduction of the cross-sectional area observed in the transverse sections. The stress versus elongation curves for the 50 mm/s samples are shown in Figure 4-50. The results for the welds made at 100 mm/s are not shown but were similar. The two sets of fibre laser tensile trials both produced tensile samples that were strong enough to produce a definitive transition between elastic and plastic deformation. The average 50 mm/s sample exhibited yielding at approximately 197 MPa. The samples then failed at an average cross-head displacement of 2.6 mm and an ultimate tensile strength of 253 MPa. The 100 mm/s specimens actually outperformed the 50 mm/s samples with average values of 205 MPa yield strength, 269 MPa ultimate strength, and

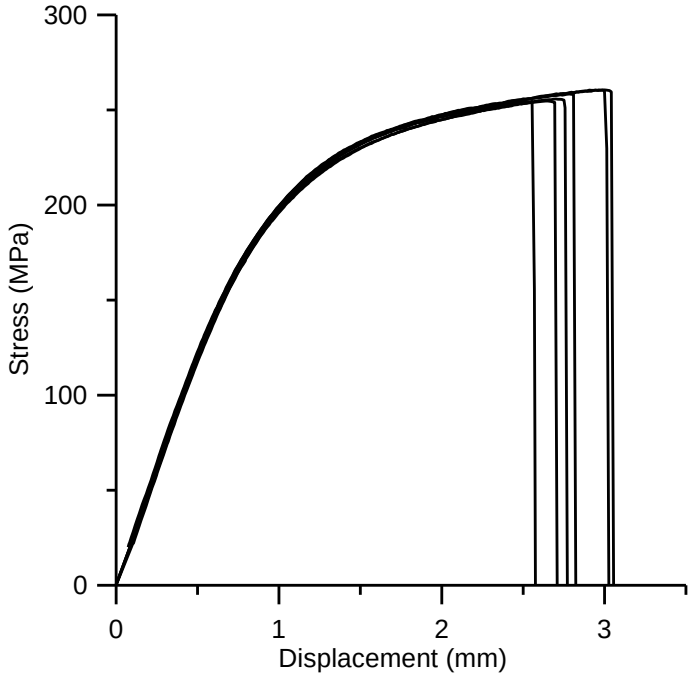

Figure 4-50: Measured stress versus cross-head displacement of the fibre laser welds made at 2 kW and 50 mm/s.

3.0 mm elongation. The fracture surfaces for the fibre laser trials were similar to those of the base material in that the fracture surface showed evidence of ductile failure and progressed along a 45° angle similar to those depicted previously in Figure 4-25b and Figure 4-26b. The failure for all the fibre weld samples initiated at a weld toe and propagated through the fusion zone.

A summary of the mechanical properties of the fibre laser welds are shown in Figure 4-51 as percentages of the base metal properties in the rolling direction. The ultimate tensile strength of the welds made at 100 mm/s were 86% of the base material ultimate tensile strength. The yield strength was over 75% of the base material properties, but the samples still suffered from serious limitations in overall elongation, managing only 30% compared to the base metal.

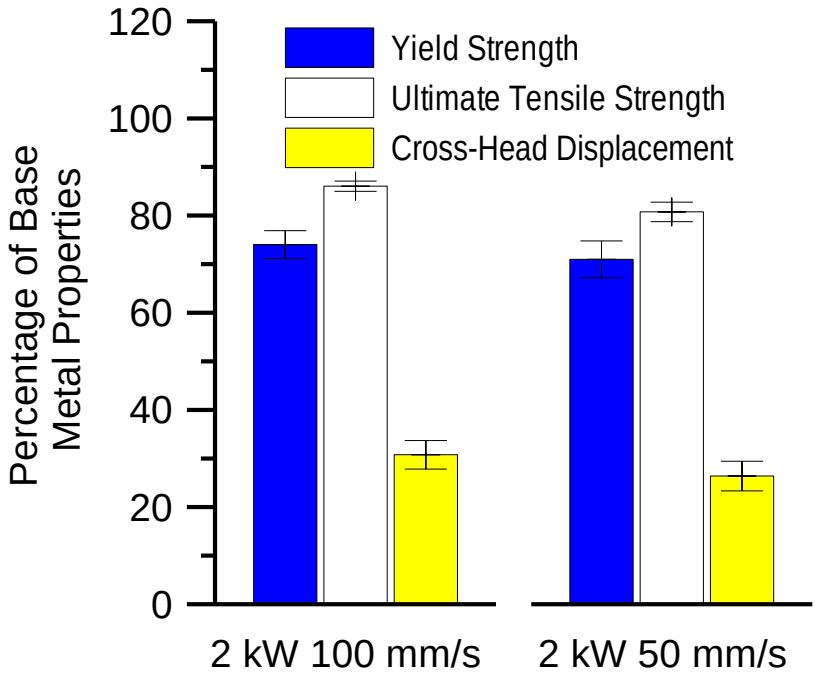

Figure 4-51: Fibre laser transverse tensile properties as a percentage of the base metal properties in the rolling direction.

Two micro-hardness profiles for the welds made at 2 kW and 150 mm/s and at 3.5 kW and 150 mm/s are shown in Figure 4-52 and Figure 4-53, respectively. Similar to previous hardness profiles conducted on both the diode and CO_2 laser welds, the fibre laser welds showed that the fusion zone was the softest region with the heat affected zone transitioning from the fusion zone hardness to the base metal hardness with no region of localized softening anywhere in the weld profile.

The fibre laser welds were the highest quality welds produced by any of the laser beam welding processes used in this study. The percentage reduction of ultimate tensile strength is now in direct proportion to the measured reduction in hardness. The surface bead quality profile was even and consistent with the weld fusion zone showing only small infrequent occurrences of hydrogen porosity. The optimized weld parameters using a low laser beam

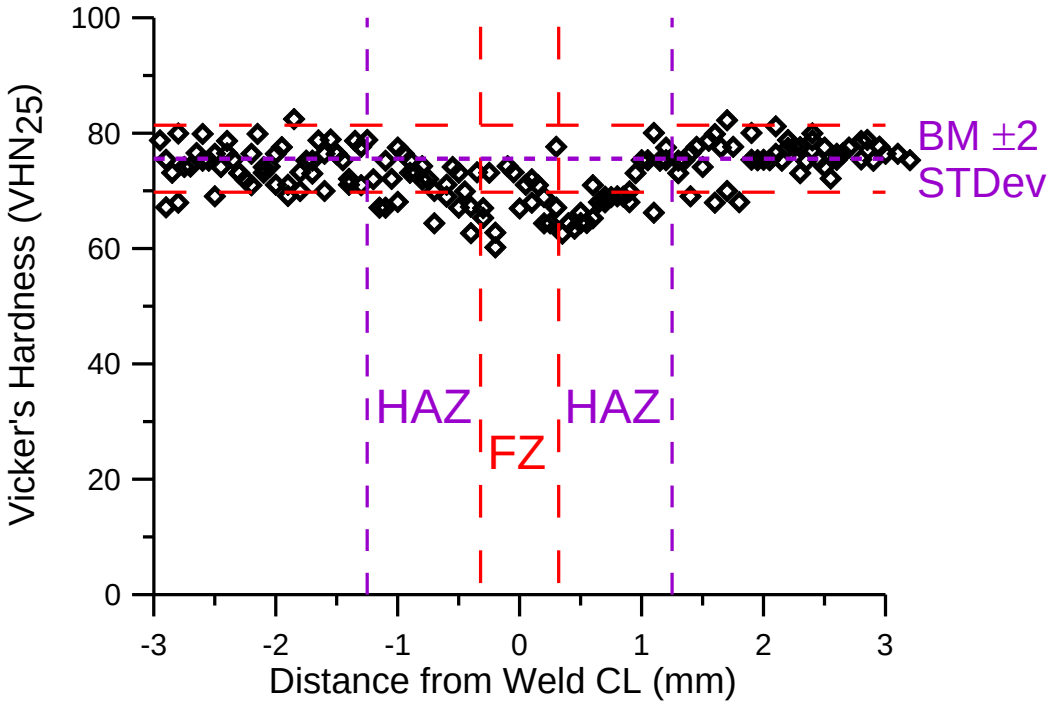

Figure 4-52: Vickers micro-hardness profile of the fibre laser weld made at 2.0 kW, 150 mm/s.

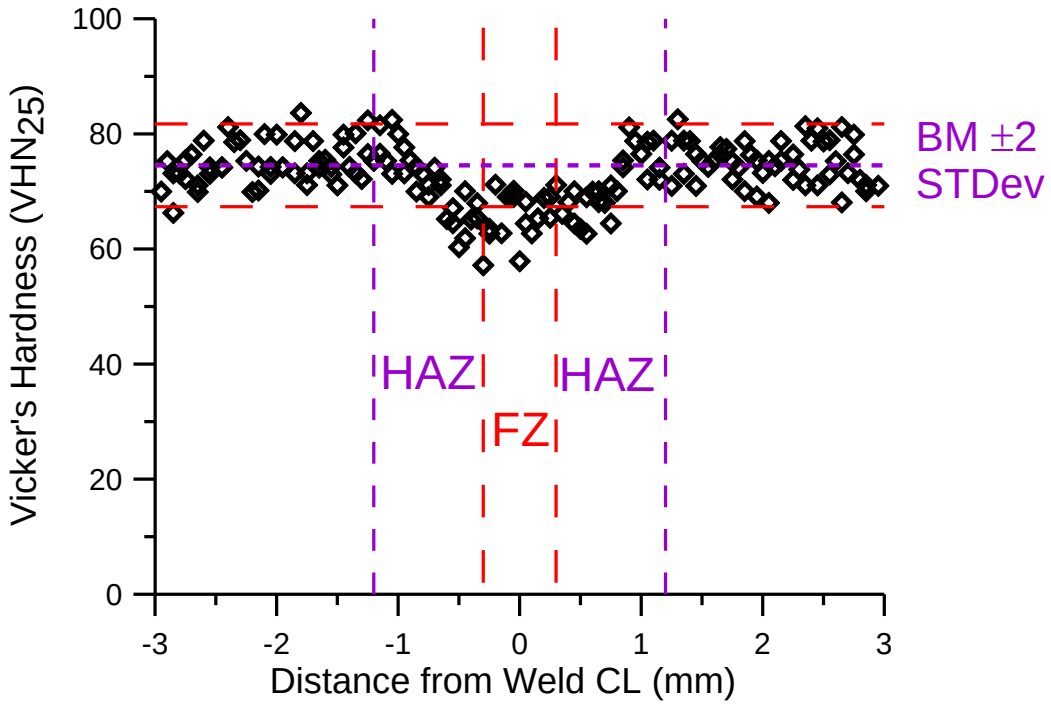

Figure 4-53: Vickers micro-hardness profile of the fibre laser weld made at 3.5 kW, 150 mm/s.

power and slow travel speed produced a fusion zone that was primarily free of ductility-limiting defects. Compared to the conduction-mode diode welding process, at 100 mm/s (6 m/min), the fibre welds were over 10 times faster than was possible with the diode laser and the high end of the acceptable bead quality region, 200 mm/s (12 m/min) was comparable to the CO_2 laser welds.

4.4 Laser Welding Results Comparison

With all three laser welding processes optimized and data analyzed, not one of the lasers was able to produce a laser welded specimen that was the equal of the base metal properties. It should be recognized that under ideal conditions, the best that could be reasonably expected would be weld properties that are 85% of the base metal properties [2], because the base metal is at the harder and stronger H24 temper where as the weld metal properties would be at the softer and lower strength F or O temper. In all trials, the lower travel speed and lower power level welds were generally found to be beneficial for maximizing the mechanical properties. Figure 4-54 shows all the recorded tensile results for the diode, CO_2, and fibre laser trials in terms of actual values and as a percentage of the base metal properties. The strongest diode laser weld achieved 184 MPa stress at failure, while the CO_2 laser beam welds were able to achieve 222 MPa. Both of these optimized laser welds still only managed elongation between 1.1 and 1.6 mm displacement compared to the base material extension of 9.9 mm. The scatter of the tensile property results of these welds were also very large, the diode laser welds having more than 10% average value deviation and the CO_2 laser welds increasing that to over 15%. The fibre laser welds achieved a vast improvement over the other trials producing weld samples which resisted in excess of

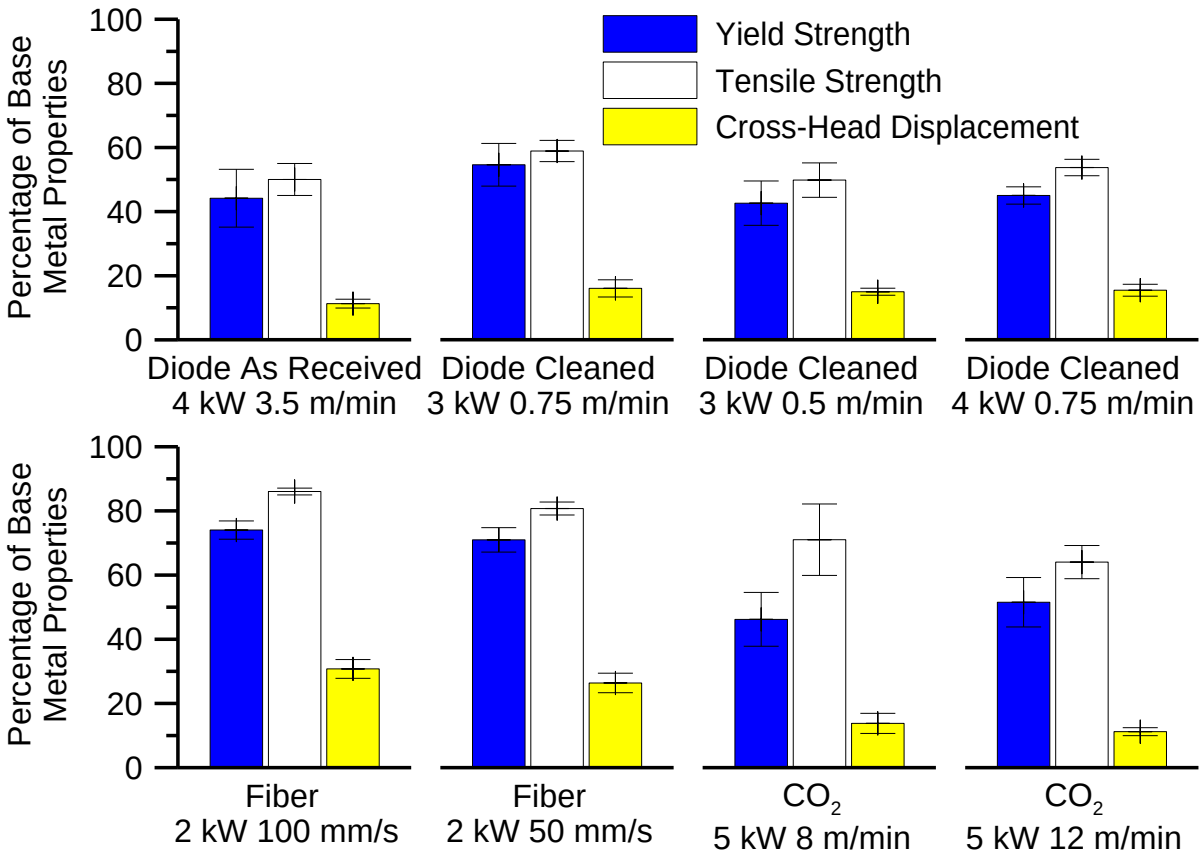

Figure 4-54: Laser welded transverse tensile properties of the diode, CO_2, and fibre laser welded specimens as a percentage of the base metal properties.

270 MPa, 86% of base metal strength, and more consistent values with overall property deviations below 5%. The fibre laser trials still only produced elongations around 3 mm, but even this was close to double any of the values measured from welds made using the previous laser welding systems. The fibre welded tensile samples showed a pronounced transition between the elastic and plastic deformation regions whereas the welds made using the diode and CO_2 lasers exhibited little or no plastic deformation prior to failure.

The ultimate stress and displacement to failure of the welded samples were the best indicators of weld quality. Any weld defects acted as strain localizers and this severely limited the ability of the material to undergo significant plastic deformation prior to fracture

and frequently changed the fracture mode from ductile to brittle. Several factors contributed to enable the fibre lasers' higher weld quality; the samples were all fully cleaned and stainless steel wire brushed to remove surface oxides and contaminants, the sample interfaces were machined to ensure excellent joint fit-up, the magnesium experienced higher absorptivity for the fibre laser beam, and the process was optimized for both weld travel speed and laser beam intensity. The low travel speed and laser beam power reduced the vaporization experienced by the weld pool and increased the solidification time which allowed the weld pool greater time to settle and form a smoother, more continuous weld bead surface while operating fast enough to be viable for mass production.

Chapter 5
Conclusions and Recommendations

5.1 Diode Laser Welding

The diode laser welding system operated in conduction mode for all welds due to the unique elongated laser beam shape and low power density at the laser beam focus. This created weld profiles that were much wider than the sheet thickness. Experimental Series A with bead-on-plate welds demonstrated the effectiveness of the undisturbed original oxide layer in preventing oxidation and vaporization of the molten weld metal, even when no additional shielding was used. However, the oxide layer was broken by mixing or boiling of the underlying material, it was incorporated into the weld fusion zone where it produced incipient cracks in the weld metal that severely reduced the strength and ductility of the weld.

In Experimental Series B, the weld specimens were sheared and seam welds were made in the butt-joint configuration. The entrapment of gas and the oxides along the joint interface caused difficulties with coupling between the laser beam and metal and resulted in the formation of melt pull-back and gaps along the fusion zone. If the gaps closed and coupling was again achieved, the interface would be contaminated with long oxide films pulled from the top and bottom surfaces inciting significant solidification cracking.

When the oxide was cleaned off the surface by stainless steel wire brushing in Experimental Series C and D the sheet magnesium alloy displayed lower effective absorptivity, where the average travel speed for successful welding had to be decreased by up to 90% to produce comparable weld bead profiles with those produced in Experimental Series A and B with no oxide removal. Weld specimens prepared by shearing were found to have excessive gaps and frequently exhibited melt pull-back or centre-line cracking. These defects were reduced or eliminated by machining the faying surfaces prior to welding.

All of the diode laser weld transverse tensile properties of these low quality welds were poor. The ultimate failure strength was less than 50 to 60% of the base metal strength. The final optimized diode laser weld sample was produced in Experimental Series D at a laser power of 3 kW and travel speed of 0.75 m/min. It was found that the original oxide must be removed before welding to prevent its incorporation into the weld, that the faying surface must be machined to reduce the gap below 5% of the material thickness, and that a very low travel speed was required to overcome the reduced absorptivity of the cleaned magnesium sheet.

5.2 CO_2 Laser Welding

The weldability trials conducted with the CO_2 laser were used to investigate the effects of travel speed on the mechanical properties of welds made using a high power density laser welding process. When welding with high power density lasers, the keyhole-mode weld pools were produced that were much deeper than they were wide. The surfaces of the CO_2 laser welds showed evidence of boiling and expulsion from the keyhole. The high vaporization rates reduced the effective cross section and combined with the high rate of solidification, introduced undercutting and incipient cracks into the fusion zone. Compared to the diode laser welds, the CO_2 welds experienced much greater mixing in the weld pool. This was evidenced by the increased frequency of entrapped hydrogen gas porosity. With the presence of the surface cracks and gas pores, the CO_2 transverse tensile samples achieved ultimate tensile strengths that were less than 70% of the base metal properties. The optimized 5 kW weld was the widest fusion zone conducted at 8 m/min. Welding with the CO_2 laser produced welds that were stronger than those created with the diode laser but they still suffered from very poor weld bead quality, excessive weld defects, and little or no weld metal ductility.

5.3 Fibre Laser Welding

All specimens for the fibre laser welding experiments were machined to minimize the joint gap, degreased, and stainless steel wire brushed to remove all pre-existing hydrated oxides prior to welding. When welding at the high power levels, the fibre laser welds showed evidence of boiling and expulsion similar to the CO_2 results. Lower welding power and slower welding speeds provided smoother weld bead surfaces, and provided the highest

weld quality with little or no evidence of solidification cracking, macro-porosity, or bulk material loss. The fibre laser welds conducted at 2 kW and 100 mm/s provided the highest ultimate tensile strength results of any tested laser weld, achieving over 86% of the base material's failure load. In addition, there was a significant improvement in weld metal ductility. The fibre laser welds performed the best in tensile testing and suffered premature failure mainly because of the normally expected softening experienced in the weld's heat affected and fusion zones.

5.4 Laser Weldability of AZ31B-H24 Using Laser Beam Welding Processes

Three different continuous lasers welding processes were investigated in this research; the diode laser was a low power density laser, while the CO_2 and the fibre lasers were high power density lasers. The diode laser produced large conduction-mode weld pools, with fusion zones that were between 5 and 12 mm in width and heat affected zones that reached the clamp and a width of 20 mm. The increased size of the weld resulted in the weld pool experiencing high amounts of sagging that acted as a strain localizer in the fusion zone during loading. Due to the weld geometry and poor tensile results, the diode welds were deemed unacceptable.

With the high power density CO_2 and fibre lasers, keyhole-mode welds were produced with approximately 1 mm wide welds and parallel fusion boundaries. The CO_2 laser was tested at 5 kW and produced welds that were inundated with too much energy, which caused excessive vaporization and poor weld bead quality. The fibre laser produced results similar to the CO_2 laser at powers above 2 kW. However at 2 kW power, the fibre laser produced much higher quality weld samples. The weld surfaces were consistent and without incipient

surface cracks to promote premature crack initiation. These welds produced the highest mechanical properties of any tested weld samples. The optimized fibre laser trials produced tensile samples that achieved over 85% of the ultimate strength of the base material and exhibited a clear transition to plastic deformation. These welds were inherently weaker than the base material because the welded material was reverted to a fully annealed state in the fusion zone, i.e., an “F” or “O” temper designation, whereas the base metal was hot worked and half annealed to make it both stronger and harder.

The highest quality laser welds were produced only when the joint was machined to minimize the gaps between the weld specimens and when the specimens were degreased and the surface oxide removed mechanically by stainless steel wire brushing. These steps were required to minimize the occurrence of weld defects in the welds such as oxide inclusions or hydrogen porosity that would act as strain localizers and severely lower weld metal ductility and strength. Form the conducted trials with the diode, CO_2, and fibre laser beam welding systems, the highest strength and ductility were produced when operating in keyhole-mode. The process was further refined by decreasing the travel speed to increase the solidification time and reducing the power to limit boiling in the fusion zone during the fibre laser beam welding trials. Of the three laser welding processes examined in this study, the fibre laser produced the highest quality, strongest, and most ductile welds when analyzed in transverse tensile testing. However, direct comparisons between the CO_2 and fibre laser welds could not be made because they were made using different joint preparations and welding conditions.

References

[1] ASTM Standard B557, 2002 (2006), "Standard test methods for tension testing wrought and cast aluminum- and magnesium-alloy products", ASTM International, West Conshohocken, PA, 2006, DOI: 10.1520/B557-02R06, www.astm.org.

[2] *ASM Metals Handbook* (10th ed., Vol. 2: Properties and Selection: Nonferrous Alloys and Special Purpose Materials). (1990). Materials Park, OH: ASM International.

[3] Smith, W. F. (1993). *Structures amd Properties of Engineering Alloys* (2nd ed.). New York, NY: McGraw Hill Inc.

[4] Ghali, E., Dietzel, W., & Kainer, K.-U. (2004). General and localized corrosion of magnesium alloys: a critical review. *Journal of Materials Engineering and Performance, 13* (1), 7-23.

[5] Quan, Y., Chen, Z., Gong, X., & Yu, Z. (2008). CO2 laser beam welding of dissimilar magnesium-based alloys. *Material Science and Engineering A* (496), 45-51.

[6] Sun, Z., Pan, D., & Wei, J. (2002). Comparative evaluation of tungsten inert gas and laser welding of AZ31 magnesium alloy. *Science and Technology of Welding and Joining , 7* (6), 343-351.

[7] Leong, K. H., Kornecki, G., Sanders, P. G., & Keske, J. S. (1998, 16-19 November). Laser Beam Welding of AZ31B-H24 Magnesium Alloy. Proc. *ICALEO: Laser Materials Processing Conferance*, Orlando, FL. 28-36.

[8] Cao, X., Jahazi, M., Immarigeon, J. P., & Wallace, W. (2006). A review of laser welding technologies for magnesium alloys. *Journal of Material Processing Technology* , 171, 188-204.

[9] Ready, John F.; Farson, Dave F. (Eds.) (2001). *LIA Handbook of Laser Materials Processing.* Orlando, FL: Laser Institute of America Magnolia Publishing, Inc.

[10] Kou, S. (2003). *Welding Metallurgy.* Hoboken, NJ: John Wiley & Sons, Inc.

[11] Diehl, R. (Ed.). (2000). *High-Power Diode Laser Fundamentals, Technology, Applications.* New York, NY: Springer.

[12] Howard, K. L. (2005). *Diode Laser Welding of Aluminum Sheet.* MASc Thesis: University of Waterloo, Waterloo, ON Canada.

[13] Silfvast, W. T. (2004). *Laser Fundamentals* (Second ed.). New York, NY: Cambridge University Press.

[14] Hilton, P. (2001). *Carbon dioxide laser.* Retrieved July 2009, from http://materialteknologi.hig.no/Lettvektdesign/joining methods/joining-welding-laser welding Al.htm

[15] Gahan, B. C., & Shiner, B. (2004, Winter). New high-power fibre laser enables cutting-edge research. *Laser Technology* , 29-31.

[16] Quintino, L., Costa, A., Miranda, R., Yapp, D., Kumar, V., & Kong, C. J. (2007). Welding with high power fibre lasers - A preliminary study. *Materials and Design* (28), 1231-1237.

[17] Duley, W. W. (1999). *Laser Welding.* Toronto: John Wiley and Sons.

[18] Al-Kazzaz, H., Medraj, M., Cao, X., & Jahazi, M. (2008). Nd:YAG laser welding of aerospace grade ZE41A magnesium alloy: Modeling and experimental investigations. *Materials Chemistry and Physics* (109), 61-76.

[19] Goncalves, C. V., Vilarinho, L. O., Scotti, A., & Guimaraes, G. (2006). Estimation of heat source and thermal efficiency in GTAW process by using inverse techniques. *Journal of Materials Processing Technology , 172*, 42-51.

[20] *ASM Metals Handbook* (10th ed., Vol. 6 Welding, Brazing, and Soldering). (1990). USA: ASM International.

[21] Zhou, W., Long, T. Z., & Mark, C. K. (2007). Hot cracking in tungsten inert gas welding of magnesium alloy AZ91D. *Materials Science and Technology , 23* (11), 1294-1299.

[22] Zhang, Z., Liu, L., & Sun, H. (2008). AC TIG welding with single-component oxide activating flux for AZ31B magnesium alloys. *Journal of Material Science , 43*, 1382-1388.

[23] Sun, D. Q., Lang, B., Sun, D. X., & Li, J. B. (2007). Microstructure and mechanical properties of resistance spot welded magnesium alloy joints. *Materials Science and Engineering A* (460-461), 494-498.

[24] Gould, J. E., & Chuko, W. (2006, March). Investigating resistance and friction stir welding processes for joining magnesium. *Welding Journal* , 46-53.

[25] Thomas W. M., Nicholas, E. D., Needham, J. C., Church, M. G., Temple-smith, P., Dawes, C. J., GB Patent Application No. 9125978.9 (December 1991).

[26] Afrin, N., Chen, D. L., Cao, X., & Jahazi, M. (2008, January). Microstructure and tensile properties of friction stir welded AZ31B magnesium alloy. *Materials Science and Engineering A*, 472 (1-2), 179-186.

[27] Xunhong, W., & Kuaishe, W. (2006). Microstructure and properties of friction stir butt-welded AZ31 magnesium alloy. *Materials Science and Engineering A* (431), 114-117.

[28] Chi, C.-T., Chao, C.-G., Liu, T.-F., & Wang, C.-C. (2008, March). Optimal parameters for low and high voltage electron beam welding of AZ series magnesium alloys and mechanism of weld shape and pore formation. *Institute of Materials, Minerals and Mining*, 13 (2), 199-211.

[29] Chi, C.-T., Chao, C.-G., Liu, T.-F., & Wang, C.-C. (2006). A study of weldability and fracture modes in electron beam weldments of AZ series magnesium alloys. *Materials Science and Engineering A* (435-436), 672-680.

[30] Chi, C.-T., & Chao, C.-G. (2007). Characterization of electron beam welds and parameters for AZ31B-F extrusive plates. *Journal of Materials Processing Technology*, (182), 369-373.

[31] Liu, L., Song, G., Liang, G., & Wang, J. (2005). Pore formation during hybrid laser-tungsten inert gas arc welding of magnesium AZ31B--mechanism and remedy. *Materials Science & Engineering A , 390*, 76-80.

[32] Song, G., Liu, L., & Wang, P. (2006). Overlap welding of magnesium AZ31B sheet using laser-arc hybrid process. *Materials Science and Engineering A* (429), 312-319.

[33] Liu, L. M., Song, G., & Zhu, M. L. (2008). Low-power laser/arc hybrid behavior in AZ-based Mg alloys. *Metallurgical and Materials Transactions A, 39A*, 1702-1711.

[34] Zhu, J., Li, L., & Liu, Z. (2005). CO_2 and diode laser welding of AZ31 magnesium alloy. *Applied Surface Science* (247), 300-306.

[35] Pan, L. K., Wang, C. C., Shih, Y. C., & Sher, H. F. (2005). Optimising multiple qualities of Nd:YAG laser welding onto magnesium alloy via grey relational analysis. *Science and Technology of Welding & Joining*, 10 (4), 503-510.

[36] Quan, Y. J., Chen, Z. H., Gong, X. S., & Yu, Z. H. (2008). Effects of heat input on microstructure and tensile properties of laser welded magnesium alloy AZ31. *Materials Characterization* (59), 1491-1497.

[37] Cao, X., Xiao, M., Jahazi, M., & Immarigeon, J.-P. (2005). Continuous Wave Nd:YAG Laser Welding of Sand-Cast ZE41A-T5 Magnesium Alloys. *Materials and Manufacturing Processes* (20), 987-1004.

[38] Yu, L., Nakata, K., Yamamoto, N., & Liao, J. (2009). Texture and its effect on mechanical properties in fiber laser weld of a fine-grained Mg alloy. *Material Letters, 63*, 870-872.

[39] *ASM Metals Handbook* (10th ed., Vol. 3: Alloy Phase Diagrams). (1990). Materials Park, OH: ASM International.

[40] Zhao, H., & DebRoy, T. (2001, August). Pore Formation during laser beam welding die-cast magnesium alloy AM60B -- mechanism and remedy. *Welding Journal*, 80 (8), 204-s-209-s.

[41] Arner, J., personal communications. Struers. (2009, April). Grinding and Polishing Sample Preparation for AZ31B.

[42] Wielage, B., & Mucklich, S. (2006, September). Improving the soldering of magnesium alloys. *Brazing & Soldering Today*, 48-51.

[43] Asahina, T. (2005). Pulsed YAG laser weldability of magnesium alloy. *Welding International, 19* (1), 23-28.

[44] *G2 PFA Manual.* (2004). USA: Panasonic Factory Automation.

[45] Howard, K., Lawson, S., & Zhou, Y. (2006, May). Welding aluminum sheet using a high power diode laser. *Welding Journal*, 85 (5), 101s-110s.

[46] *KUKA Robotics Corp.* (n.d.). Retrieved June 2009, from KUKA Industrial Robots: http://www.kuka-robotics.com/usa/en/products/industrial_robots/medium/kr60_ha.htm

[47] Deutsch, M. G., Punkari, A., Weckman, D. C., & Kerr, H. W. (2003). Weldability of 1.6 mm thick AA5182 aluminum sheet by single- and dual-beam Nd;YAG laser welding. *Science and Technology of Welding and Joining , 8* (4), 246-256.

[48] Kwon, Y., & Weckman, D. C. (2008). Double sided arc welding of AA5182 aluminum alloy sheet. *Sci. Technol. Welding Joining*, 13(6), 485-495 .

[49] Grong, O. (1997). *Metallurgical Modelling of Welding* (2nd ed.). London, UK: The Institute of Materials.

[50] Liu, L.-M., Wang, H.-Y., & Zhang, Z.-D. (2007). The analysis of laser weld bonding of Al alloy to Mg alloy. *Scripta Materialia*, (56), 473-476.

[51] Liu, L., Wang, H., Song, G., & Ye, J. (2007). Microstructural characteristics and mechanical properties of laser weld bonding of magnesium to aluminum alloy. *Journal of Material Science*, (42), 565-572.

[52] Borrisutthekul, R., Miyashita, Y., & Mutoh, Y. (2005). Dissimilar material laser welding between magnesium alloy AZ31B and aluminum alloy A5052-O. *Science and Technology of Advanced Materials* (6), 199-204.

[53] Horstemeyer, M. F., & Ramaswamy, S. (2000). On factors affecting localization and void growth in ductile metals: A parametric study. *International Journal of Damage Mechanics, 9* (5), 5-28.

Appendix A

Diode Laser Operating Procedure

For producing welded samples from the diode laser equipment at the University of Waterloo, Canada, the following steps were followed by a trained operator.

1. The power is turned on to the robotic arm controller and laser power supply. Keys are required to operate the robotic arm's pendant as well as the laser power supply.

2. The water chiller is turned on to cool the distilled water supply to 19° C. If this is the first weld it requires a minimum of 5 minutes before any welds are conducted. Subsequent welds do not normally require any wait time. When there is insufficient distilled water or the water temperature is too high, warnings will appear and prevent operation of the laser.

3. The helium and compressed air cylinders are opened.

4. The air flow is set to 2.5 l/min (5 SCFH) to remove any moisture in the diode laser head and both helium flows are set to 2.5 l/min (5 SCFH) to purge the lines and shielding device of contamination. Similar to the chiller mentioned in step 2, for the first weld this must be allowed to flow for at least 5 minutes before welding and is assumed stabilized for subsequent welds that have not had the system turned off. Warnings will also prevent laser operations if the relative humidity or dew points in the laser is too high.

5. The cleaned samples are clamped in the jig.

a. A locator spacer is placed on the far lip and the first half sample is butted against it.

b. The half sample is secured with 2-6 bolts as space permits. Spacers are used as needed to keep the clamp flat on the sample.

c. The locator spacer is removed and the other half sample is butted against the connecting half.

d. The second half sample is similarly secured mirroring the first.

6. The laser welding program is opened. This shows simple coding that provides control of the robotic arm and allows inputting of operation parameters.

7. The laser sights are activated. Through the use of the pendent the key points are programmed into the laser controller.

8. The power and travel speed is selected. The laser software allows travel to be incremented in 0.01 m/min and power to be altered in 0.01 kW steps. The program is saved with the form "Prog00XX.prg" where XX is replaced with the desired program identification number. The pedestal is then set to run the desired program corresponding to the last two numbers of the program.

9. The pendent robotic arm controller is switched to 'automatic mode' where the robots actions are now controlled by the computer.

10. Laser specific safety eye wear is put on and then the system is set to operate mode.

11. The laser sights are turned off and the warning lights are checked for activation. If laser operation lights have not activated the controller is returned to standby.

12. The air flow is increased to 5 l/min (12 SCFH). The helium is increases to 12 l/min (25 SCFH) for back shielding and 35 l/min (75 SCFH) for top shielding.

13. Both pedestal safety switches are activated to enable the robotic arm's motion and confirm automated control in that order.

14. All safety interlocks are checked for compliance. The laser cannot be activated if any of the safety sensors have been faulted.

15. The laser is armed and all four diode banks are checked for operation.

16. With all individuals outside of the lasers minimum safe radius and possible range of motion for the robotic arm, the operator stands at the pedestal covering the emergency stop and activates the start button. Welding is observed from a safe distance and the emergency stop is triggered if any aberrations occur in programming or weld dynamics. If the emergency stop is activated, the entire control system must be shut down and cycled before the arm can be used again.

17. Once the weld is complete the diode arrays are disarmed. And the power supply is returned to standby mode. Laser operation lights should turn off and laser safety glasses can be removed.

18. The pendant is switched back to 'teach' mode deactivating the robotic arm.

19. The gas flows are returned to 2.5 l/min (5 SCFH) if additional welds are planned or turned off and the cylinders closed.

20. The sample is removed from the clamps and welding parameters are recorded.

21. If welding is complete the power supply is returned to the ‘off’ setting and the robotic arm control power supply is turned off. Both keys are removed from the system to prevent tampering or inadvertent operation. Otherwise the process is repeated from step 4.